

**TIME-LAPSE SEISMIC MODELING FOR CO_2 SEQUESTRATION
AT THE DICKMAN FIELD, KANSAS**

A Dissertation

Presented to

the Faculty of the Department of Earth and Atmospheric Sciences

University of Houston

In Partial Fulfillment

of the Requirements for the Degree

Doctor of Philosophy

By

Jintan Li

December 2012

**TIME-LAPSE SEISMIC MODELING FOR CO_2 SEQUESTRATION
AT THE DICKMAN FIELD, KANSAS**

Jintan Li

APPROVED:

Dr. Robert R. Stewart, Chairman

Dr. Christopher C. Liner

University of Arkansas 72701

Dr. Michael A. Murphy

Dr. Aibing Li

Dr. Mark A. Smith, Dean, College of Natural
Sciences and Mathematics

ACKNOWLEDGMENTS

I want to express my sincere gratitude to my former academic advisor, Dr. Christopher Liner, for his support, guidance, enthusiasm, patience, and encouragement during this study. Thanks to his excellent direction, I could explore new fields of knowledge and complete my Ph.D. study.

I would also like to express my gratitude to my current advisor Dr. Robert Stewart for his generous support, Dr. Michael Murphy, Dr. Aibing Li, Dr. Tien-when Lo, and Dr. Rodney Johnston for their valuable comments and suggestions to improve the quality of my research and dissertation as my committee.

I also want to thank Dr. Po Geng and Dr. Jianjun Zeng for their input and many useful discussions during my research study.

I also want to thank my group members of CO_2 Capture and Storage project at University of Houston. I would also like to thank Dr. De-hua Han and Min Sun for their invaluable input for my research work.

I want to give my special thanks to my family for their support during my work.

**TIME-LAPSE SEISMIC MODELING FOR CO_2 SEQUESTRATION
AT THE DICKMAN FIELD, KANSAS**

An Abstract of a Dissertation

Presented to

the Faculty of the Department of Earth Sciences

University of Houston

In Partial Fulfillment

of the Requirements for the Degree

Doctor of Philosophy

By

Jintan Li

December 2012

ABSTRACT

Time-lapse seismic modeling is often used to study hydrocarbon reservoirs, especially for those undergoing injection or production. The Dickman field, Kansas, provides two possible CO_2 sequestration targets: a regional deep saline reservoir (the primary objective) and a shallower mature, depleted oil reservoir (secondary). The work in this dissertation characterizes and simulates monitoring of CO_2 movement before, during, and after injection including fluid flow paths, reservoir property changes, CO_2 containment, and post-injection stability. My seismic simulation for time-lapse CO_2 monitoring was based on flow simulator output over a 50-year injection and 250-year simulation period. This work introduces a feasible and reliable regridding technique that resolves different scales from geological modeling, flow simulation, to seismic modeling for a realistic carbonate geological model. Gassmann fluid substitution theory is applied to calculate fluid properties changes before and after injection. For a porous Mississippian carbonate reservoir with average 25% porosity, the P wave velocity can change around 15% with CO_2 saturation up to 84%. Seismic simulation was accomplished via PP and PS reflectivity from the Zoeppritz equation, convolutional (1D), acoustic and elastic (2D) finite difference modeling by a flux-corrected transport equation. This work assesses the effectiveness of 4D seismic monitoring in the evaluation of long-term CO_2 containment stability through a fault leakage test. A CO_2 plume can be detected from the difference on seismic sections with 5 to 10ms time shift at the storage site before and after injection, and was validated by comparison with the prestack field data. Time-lapse flow to seismic modeling is proved to be useful for carbon dioxide sequestration in a hard rock carbonate reservoir.

CONTENTS

1. INTRODUCTION AND BACKGROUND	1
1.1 CO_2 sequestration and storage (CCS)	1
1.2 Flow simulation to time-lapse seismic	4
1.3 Objectives	7
2. THE DICKMAN FIELD	10
2.1 Geological setting	10
2.2 Flow simulation	16
3. GASSMANN FLUID SUBSTITUTION	24
3.1 Nature of flow simulation grids	24
3.2 Flow parameters in each cell	25
4. FLOW SIMULATION REGRIDDING	27
5. SEISMIC SIMULATION METHODS	37
5.1 PP and PS reflectivity	37
5.2 Seismic simulation methods	38
5.2.1 One-dimensional convolutional forward modeling	38
5.2.2 Two-dimensional convolutional acoustic and elastic forward modeling	40

6. RESULTS and DISCUSSIONS	43
6.1 PP and PS reflectivity	43
6.2 Forward modeling results	49
6.3 Reservoir properties	50
6.4 Example 1: One dimensional convolutional forward modeling results	55
6.4.1 Validation of gridding technique	67
6.5 Example 2: Two dimensional acoustic and elastic forward modeling results	68
6.5.1 Acoustic forward modeling results	69
6.5.2 Elastic forward modeling results	75
6.6 Discussion	88
6.6.1 Comparison of 1D convolutional and 2D acoustic forward modeling	88
6.6.2 Signal-to-noise ratio study	90
6.6.3 Comparison with the real seismic data	93
6.6.4 Multiple shot gathers	95
6.6.5 Horizontal injection design	97
6.7 Other attempts: Prestack inversion result from UT	98
7. SUMMARY	105
<i>References</i>	107

<i>Appendices</i>	115
A. Detailed Gassmann fluid substitution work flow for the Dickman field	116
1 Kmin and density	116
2 Kfluid	117
3 Kdry	117
4 Ksat	118
B. Preprocess the flow simulation output	119
1 Skipping headers	119
2 Adding missing points	121
C. Flux correction to the transport equation for elastic forward modeling finite difference method	123
1 Implementation of elastic finite difference forward modeling	123
2 Implementation for generating the stiffness and shear model	127

1. INTRODUCTION AND BACKGROUND

1.1 CO_2 sequestration and storage (CCS)

As atmospheric CO_2 levels become an increasing concern, the initiative to reduce them by carbon dioxide capture and storage has raised considerable interest. This is partially based on the experiences with enhanced oil recovery using CO_2 injection. The International Energy Administration (IEA) estimated that the annual greenhouse gas (carbon or carbon equivalent) emission to be around 1.5 giga-tons (Gt) by 2011 (Reimer, 1994). The most recent definition for carbon sequestration and storage (CCS) by U.S. Geological Survey is used to "describe both natural and deliberate processes by which CO_2 is either removed from the atmosphere or diverted from emission sources and stored in the ocean, terrestrial environments (vegetation, soils, and sediment), and geologic formations". The geologic, hydrologic, and ecological consequences have been investigated to estimate storage source potential for CO_2 injection and retainment for thousands of years. A number of organizations including U.S. Department of Energy, National Energy Technology Laboratory, etc. have established collaboration with U.S. Geological Survey to develop the geological models to be accessed for CCS (http://www.usgs.gov/climate_landuse/carbon_seq). This dissertation presents one of those CCS projects under the Department of Energy (DOE award: DE-FG26-06NT42734).

CO_2 capture and storage (CCS) was first discussed in late 1970s (Baes and Lee, 1980). The candidates for CCS include deep saline aquifers, depleted hydrocarbon reservoirs, and coal beds used as storage sites for long-term carbon sequestration. Worldwide deep saline reservoir CO_2 storage capacity is estimated to range from 1,000 to 100,000 giga-tons, and considered saline aquifers as ideal storage candidate (Metz *et al.*, 2005). The trapping

mechanisms for CCS include mineral trapping, residual gas trapping, solubility trapping, geological trapping, and hydrodynamic trapping (Liner *et al.*, 2011).

Mineral trapping is the safest and considered as "permanent" trapping mechanism. In deep saline aquifers, solubility trapping (CO_2 dissolved in the water) can also be a very safe trapping mechanism, because CO_2 dissolved in water will react with the minerals and slowly precipitate new products. **Residual gas trapping** means that CO_2 can be trapped as immobile fluid in the porous space. This occurs on the pore scale but the amount of stored CO_2 can be significantly varied depending on the rock formation (Metz *et al.*, 2005), and can also be as permanent as mineral trapping. For **geological trapping**, CO_2 is held in structural or stratigraphic traps that has extremely low permeability or any fracture or fold that is impermeable (a seal or cap rock). **Hydrodynamic trapping** means that the CO_2 behaves like a free-phase liquid and trapped in the fluid flow. Due to buoyancy of CO_2 which has a smaller density than underground water or brine, CO_2 will move slowly on the top of brine in the deep saline aquifer unless there is any change in pressure or temperature. This trapping mechanism also has a potentially large storage capacity (Bachu, 2003; Metz *et al.*, 2005). Other factors that may impact CO_2 trapping efficiency can be CO_2 injection rate, duration, injector location and if there is any leakage through corroded well pipes (Liner *et al.*, 2011). It is worth mentioning that the risk of trapping free phase CO_2 is significantly high as it is mobile and the storage would not be stable if an up-section leak is present. Under conventional CO_2 injection procedures, over 50% of CO_2 will be in a free-phase state trapped either by geological or hydrodynamic trapping (Liner *et al.*, 2011). Time scales for different trapping mechanisms are shown in Figure 1.1. CO_2 capture and storage also faces both political and environmental challenges. The Underground Injection Control (UIC) program of the Environmental Protection Agency (EPA) addresses the pathways where CO_2 might migrate into underground sources of drinking water. Furthermore,

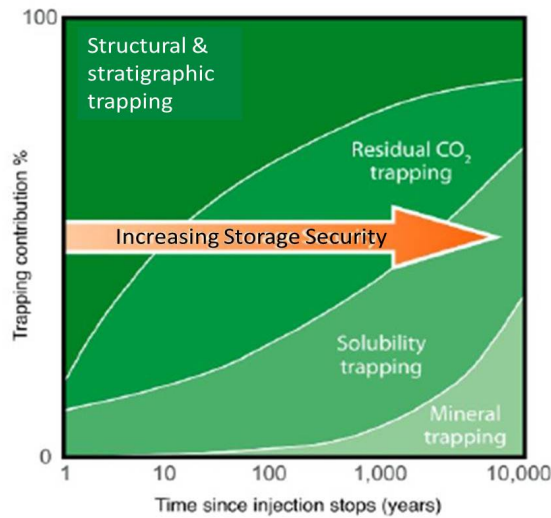


Figure 1.1. Time scales for different trapping mechanisms. After Metz *et al.* (2005).

several important factors need to be carefully considered: siting, area of review, well construction, operation, mechanical integrity, monitoring well plugging, and post-injection site care. These regulations are evaluated with risk analysis to guarantee safe and long-term carbon dioxide capture and storage (Raza, 2009).

There have been several key CCS projects throughout the world. CO_2 plume monitoring was first introduced at the Sleipner field in the Norwegian North Sea (Chadwick *et al.*, 2010), which was a field test of CO_2 injection into a saline reservoir of late Cenozoic age. The In Salah project in Algeria is a large-scale CO_2 injection project that has been in operation since 2004 (Mathieson *et al.*, 2010). The Weyburn Field in Canada has injected CO_2 into depleted gas reservoirs since 2000 (Ma and Morozov, 2010), showing that time-lapse P-impedance data is able to provide valuable interwell information to aid the flow simulation history matching (Yamamoto *et al.*, 2004). In South Eastern Australia, a large scale test with 100,000 tons of CO_2 injection was performed, 80% of which was produced from a depleted gas reservoir. This project was tested for CO_2 safe storage, transportation,

and behaviorial status at different time intervals. The whole process includes pre-injection, production, post injection and closure as well as longer term injection plan (Dodds and Sharma, 2009).

1.2 *Flow simulation to time-lapse seismic*

This dissertation presents a systematic study from the field site geological setting, to flow simulation, to seismic modeling. The essential part of this process is to accurately interpret the reservoir properties from flow simulation model and apply them to perform seismic modeling which follows a general routine as flow to seismic. This will include a regridding process that resolves the different scales from flow simulation grid to a seismic grid.

Flow simulation is used to simulate liquid and gas flow in real world conditions, and the models are usually calibrated by history matching of pressure, fluid contacts, and oil and water production data. This process includes analysis from petrophysical static modeling which relates porosity, shale volume and permeability which will further be developed into a dynamic model including saturation, temperature, and pressure changes at different time intervals.

A good reference for this general analysis procedure is provided by Samson *et al.* (1998). A general process starts from building a 3D structural model including mapping faults, horizons, etc., followed by a 3D sedimentary model including depositional environment and facies modeling, as well as a final 3D petrophysical model (from static to dynamic fluid properties). This work flow is generally applied in flow simulation for most exploration and production practices. For example, flow simulation and petrophysical analysis are used to aid history matching to better define fluid movement between wells (Fanchi, 2001). Using repeated seismic surveys, the simulated seismic response can be compared with the real

seismic response, and thus a consistent flow simulation model can be determined (Brinks and Fanchi, 2001). However, different scale issues among geological model, seismic earth models and flow simulation models should be carefully addressed.

Grid cell size is an important attribute in flow simulation. Due to the high computational cost of flow simulation runs, there is a compromise between the choice of cell size and computation time. To this end, the grid cell size for flow simulation may be considerably larger than geological modeling (normally less than a half meter) and seismic scale (less than 10m).

Previously, many researchers have discussed the flow simulation regridding to optimize computational time. For example, the Society of Petroleum Engineers (SPE) Comparative Solution Project flow simulation model was downscaled to seismic grid size, and converted into V_p , V_s , and density for seismic simulation by using both fine and coarse grid sizes to obtain finite difference modeling results. It was shown that for seismic response below 80Hz, the coarse grid is acceptable, and the difference at higher frequency is smaller (Stoffa *et al.*, 2005). For a locally complex reservoir, saturation patches from the flow simulator will influence the seismic response because of fine scale variations. Upscaling the grid cell size is not feasible in flow simulation due to its expensive computation and efficiency, so this is done by downsizing fluid saturation within a coarse grid cell consistently within the flow simulator to simulate the local fine scale flow change and match the boundary conditions for both coarse and fine grids (Castro and Caers, 2005).

The other work related is upscaling from log scale (fine) to flow simulation scale (coarse) by using Backus averaging, and then obtaining the blocking velocities and densities. The deviation of P and S waves can lead to 20% or more depending on the size of the window chosen and other factors (such as heterogeneity within the grid cell) (Menezes and Gosselin, 2006). The velocities and densities can be calculated within each flow simulation cell, but

the calculation is based on the evenly spacing grid in all (x,y,z) direction. Meanwhile, in the work from Emerick *et al.* (2007), the structure of the reservoir was not mentioned clearly. Moreover, the output was still the P and S wave velocity and density, and the regridding process was not fully described either.

Another study with a localized variations of structure was only done in the flow simulation model (Enchery *et al.*, 2007). They performed a complex work flow only for downscaling the saturation and pressures in the grid including: 1) first identify the downscaling region where permeability is greater than the user-defined threshold, and 2) then run the flow simulation in the downscaled area and keep the saturation and pressures in the coarse grid blocks. The computation time is constrained by the threshold value and this process may be time-consuming. Another study used a downscaled seismic grid to flow simulation grid conducted by integrating stochastic seismic inversion models and Gaussian geostatistical model for fine-scale layer thickness and other reservoir properties. It can preserve correlations implied by rock physics and seismic data, but this work flow was quite complex (Kalla *et al.*, 2009). Another study for resolving rescaling issues from reservoir to seismic used an arithmetic average upscaling for the physical properties (pressures and saturations) from a fine grid to a coarse grid within seismic resolution scale. But this upscaling procedure can hamper the history match in local regions due to the lost information in the scaling process (Avansi *et al.*, 2010).

A similar study involving flow simulator to seismic simulation was conducted in the Forties field, North Sea by incorporating stratigraphy and structure with fluid properties into the flow simulator to build a regular seismic property grid (V_p , V_s , and density) (Ribeiro *et al.*, 2007). A 4D seismic modeling work conducted in the Statfjord Field, Norway also used a similar approach (Al-Najjar *et al.*, 1999; Doyen *et al.*, 2000) as well as other studies (Skorstad and Kolbjornsen, 2005; House *et al.*, 2003). However, all these studies did not

introduce a complex geological model into flow simulation, which differs from our approach. For time-lapse monitoring, flow simulation to seismic are always related to each other. Time-lapse monitoring relies on the fundamental physical basis: velocity and density. For the repeated surveys, the economic impact for acquisition can be very significant. However, for subtle reservoir changes or noisy seismic data, it is very necessary to maximize repeatability by obtaining multiple acquisition surveys (Johnson, 1997; Key and Smith, 1998).

The effectiveness for 4D seismic depends on how much change can be detected on the seismic data due to the dynamic reservoir property changes at various times. Seismic reflection coefficients represent impedance contrasts between the two intervals. If a contrast is evident, a large reflection coefficient will have seismic response that can be easily detected on the two different surveys. This is also bounded by the thin layer reservoir when seismic resolution is not sufficient to resolve the inter-bedded reflections and thus cause noise etc. Seismic bandwidth and changes of the dynamic fluid properties are both key factors (Pagano *et al.*, 2000). Time-lapse monitoring can also be used for monitoring streamline fluid flow (Yuh *et al.*, 2000). In most cases this "flow simulation to seismic" is used to compare the simulated seismic response and to observe seismic response to help adjust the flow simulation model. The seismic simulation can be full wave or AVO analysis (Davies and Maver, 2004).

1.3 Objectives

The Dickman field, Kansas located in the US mid-continent provides two possible CO_2 sequestration targets: a regional deep saline reservoir as the primary objective and a shallower mature, depleted oil reservoir serving as a secondary objective. The goal of this work is to characterize and simulate monitoring of carbon dioxide (CO_2) movement before, during and after injection.

As mentioned previously, the scaling issues from geology, flow simulation, and seismic need to be resolved to better assist 4D CCS monitoring. Although the previous studies integrated time-lapse seismic modeling of CO_2 sequestration, some researchers used flow simulator output to seismic modeling (Shekhar et al.,2006; Kumar et al.,2008). They did not however, introduce a realistic geological model with unconformity into the flow model. This flow to seismic process involves difficult issues of scaling and smoothness in geological, flow simulation, and seismic earth models. This dissertation compensates this re-gridding process for a complex and realistic geological model with an unconformity, pinch-out and truncation embedded in the flow simulation model, and interprets it accurately into seismic modeling. The hypothesis of this work is that for a hard rock carbonate reservoir as a potential CO_2 capture and storage site at the mid-continent with extensive geological features, a CO_2 plume could still be mappable from 4D seismic. An algorithm is developed and the evaluation of the effectiveness of 4D seismic for a long-term monitoring of CO_2 storage is also conducted. This work is innovative according to previous summary and summarized as follows:

1. Dealt with a realistic geological model with unconformity into flow simulation model
2. Performed flow to seismic simulation (resolved the difficult scale issues from geological model, flow simulation to seismic earth models)
3. Compared three different seismic simulation methods:
 - a simple and ideal interface between sand and shale to study reflectivity change due to CO_2 injection (Zoeppritz equations)
 - 1D convolutional forward modeling
 - 2D acoustic and elastic forward modeling

Previous investigations and research objectives

Overall, by using these three different simulation methods, the simulated seismic response before and after CO_2 injection can help evaluate 4D monitoring.

2. THE DICKMAN FIELD

2.1 Geological setting

The Dickman field located in Ness County, Kansas, U.S.A, is a representative of the Western Interior Plains (WIP) aquifer system as a CO_2 sequestration candidate (Figure 2.1). The WIP system consists of a lower Ordovician and Cambrian carbonate unit, a middle unit of Mississippian and Devonian shale, and an upper Mississippian carbonate unit. The upper unit provides water drive for carbonate and clastic petroleum reservoirs at the Mississippian and Pennsylvanian boundary, hence representing the primary target for CO_2 injection (Liner *et al.*, 2011). The Dickman field (Figure 2.2) covers 17 square kilometers with surface

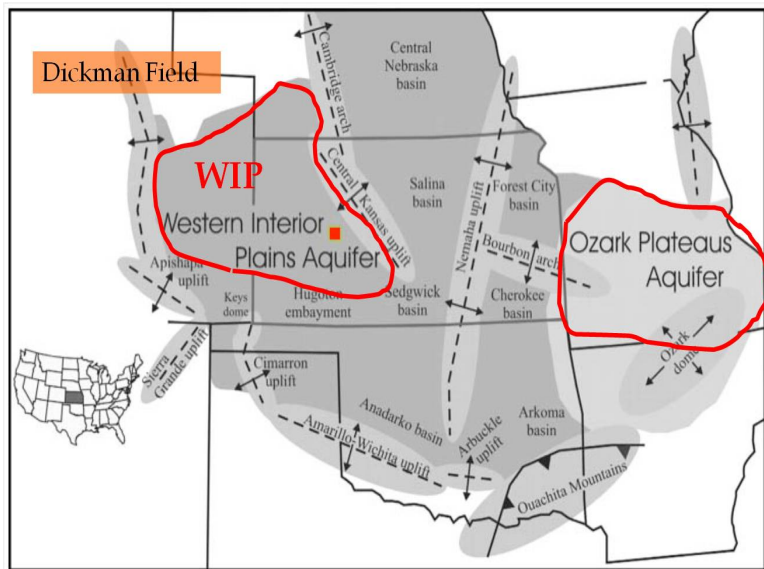


Figure 2.1. Lower Paleozoic aquifer system and the Dickman field location. After Carr *et al.* (2010).

elevation from 700-730 meters above sea level. It has produced about 1.7 million barrels of oil since its discovery in 1962. Oil reservoirs are fractured and solution-enhanced shelf carbonates of Mississippian age, producing from a small structural closure with original

oil-water contact at about 600 meters subsea and maximum oil column of about 10m. The two main CO_2 sequestration targets include this shallow depleted oil reservoir and the deep saline aquifer (Figure 2.3). The stratigraphic section for the depleted oil reservoir hangs on middle Pennsylvanian Fort Scott Limestone of the middle Pennsylvanian age, covering a stratigraphic interval from middle Pennsylvanian to lower Mississippian, including part of the WIP aquifer.

A regional unconformity separates middle Pennsylvanian strata from middle Mississippian carbonate below, representing a depositional hiatus of 30 and 40 million years (Zeller, 1968). The Pennsylvanian section in our study interval is about 40m thick, consisting of inter-bedded elastics and carbonates, and a minor sandstone pay-zone in the base Pennsylvanian channel-fill, locally named the Lower Cherokee Sandstone. The depleted carbonate reservoirs below the Mississippian unconformity are about 10m thick, including the Spenger Limestone and the upper part of the Warsaw Limestone formation. The deep saline reservoir, is a secondary CO_2 injection simulation target 40-60m thick, that includes Osage carbonates and part of the Gilmore City Limestone.

Our Dickman data set consist of 3D seismic survey, digital log curves, and limited core data (Table 2.1). Figure 2.4 illustrates that a karst surface exists at the contact between porous Mississippian limestone and the overlying seal, with a high conductive channel feature at the Mississippian/Pennsylvanian unconformity (Liner *et al.*, 2009).

Dickman Field Geological Setting

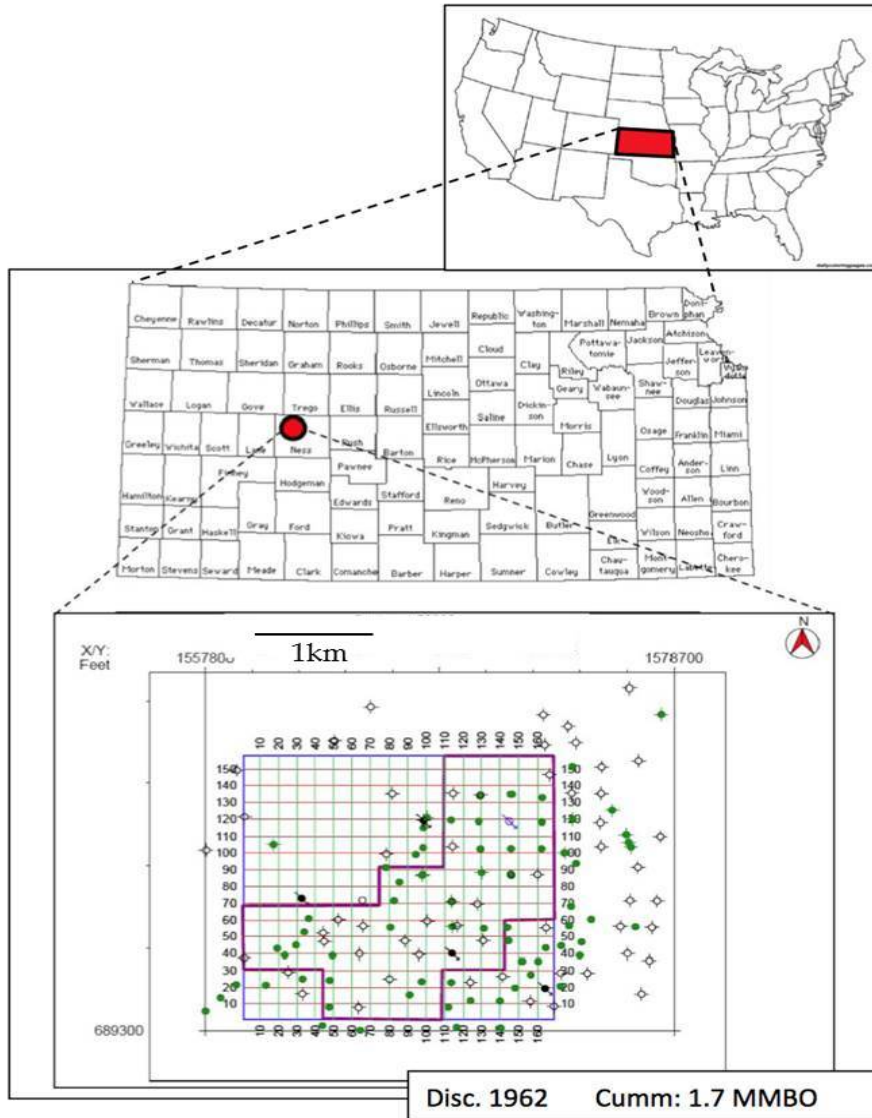


Figure 2.2. The Dickman field site and data available (wells locations and seismic outline)

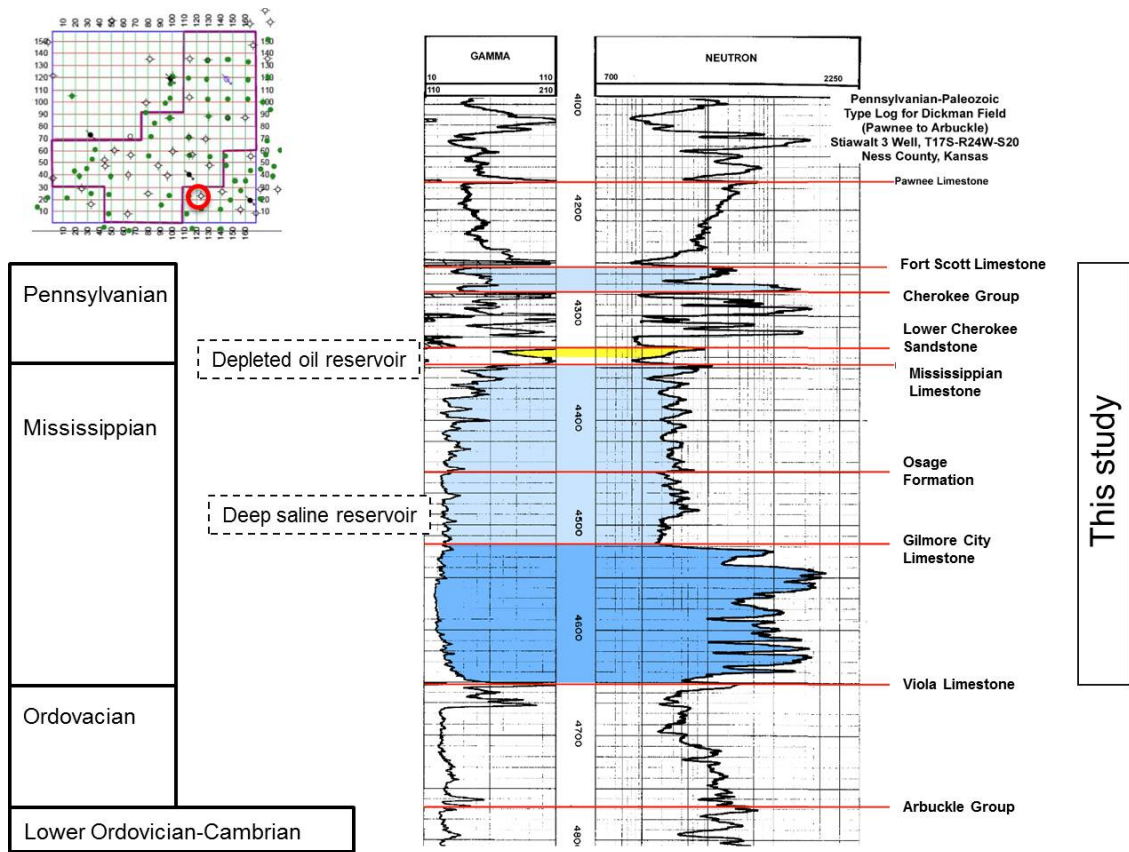


Figure 2.3. Annotated type logs for Dickman project area (Liner *et al.*, 2009).

Table 2.1. Data available in the Dickman field

Current data available in the Dickman field				
3D Seismic	8.6 square km			
Wells	142 wells			
	54 in 3D area	45 with logs	7 with cores	3 deep saline aquifer penetration
		GR(43)		
		Resistivity(25)		
		Neutron (27)		
	P sonic (6)			
	Density(6)			

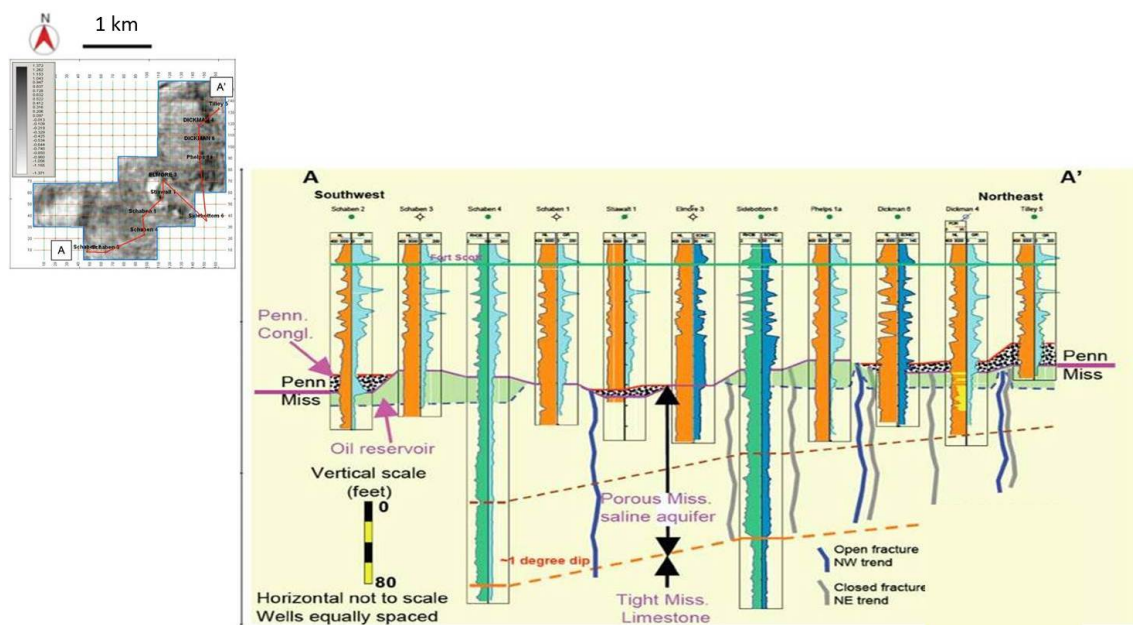


Figure 2.4. 3D seismic area, time slice at the Mississippian, and profile A-A' (Liner *et al.*, 2009). Cross section courtesy of Tom Bjorklund.

In this work, a 3D geological property model was created by the geologist in the group from the existing well logs and core data (Figure 2.5). Seismic interpretation and impedance volume have been used as guidance for structural mapping. Seismic interpretation was done in SMT Kingdom by previous researchers associated with this project, and porosity maps are obtained from digital well logs correlation with Petrel from Schlumberger. Core analysis was employed to construct a 3D porosity and permeability model for different formation. The 3D geological property (porosity and permeability) modeling work flow from digital well logs and core analysis is shown in Figure 2.6. This modeling process utilized the raw data from cores (core permeability and porosity), logs (neutron porosity, density and velocity), and core measurements within the same stratigraphic target from other fields. This work flow starts with the calibration of neutron logs scaled based on the limestone matrix to represent the porosity of different lithologic units or sandstone-shale inter-beds, cherty dolomite and dolomite. The porosity logs in 18 wells over the entire target strata were then calibrated using the core porosity measurements and the neutron porosity log from the Mississippian cherty dolomite reservoir. Combining these two steps will help compute porosity logs to be used in the property model. For the permeability modeling, the first step is to identify if the permeability is isotropic from the vertical and horizontal permeability measurements, in this study, a single permeability is first derived from the computed porosity logs for the property modeling; the next step is to consider permeability anisotropy due to existence of sandstone/shale inter-beds; and combined analysis above is used to compute the permeability for the property model. The final step is to use the seismic impedance to guide the permeability through the Osage saline aquifer where there are limited porosity data points. The obtained porosity and permeability gridded models are the input for flow simulation model. Furthermore, these property models have been validated by the oil/water production history match (Liner *et al.*, 2011), introduced in the

later section. There are additional well logs outside the 3D seismic data boundary, and the digital logs curves are interpolated to compensate the areas where there is no seismic data (Figure 2.7). This flow model grid is extended to the underlying saline reservoir, and served as input to the seismic simulation.

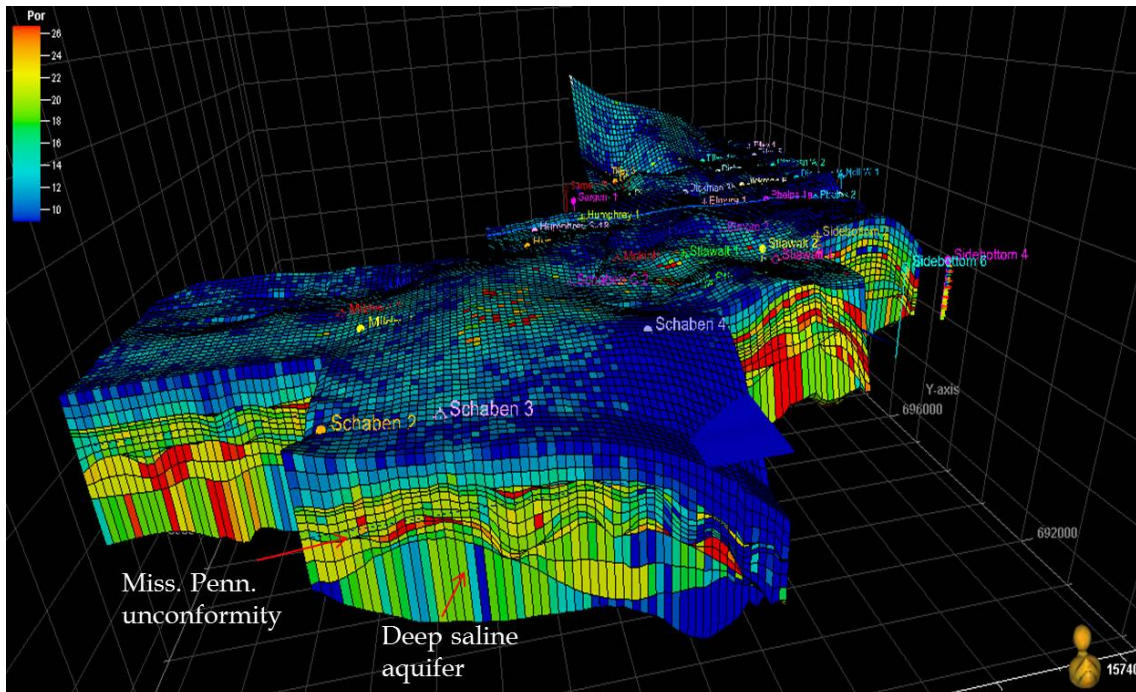


Figure 2.5. Three-dimensional gridded property (porosity) model, courtesy of Jianjun Zeng.

2.2 Flow simulation

The object of flow simulation in this study is to monitor CO_2 movement and help determine an optimal injection process to maximize CO_2 trapping. The compositional reservoir simulator GEM from CMG (Computer modeling group) is used in this study. Several studies report using CMG GEM for CO_2 sequestration simulation in deep saline reservoirs (Nghiem *et al.*, 2004; Noh *et al.*, 2004; Kumar *et al.*, 2005; Kumar and Bryant, 2008). GEM has also

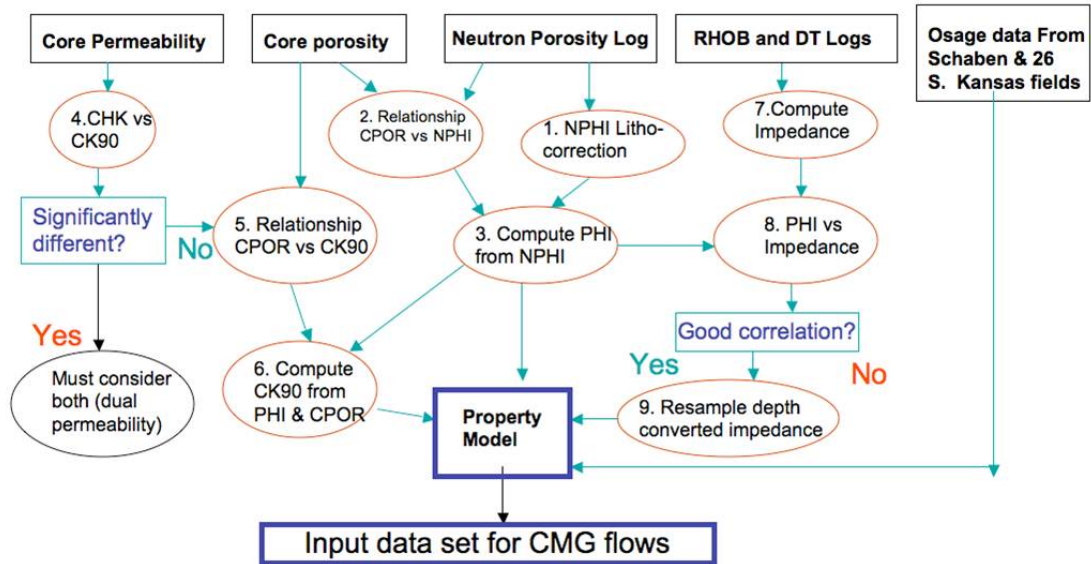


Figure 2.6. Work flow and the risk assessment in processing raw data from various sources for porosity and permeability modeling as input for CMG flow simulator, courtesy of Jianjun Zeng.

been used in CO_2 enhanced oil recovery (EOR), CO_2 storage in depleted reservoirs and enhanced coal bed methane simulation (Law *et al.*, 2003).

For the Dickman Field, the history-matched flow simulation model consisted of five layers bracketing the oil reservoirs as shown in Figure 2.8. Once calibrated by oil/water production history matching (Liner *et al.*, 2011), shallower layers were added to provide an overburden (Layers 1 to 8) for CO_2 leakage and containment scenarios. Table 2.2 shows the relationship between simulation layers and geological units. In this study, flow simulation grid cells are 150×150 m in (x-y) and have 32 layers with variable thicknesses in z. Permeability was obtained from core analysis, and it assumes that the ratio of vertical permeability and horizontal permeability is 0.7 for carbonate and 0.5 for sandstone (Figure 2.9). In this model, we simulate a single vertical well perforated in the deepest layer, with CO_2 injection of around 384 tons per day (Figure 2.10). To validate and calibrate the flow model, history

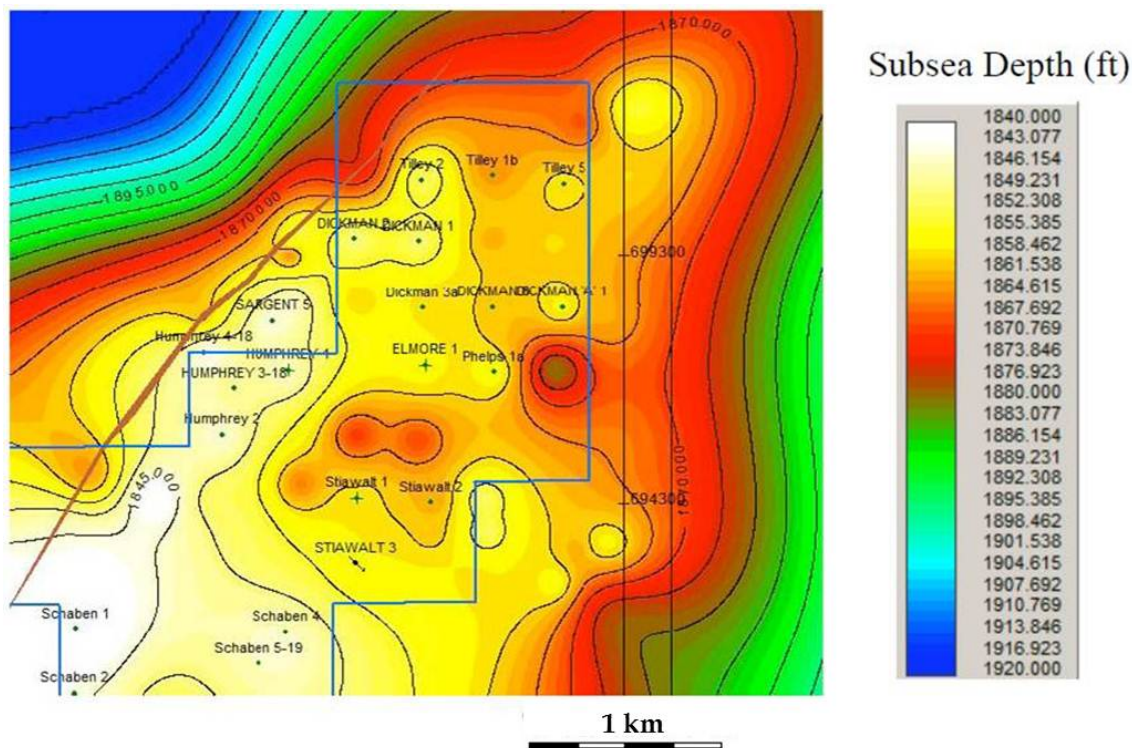


Figure 2.7. Map view for top of Fort Scott Limestone unit. The locations of wells with digital log data are displayed and the blue lines are 3D survey boundaries. After Liner *et al.* (2011)

matching of fluid production with 15 production wells was conducted (Figure 2.11). The well Dickman 4 was assumed to have been injected with all produced water back to the reservoir, which shows matching on both oil and water productions on the production wells around Dickman 4 well. In summary, with slight adjustment in the net pay zone thickness, well perforation length and reservoir relative permeability, A good history matching has been obtained, as shown in Figure 2.12 which validates our geology model (Liner *et al.*, 2011).

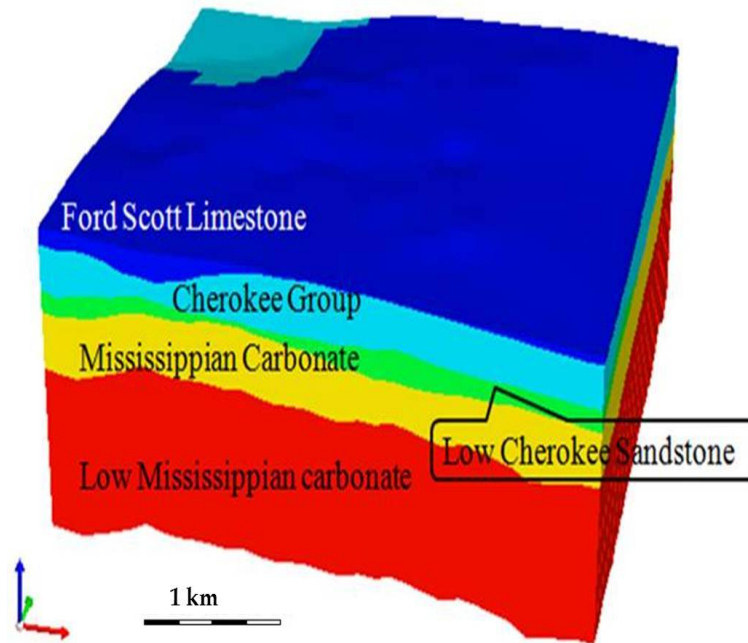


Figure 2.8. The five layers flow simulation aquifer model. After Liner *et al.* (2011)

Table 2.2. The relationship between the simulation layers and geological layers

Sim Layer No.	Vertical Perm	Porosity(%)	Formation Name
1-6	10md	18.2	Shallow reservoir layers
7-8	0.01md	20	Two seal layers
9-10	0.7 Horizontal Perm	10.3	Fort Scott Limestone
11-13	0.5 Horizontal Perm	19.1	Cherokee
14-15	0.5 Horizontal Perm	16.5	Lower Cherokee
16	0.7 Horizontal Perm	14.8	Mississippian Unconformity
17-24	0.7 Horizontal Perm	20.0	Mississippian Porous Carbonate
25-32	0.7 Horizontal Perm	22.5	Mississippian Osage and Gillmore City

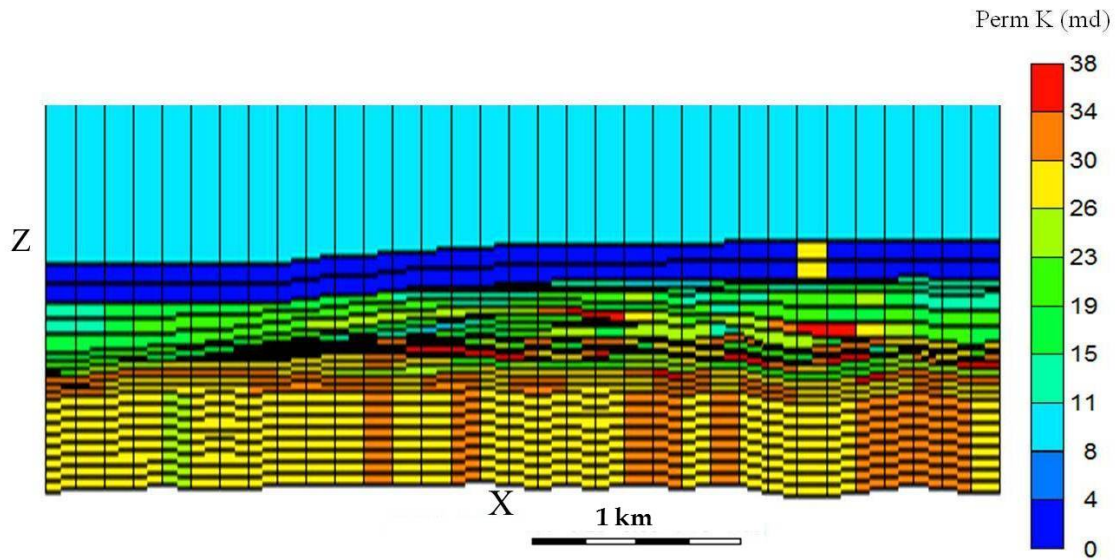


Figure 2.9. Cross-section view of the 32-layer Dickman flow simulation permeability model. Grid block have uniform XY size (152 x 152m) and variable thickness (Liner *et al.*, 2011).

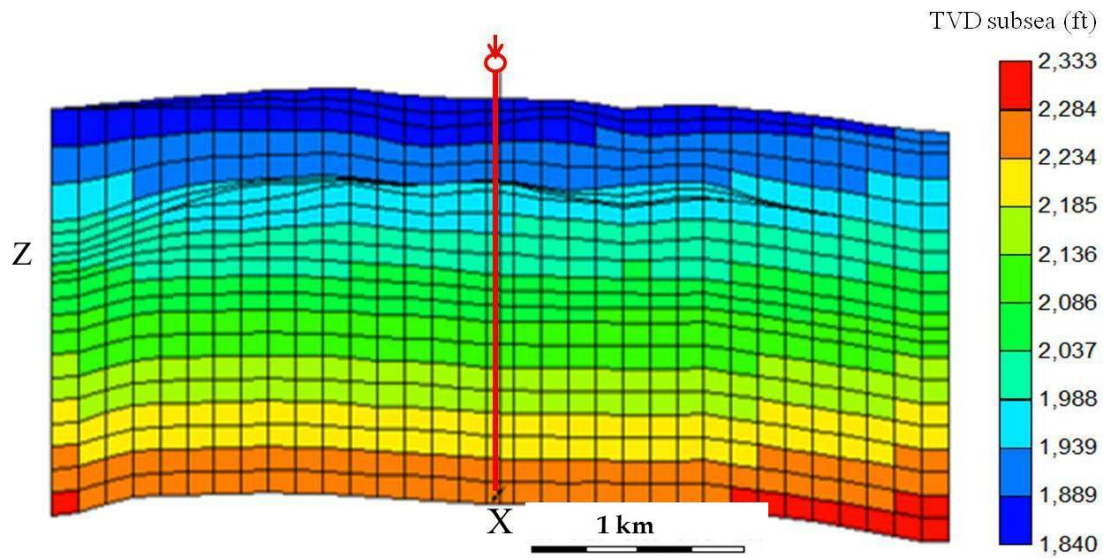


Figure 2.10. Vertical CO_2 injection well arrangement. The well (red) is perforated in the bottom layer (Liner *et al.*, 2011).

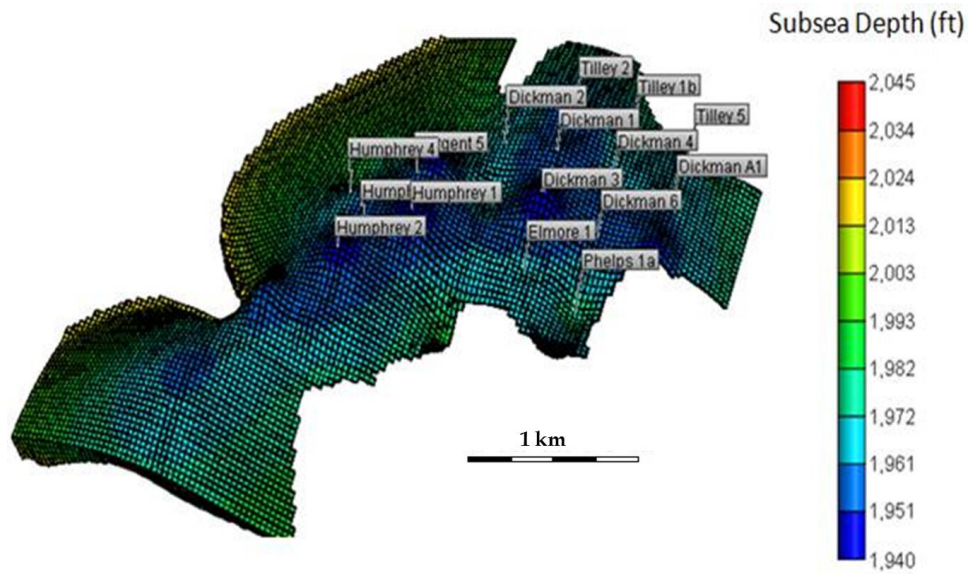


Figure 2.11. Fifteen production wells and one injection well (Dickman 4) are used for the production history match (Liner *et al.*, 2011).

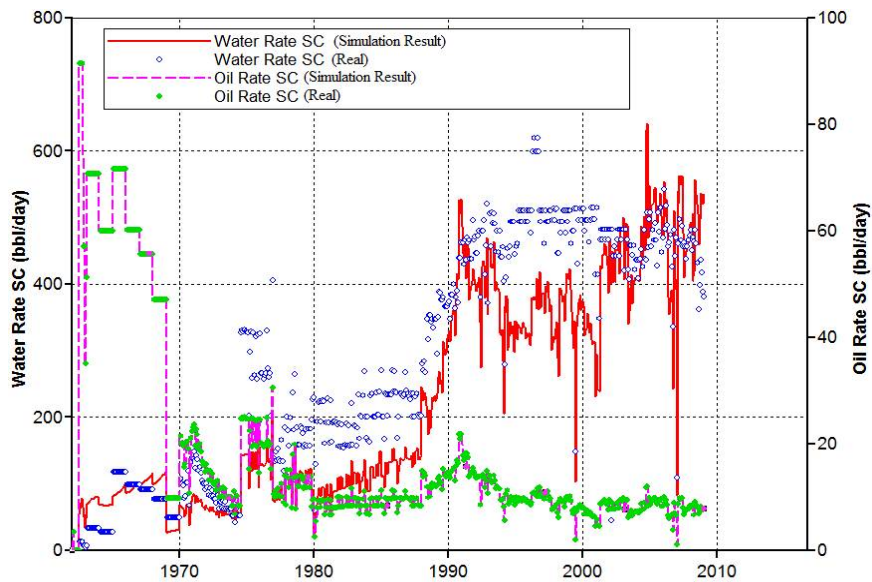


Figure 2.12. A good matching on both oil production rate and water production rate was obtained, which gives confidence of our geological model (Liner *et al.*, 2011).

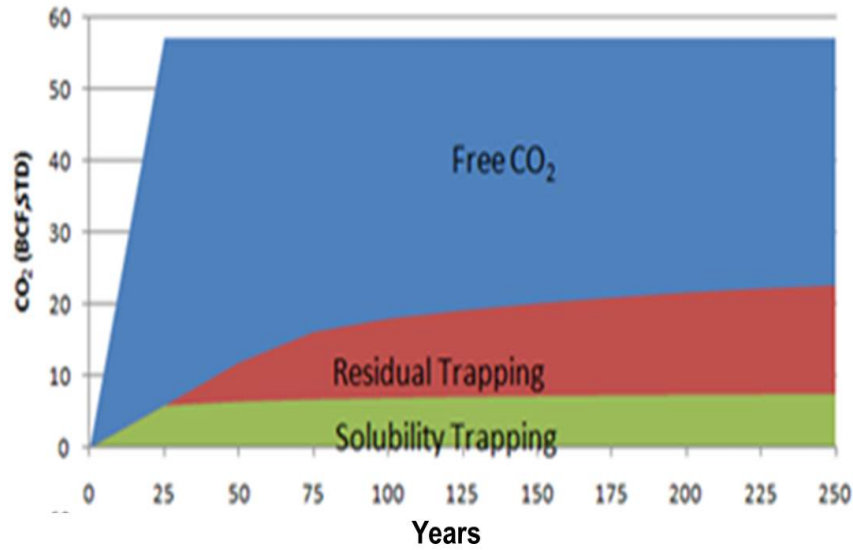


Figure 2.13. Standard CO_2 trapping amount by three different trapping mechanisms in the Dickman field in 250 years time interval (Liner *et al.*, 2011)

In this work, CO_2 is trapped by three different trapping mechanisms: solubility trapping, residual trapping, and hydrodynamic (free CO_2) trapping (Figure 2.13) during 250 years flow simulation interval.

The general workflow from geologic structure, flow simulation, and seismic simulation is shown in Figure 2.14. This process will bring the scale issues into consideration, which is the main investigation for this dissertation.

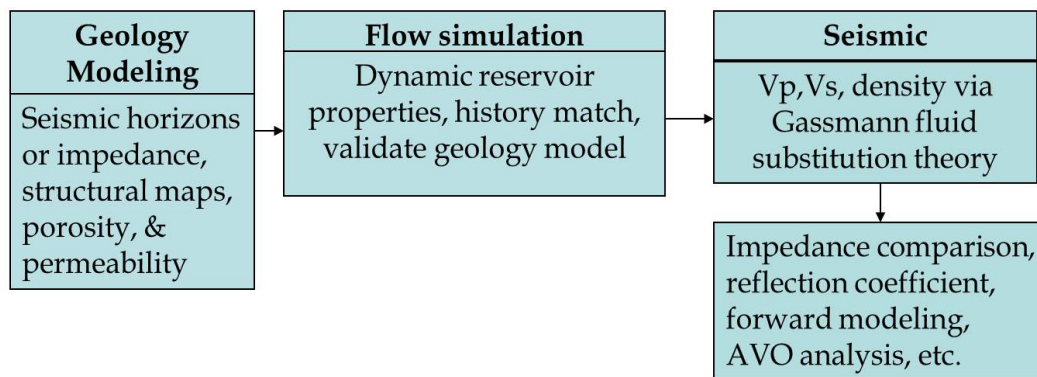


Figure 2.14. A summarized general work flow from geological modeling, flow simulation to seismic simulation.

3. GASSMANN FLUID SUBSTITUTION

3.1 Nature of flow simulation grids

In the flow simulation simulators, two type of grids are generally used: unstructured and structured. Generally the structured grid, including orthogonal corner grid and non-orthogonal corner grid, is preferred because it can improve the simulation performance. The orthogonal grid is more simple in modeling if there are not many faults in the geologic model. However, for a complicated faulted reservoir, a non-orthogonal corner grid may be necessary since it can provide a better approximation of the reservoir geometry and structure. For the purpose of this work, the orthogonal corner grid is sufficient (Liner *et al.*, 2011).

The flow simulation output is composed of several reservoir property grids at different time intervals. Each grid block contains a set of reservoir properties including: XY position (ft), depth (ft), pressure (psi), porosity, and CO_2 saturation. In this study, it is assumed that porosity is constant during CO_2 injection and thus ignore long-term mineral trapping (Liner *et al.*, 2011).

Temperature is calculated for the Mississippian by (Carr *et al.*, 2010) and consistent pressure results are also obtained:

$$T = 0.004z + 55 \tag{3.1}$$

where z is depth in m and T in Fahrenheit. The calculated temperature in the Mississippian formation ranges from 33°C to 49°C, and pressure from the flow simulation model ranges from 8.5 MPa to 28 MPa. Figure 3.1 gives an overview of the average reservoir conditions and a few additional properties for the Dickman field. Under such conditions, CO_2 becomes a supercritical fluid (critical point: $T=31.1^\circ\text{C}$; $P=7.38$ MPa), which is ideal for carbon

dioxide capture and storage (Bachu, 2003; Bentham and Kriby, 2005). Figure 3.1 gives a CO_2 phase diagram for the Dickman field (orange zone). Details of calculations for different

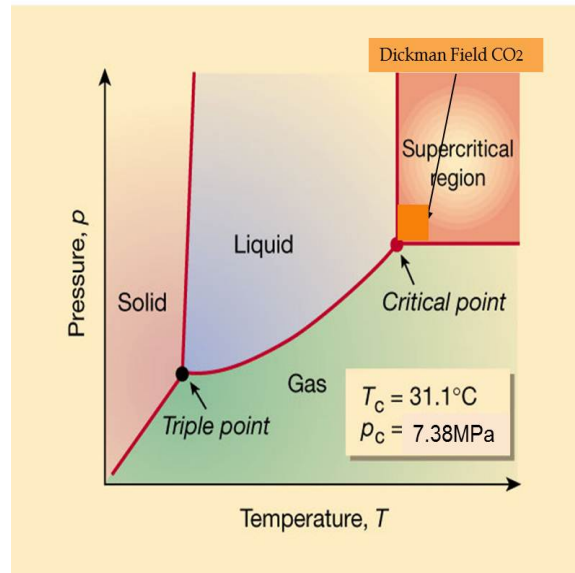


Figure 3.1. CO_2 phase diagram in the Dickman field (orange zone), which is above critical point and behaves like supercritical fluid. Modified from Leitner (2000).

variables are presented below.

3.2 Flow parameters in each cell

Once pore fluid properties are obtained, Gassmann fluid substitution is used to calculate fluid-saturated rock properties (Smith *et al.*, 2003). The input parameters for the Gassmann equation include bulk modulus for the porous dry rock (**Kdry**), solid mineral (**Kmin**), and fluid (**Kfluid**). The details can be found in the **Appendix A**.

The velocity calculated ranges from 2793m/s to around 5500m/s, the high velocities of which are mostly in the deeper units of carbonate. The calculation was coded in Matlab with input parameters as all aforementioned fluid properties, and the output of this program is the fluid saturated velocity and density in each cell.

Table 3.1. Comparison of Gassmann fluid substitution results

Fluid properties	Year 0	Year 250	Change by %
Pressure (MPa)	14.69	26.8	+45.2%
CO_2 saturation	0	0.8413	+100%
P wave velocity (m/s)	4344.9	3673.2	-15.5%
S wave velocity (m/s)	2711.5	2711.5	unchanged
CO_2 density(g/cm^3)	0	0.8322	100%
fluid saturated rock bulk modulus(GPa)	12.35	24.23	49%

The Gassmann code includes two parts: 1) parameters (reservoir properties) used to calculate \mathbf{K}_{dry} , then \mathbf{K}_{dry} is fixed and saved into a file; 2) explicit calculation \mathbf{K}_{sat} with the fixed \mathbf{K}_{dry} at each time step.

Table 3.1 gave some reference fluid properties from two different flow simulation years (year 0 and year 250) calculated by Gassmann fluid substitution theory. This example was taken from where the CO_2 saturation changes most, from 0 to around 84%. In this example, temperature as a function of depth remains changed, and shear wave velocity is kept constant with porosity of 18.4 %.

4. FLOW SIMULATION REGRIDDING

This section is the major contribution of this work. It incorporates different scaling issues from geology, flow simulation, and seismic forward modeling. From the early work as described in the previous section, a property grid is obtained with velocity and density of fluid saturated rock in each cell. However, this flow simulation property grid is too coarse for realistic seismic simulation, and the geologic structure has not been incorporated. Unconformities, truncations, and strata pinch outs, excluded in the flow simulation model to avoid zero thickness layers, need to be added back into the model to establish a regular 3D grid. Hence, the property grid has to be reconstructed to match the realistic geologic structure. The following steps are then performed to prepare flow to seismic procedure.

As introduced in **Chapter 2**, the flow simulation property grid has a set of properties contained in each individual '.txt' files shown in Figure 4.1. Each '.txt' file stores one fluid property such as depth, pressure, porosity, and saturation, etc. Each '.txt' file starts with x and y absolute coordinates, and property on the 3rd column (shown as an example of "depth" in Figure 4.1, which is different for each '.txt' file). The header words also provide the simulation run time (shown as red box in Figure 4.1), where **Time** is 0, meaning at the first year of injection. Property name and unit are defined on the 3rd column.

In order to decipher the data, the **first** step is to preprocess the files by skipping the headers and then combine all these property files into one single file. Since the minimum and maximum x and y coordinates are known (from the edges of 3D seismic data outline), for each data point, the indices of x and y can be calculated. This was realized by writing a C program included in the **Appendix B-1**. After this step, the output file shows the elimination of the header words, the correct index of x, y, corresponding z values, and combined properties (e.g. CO_2 saturation, porosity). These will be written into a new file

** TIME: 0						
** PROPERTY: Grid Paydepth						
** UNITS: ft						
** X and Y in Reservoir Coordinates						
<	X	>	<	Y >	<Layer	1>
	1562247.00			705023.00		150
	1562747.00			705023.00		150
** PROPERTY: Grid Paydepth						
** UNITS: ft						
** X and Y in Reservoir Coordinates						
<	X	>	<	Y >	<Layer	2>
	1562247.00			705023.00		450
	1562747.00			705023.00		450

Figure 4.1. Flow simulation output data format which has format of (x,y, property). It also provides simulation run time, property unit, and layer information.

with formatted x and y indices and properties (Figure 4.2).

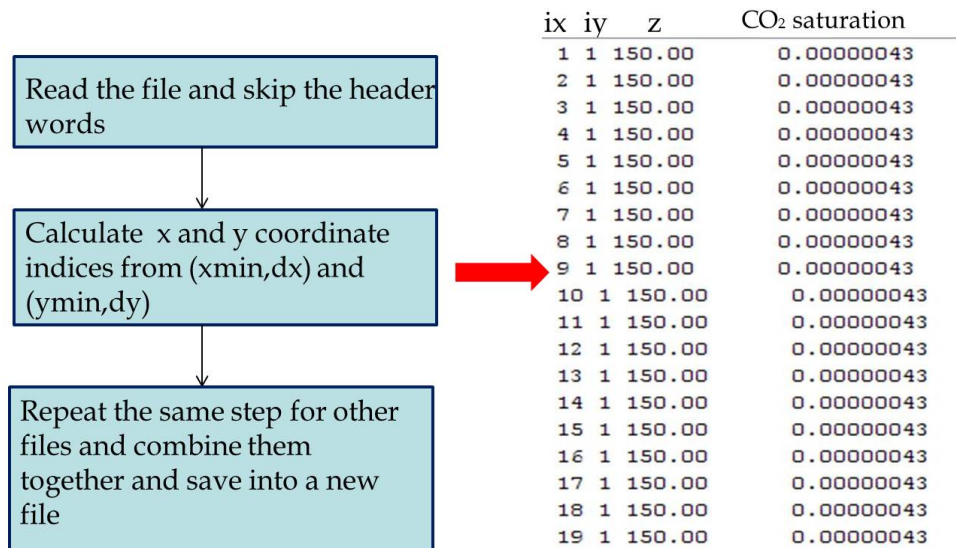


Figure 4.2. Step 1: Preprocess the data by eliminating header words and save all the properties into one file.

The 2nd step is to find the missing points (Figure 4.3). This realistic geology model has unconformity such as truncation and pinchout which will be eliminated during flow simulator output. For example, the numbers of grid points in (x,y,z) direction are known as (nx,ny,nz) respectively with the total number of cells of nx by ny by nz. However, this number is smaller than the total grid number used in flow simulation because the flow simulator was not able

to include these points due to the existence of zero thickness. To retain a regular 3D model, these missing points need to be added back with correct indices to reform a regular 3D model with number of dimensions of n_x by n_y by n_z . Notice that in Figure 4.3, for the first column ix , the missing indices are shown between x index number 4 to 8 in the red box. Once they are found, the missing points with correct x and y indices will be added back shown in Figure 4.4. This means that for a missing point thrown out from the flow simulator, it will have all x, y and z as well as other properties missing, reflected both on the (x,y) plane and (x,z) or (y,z) vertical section (Figure 4.4). After the indices for x and y have been assigned, the z and other property values will be treated but in different ways.

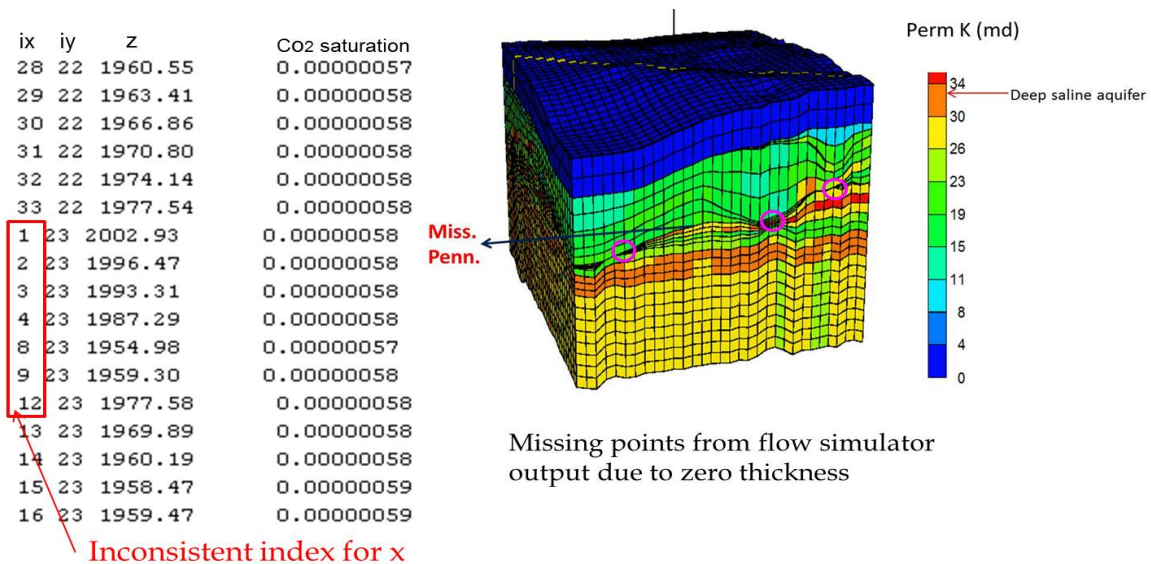


Figure 4.3. Step 2: Find the missing indices due to unconformity.

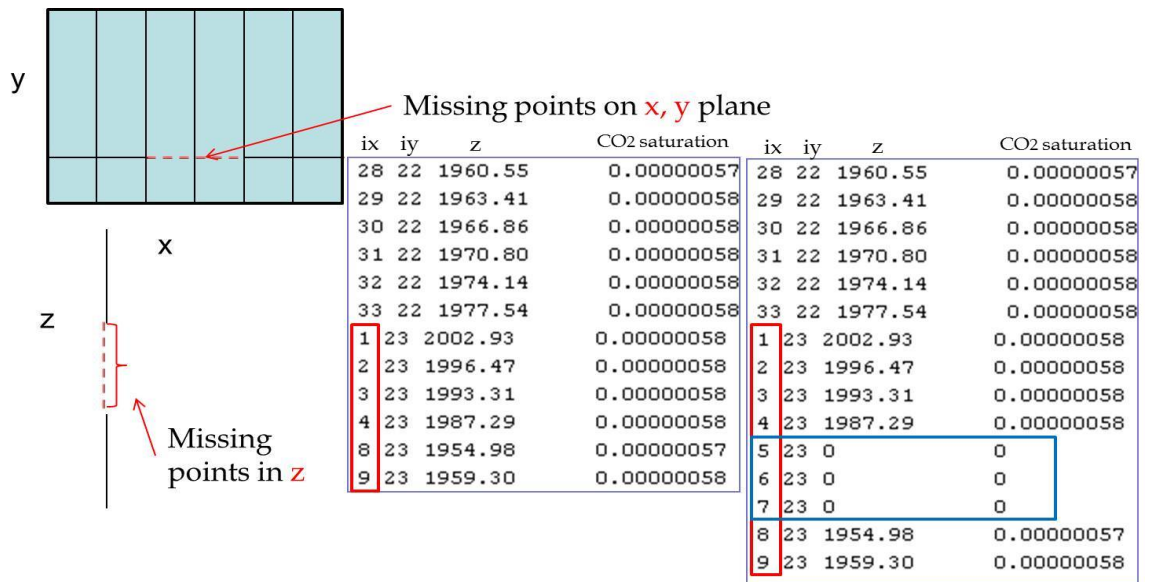


Figure 4.4. Step 2: After the missing points are found, add the x and y indices back and assign z as zero first

After this step, the 3D property grid has been reformed. In order to restore the correct depth and other properties for each missing point, the data format needs to be understood. The data from the flow simulator are layer-based: for each layer, the data is read from the x direction first then the y direction. The 3rd step is to rewrite the property grid into a matrix with the size of (nz, nx, ny) . The data can then be accessed from each layer first then each (x, y) plane (Figure 4.5).

The depth and other properties for the missing points can now be filled. The criterion is that for each layer if the depth is zero, the depth and any other properties will be assigned the same as the one for the layer above. Repeat this step for all the 32 layers, then the matrix will be all filled up where they were zero values.

Since the data points are not evenly spaced in z, the 4th step is to assign all these data points onto a regular grid (Figure 4.5). The irregular z spacing will not be compromised in the forward modeling method. A regular spacing in x, y, and z is necessary. This step may be tricky because when interpreting the reservoir properties from flow simulation output with varied spacing in z direction, data may be missing/unknown depending on the choice of the vertical cell size. For example, if two vertically adjacent points are 10m apart, and a 5m spacing is chosen, then the properties for the intermediate points will be unknown, and have to be obtained from the neighboring values through interpolation. On the other hand, if two vertically adjacent points are 2m apart for example, then 5m spacing will involve averaging neighboring values. In our flow model, native depth spacing varies from 0.15m to 90m, so the seismic cell size has to be carefully chosen to accommodate these issues. The easiest method is to set the vertical grid spacing as small as possible, i.e., the smallest spacing between two adjacent vertical points, to include all the subtle features that have been embedded in the cells. Intermediate points between every two layers after vertical regridding are top filled with known data points (Figure 4.6). However, choosing

the smallest spacing between any points in dz may cause the sharp edges of inconsistent lateral variation in the velocities, which may later greatly affect acoustic and elastic forward modeling results. Besides, too fine grid size that includes too much detail will also increase the computational cost. To this end, a reasonable choice of dz becomes important.

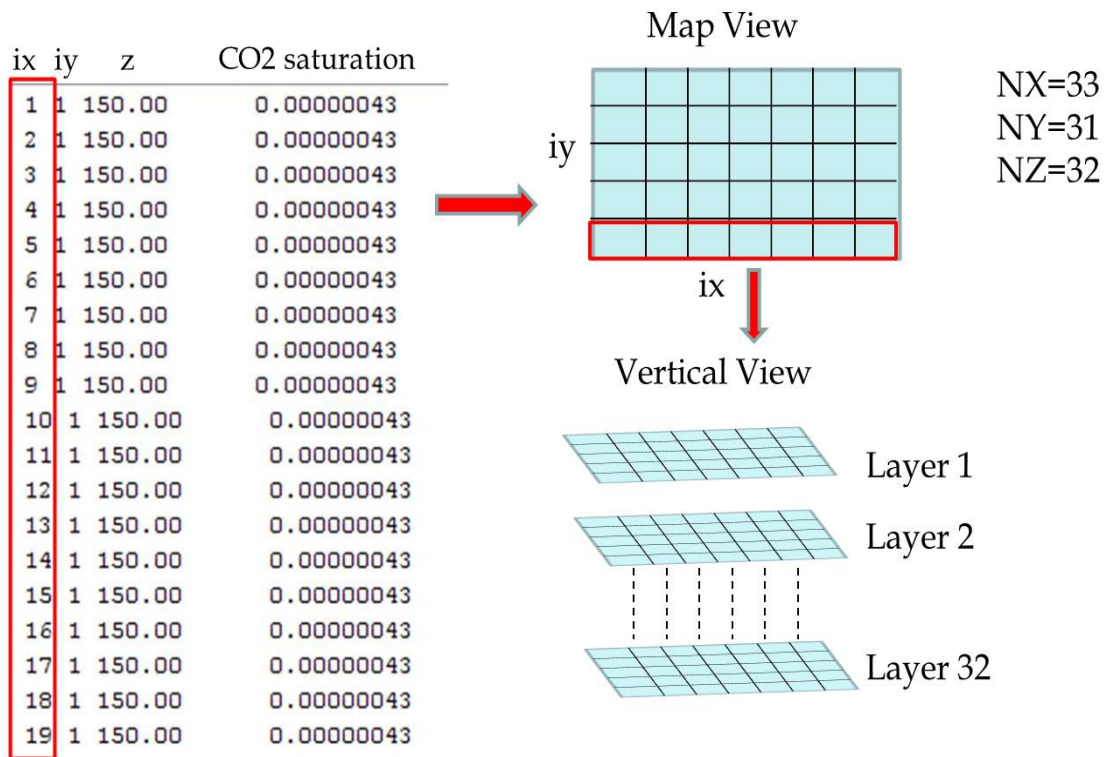


Figure 4.5. Step 2: The correct indices for x and y have been added back, but leave the z values or other properties as zero. This will be matched or added by the layers above and below. Step 3: rewrite the matrix with dimension of (nz,nx,ny)

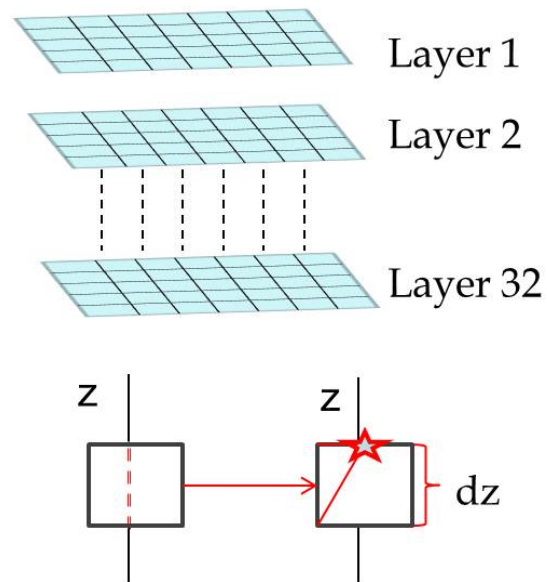


Figure 4.6. Step 4: for 32 layers, the depths at the missing points from flow simulation model are the same.

After vertical regridding process is completed, the 5th step is to interpolate the coarse horizontal grid into a finer seismic bin size. For the x-y direction, the flow simulator cell size is regular of 150m in both directions. Compared with the 3D seismic dataset for the Dickman field, the bin size is 25m by 25m. To make the seismic simulation results coincident with it, spacing in both x-y directions is set at 25m. The interpolation starts from the x direction from the original 150m spacing into 25m spacing, and then the matrix will be sorted to y direction. Then perform the same interpolation in y direction from 150m to 25m as well, and the data can be sorted back again in the x direction. After all these steps are complete, the simulated seismic response has a data range as shown in the Figure 4.8.

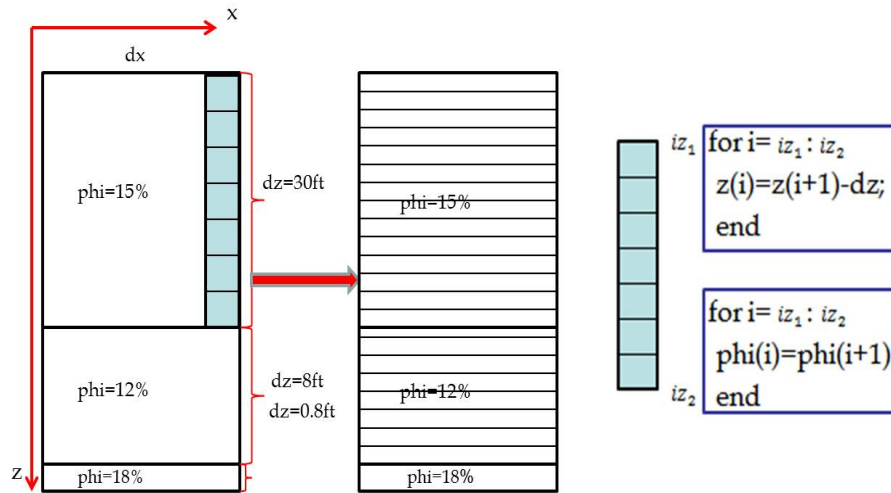


Figure 4.7. Step 5: Fill the data points between two adjacent values when dz is chosen.

For different seismic simulation methods, the spacing in x and y direction needs to be adjusted. For **1D** convolutional forward modeling, we focus on the one dimensional changes in z, so 25m spacing may be adequate; but for **2D** acoustic and elastic forward modeling, 25m may be too large that will induce numerical dispersion, so it has to be interpolated into a finer scale.

In summary, the procedure of flow to seismic regridding is as follows:

1. find the missing points from inconsistent x and y coordinates
2. add these points back with correct x, y and assign their depths to zero
3. establish the regular n_z by n_x by n_y 3D matrix
4. for each iz ($iz=0, n_z-1$), find the points where depth is zero and assigned the depth value of the adjacent point from the layer above
5. after all the data points with depth zero assigned, find the minimum and maximum depths (z_{min} and z_{max})
6. determine the minimum and maximum spacing between the data points in z , and assign minimum spacing value as dz
7. for all the depth points, calculate the corresponding depth indices for given the depth range from z_{min} to z_{max} and dz ($new_{NZ} = (z - z_{min})/dz$), and these are the new depth indices.
8. for the cell which has no property values due to inconsistent new depth indices, fill the same properties in from one depth index (iz_2) to the next one above (iz_1); for the values in depth, assign these points in each cell with increment dz
9. do the interpolation in x first then y (downscale to seismic bin size)

Part of the realization of this process is coded in Matlab included in **Appendix B-2**.

Overall, the flow grid is regular in $x - y$ and irregular in z , i.e., all grid blocks have the same $x-y$ size but variable thickness. The desired seismic grid is regular in $x - y - z$. The flow grid (dx, dy) is much larger than the seismic grid (dx, dy), which requires a downscaling of the flow grid to the seismic grid interval. In the vertical direction things are more complicated.

The irregular flow grid dz can range from zero (unconformity) to the scale of 30m, while the seismic grid is desired to be regular and in the scale of 1-3m. Depending on the thickness of each individual block, it may require either upscaling or downscaling, and missing section must be addressed carefully since every point in an earth model for seismic simulation must contain parameter values.

5. SEISMIC SIMULATION METHODS

5.1 PP and PS reflectivity

PP and PS reflection coefficients with different incident angles have been investigated by many researchers in the past (Veire and Landro, 2011). It has been a useful method to detect the AVO effect due to the different fluid properties. The most fundamental concept came from Zoeppritz equation, and many implied forms or approximations have been brought up for different purposes (Jin, 1999). In this study, an ideal two layered model with sand and overlying shale was built to study how the fluid content would affect the PP and PS reflectivities as well as the sensitivity for the V_p and V_s velocities. The PP and PS reflectivities are calculated from Aki and Richard's approximation:

$$R_{pp} = \frac{1}{2}[1 - 4\gamma^2 \sin^2 \theta_p] \frac{\Delta \rho}{\rho} + \frac{1}{2 \cos^2 \theta_p} \frac{\Delta V_p}{V_p} - 4\gamma^2 \sin^2 \theta_p \frac{\Delta V_s}{V_s} \quad (5.1)$$

$$R_{ps} = 2 \frac{\sin \theta_p}{\cos \theta_s} [\gamma^2 \sin^2 \theta_p - \gamma \cos \theta_s \cos \theta_p] \frac{\Delta V_s}{V_s} - \frac{\sin \theta_p}{2 \cos \theta_s} [1 - 2\gamma^2 \sin^2 \theta_p + 2\gamma \cos \theta_s \cos \theta_p] \frac{\Delta V_p}{V_p} \quad (5.2)$$

where $\Delta V_p = V_{p2} - V_{p1}$, $V_p = (V_{p1} + V_{p2})/2$ (similar for V_s and ρ), $\gamma = V_s/V_p$.

For different incident angles (either PP or PS), the reflectivities can be studied to help identify the different features of PP and PS waves, and determine how they would differentiate reservoir properties.

5.2 *Seismic simulation methods*

There are many approaches for seismic simulations. In this study, three different methods were used: 1D convolutional forward modeling, and 2D acoustic and elastic finite difference forward modeling.

5.2.1 *One-dimensional convolutional forward modeling*

The 1D convolutional model is based on the assumption of an isotropic and layered earth. When waves propagate through the earth, the seismic wavelet $w(t)$ will convolve with the earth reflectivity $r(t)$ to obtain seismic trace $d(t)$,

$$d(t) = w(t) * r(t) + n(t) \quad (5.3)$$

where $n(t)$ is noise. The 1D convolutional forward modeling assumes that the data has only primary reflections.

The regridded CMG simulator outputs are imported to in-house Matlab routines implementing the Gassmann equation to calculate fluid-saturated rock velocity and density in each simulation grid cell (as a function of time). Our approach uses a 1D convolutional model in which computed normal-incidence reflection coefficients are convolved with a seismic wavelet. To obtain the reflectivity in each cell, acoustic impedance is calculated by:

$$I = \rho_{sat} V_{sat} \quad (5.4)$$

then the reflection coefficients are obtained by:

$$R_o = \frac{I_n - I_{n-1}}{I_n + I_{n-1}} \quad (5.5)$$

where I_n is impedance for the n^{th} layer. The calculated reflectivity in each cell will be converted from depth to time using fluid-substituted rock velocity. The reflectivity time series is re-sampled and convolved with a seismic wavelet to obtain 3D zero-offset seismic cube. Overall, the work flow is as follows:

1. read in all property values (depth, porosity, saturation, etc.)
2. calculate the initial mineral bulk modulus with different mineral composition
3. calculate bulk modulus for different fluids (CO_2 , brine)
4. compute the initial bulk modulus (K_{sat}) for saturated rock
5. calculate the bulk modulus for the porous rock frame K_{dry} with the initial K_{sat}
6. update K_{sat} using Gassmann's equation with fluid substitution
7. calculate the velocity and fluid-saturated density for the saturated rock
8. regriding in (x,y) plane first and then in z direction
9. compute impedance with fluid saturated density and velocity
10. calculate the reflectivity at each cell and perform the depth to time conversion using the only time-depth functions available from the well Elmore 3
11. re-sample the reflectivity time series and convolve with Ricker wavelet to generate seismic dataset

The simulated seismic response for this method can produce a 3D seismic cube. Depth slices can be obtained for comparison for different CO_2 saturation.

5.2.2 Two-dimensional convolutional acoustic and elastic forward modeling

In this study, 2D acoustic and elastic finite difference forward modeling methods were used to study the 2D seismic data.

At the initial stage of this work, the forward modeling code **Sufdmod2** for acoustic and **Suea2fd** for elastic in the software package **Seismic Unix (SU)**(Cohen and Stockwell, Cohen and Stockwell) were employed. The former used 2^{nd} order approximation in both time and space while the latter used 2^{nd} order in time and 4^{th} order in space for finite difference forward modeling. Compared with one-dimensional convolutional forward modeling which primarily focuses on one dimensional in the z direction, 2D acoustic and elastic forward modeling performs wave propagation in a 2D plane. Elastic finite difference modeling can also generate both P and S wave reflections.

Before moving forward to the forward modeling methods, the input velocity grid may need to be interpolated into a finer grid to reduce artifacts caused by numerical dispersion. The stability of this numerical solution relies on the choice of parameters that include grid spacing (both x or y and z), minimum velocity value and frequency:

$$f_{max} = v_{min}/(10h) \tag{5.6}$$

$$f_{peak} = f_{avg} = f_{max}/2 \tag{5.7}$$

where v_{min} is the minimum velocity value, h is vertical spacing, and f_{max} is maximum frequency. When running this program in **SU**, the program will illustrate the data information, and so the parameters can be changed or modified.

For 2D acoustic forward modeling, the algorithm is straightforward and can be used to model wave propagation accurately in general media (Etgen and O'Brien, 2007). Here lists

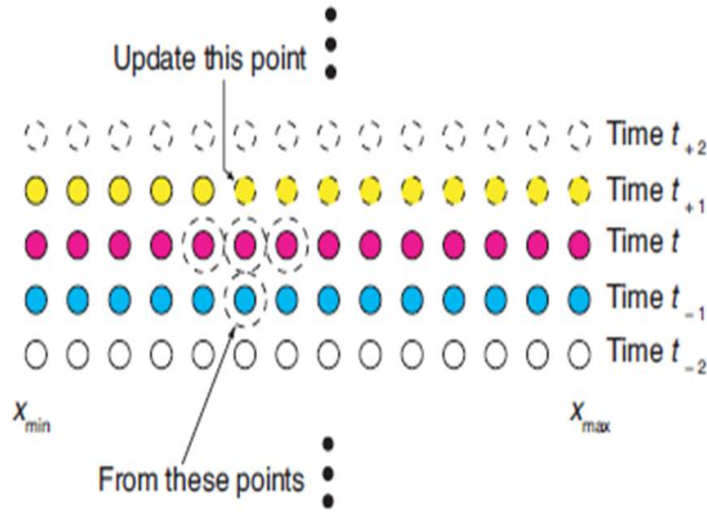


Figure 5.1. For computation for each dashed dots, it requires 4 points at the $(x - \Delta x), x$, and $(x + \Delta x)$ at the time sample t ; plus the data point at the previous time sample $(t - \Delta t)$. Modified from Etgen and O'Brien (2007)

the general scheme for calculating the wave propagation with 2^{nd} order in space and 2^{nd} order in time. Starting with the 1D constant density wave equation:

$$\frac{\partial^2 u}{\partial t^2} = v^2(x) \frac{\partial^2 u}{\partial x^2} \quad (5.8)$$

Expand this using finite difference, then it becomes:

$$u(x, t + \Delta t) = v^2(x) \frac{\Delta t^2}{\Delta x^2} [u(x + \Delta x, t) - 2u(x, t) + u(x - \Delta x, t)] + 2u(x, t) - u(x, t - \Delta t) \quad (5.9)$$

This means that in order to get the data point for the next time sample $u(x, t + \Delta t)$, four points are used as shown in Figure 5.1. The surrounding wavefield points (three purple dots and one blue dots) are needed to calculate the yellow dot above. For the data at the edges, boundary conditions such as free surface, absorbing boundary are applied.

At the later stage of this work, a flux-corrected transport correction applied to the 2D elastic wave equation for finite difference modeling in anisotropic media named **Sufctanismod** was applied. This method was first developed by Boris and Book (Boris and Book, 1973; Book and Hain, 1975) based on the solution of the continuity equation in hydrodynamics. Since the conventional finite difference methods suffer from the numerical dispersion from the coarse grid, this method is an efficient alternative for obtaining finite-difference solutions to the wave equation on coarse grids with no numerical dispersion (Fei and Larner, 1995). This method includes two steps: the first step is conventional finite difference simulation, and the 2nd step is diffusion and anti-diffusion used for correction of the wavefield caused by the numerical dispersion. Diffusion is first applied to the field where the numerical dispersion occurs due to no prior information, and then anti-diffusion is applied to counteract to the field where no correction is needed. The algorithm was developed to perform a nonlinear local search for extrema at the two adjacent points, and anti-diffusion will not be applied to these points. The issue with this method is that the amplitude loss during diffusion will not be compensated by the anti-diffusion when there is no local extrema, which may bring some amplitude distortion at these places (Fei and Larner, 1995).

Due to the algorithm limitation, the previously mentioned **Suea2df** seem not to be able to provide very reliable results which induce lots of artifacts and noise embedded in the code. **Sufdmod2** can provide relatively reliable results that have been used to compare with the **1D** convolutional forward modeling results in the **Discussion** session.

6. RESULTS AND DISCUSSIONS

6.1 *PP and PS reflectivity*

In this section, CREWES Zoeppritz Explorer and Gassmann fluid substitution were used to calculate PP and PS reflectivity with different CO_2 saturation. A simple two-interface model with overburden shale is shown in Figure 6.1. This is an ideal case for Pennsylvanian shale in direct contact with Mississippian carbonate. This test shows how the seismic properties are affected by the CO_2 injection in the carbonate.

Given the average reservoir condition for the Dickman field ($T=33.7^\circ$, $P=13.8\text{MPa}$), these tests use a trial of CO_2 saturation values to obtain different V_p , V_s and fluid-saturated densities. The mineral content is kept the same as a combination of 30% calcite and 70% dolomite with porosity is averaged from the field as 20%. Gassmann fluid substitution is then applied to substitute brine for CO_2 with saturation changing from 0.1 to 0.8. From the well Humphery 4-18 DT log, the V_p of Pennsylvanian shale has a range of 2950-4080m/s with an average of 3600m/s and the corresponding V_s has a range of 2955-2833m/s and an average of 2840m/s is used. For the Mississippian carbonate, V_p has an average of 5000m/s and V_s of 3000m/s. In this test, it is assumed that at the initial stage, there is only brine in the reservoir, and no CO_2 . Thus the initial fluid saturated bulk modulus K_{sat} and dry frame bulk modulus K_{dry} are calculated and kept fixed. With more CO_2 injected, V_p starts with a rapid decrease around 15% percent after 10% CO_2 injected, then will have a slightly increase after more CO_2 is injected. The bulk modulus of fluid saturated rock will be affected more than the density. Table 6.1 gives a set of model parameters (V_p , V_s , and fluid saturated rock density) calculated from the Gassmann fluid substitution with different CO_2 saturation.

Table 6.1. Calculated model parameters for different CO_2 saturation

CO_2 saturation	Vp (m/s)	Vs (m/s)	fluid saturated density (g/cm^3)
0	5000	3000	2.458
0.1	4878	3005	2.45
0.3	4856	3014	2.434
0.5	4862	3025	2.418
0.8	4880	3040	2.394

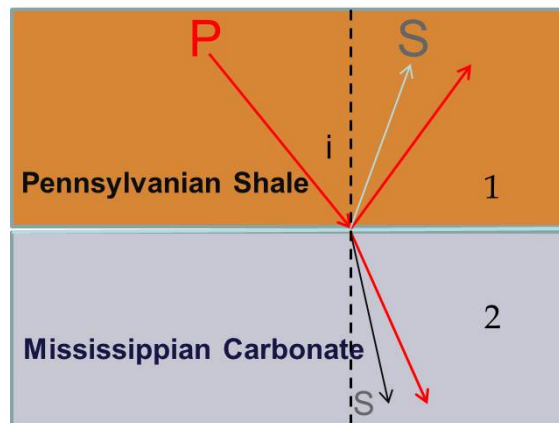


Figure 6.1. A simple two-interface model with overlying Pennsylvanian shale and underlying Mississippian carbonate.

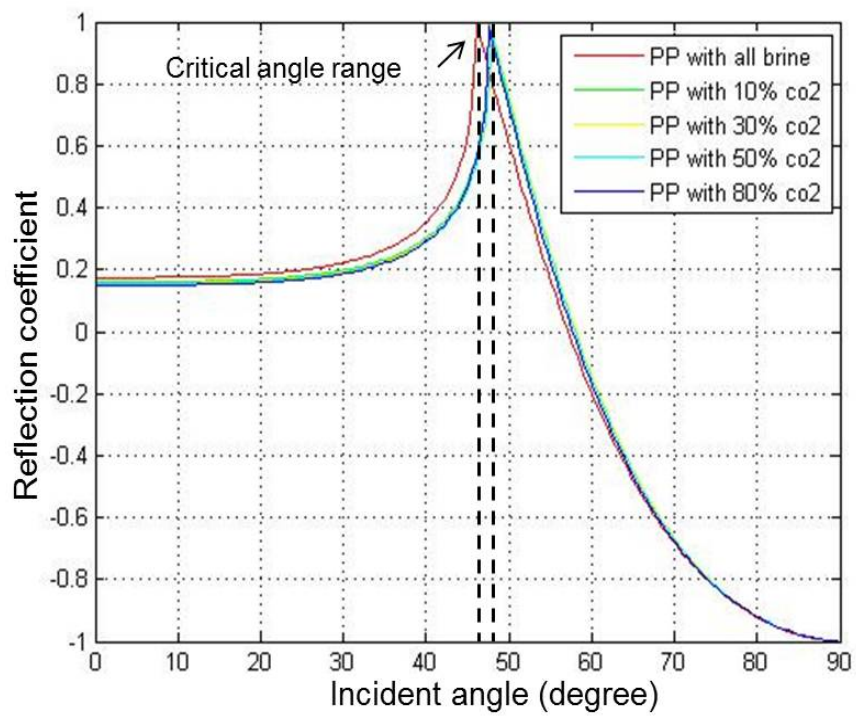


Figure 6.2. PP reflectivity for incident angles from 0-90 degree with brine and 10%-80% CO_2 .

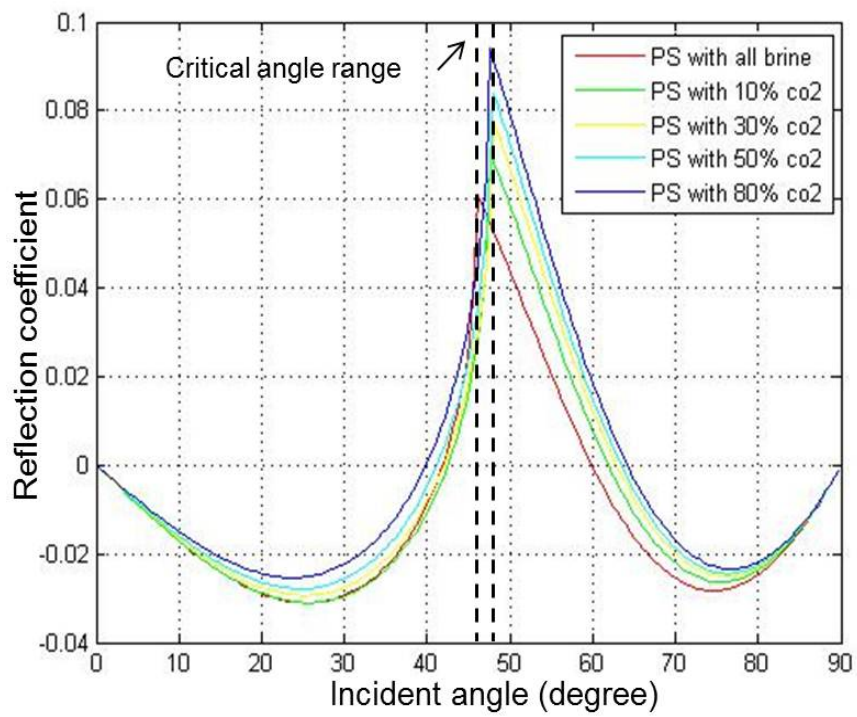


Figure 6.3. PS reflectivity for incident angles from 0-90 degree with brine and 10%-80% CO_2 .

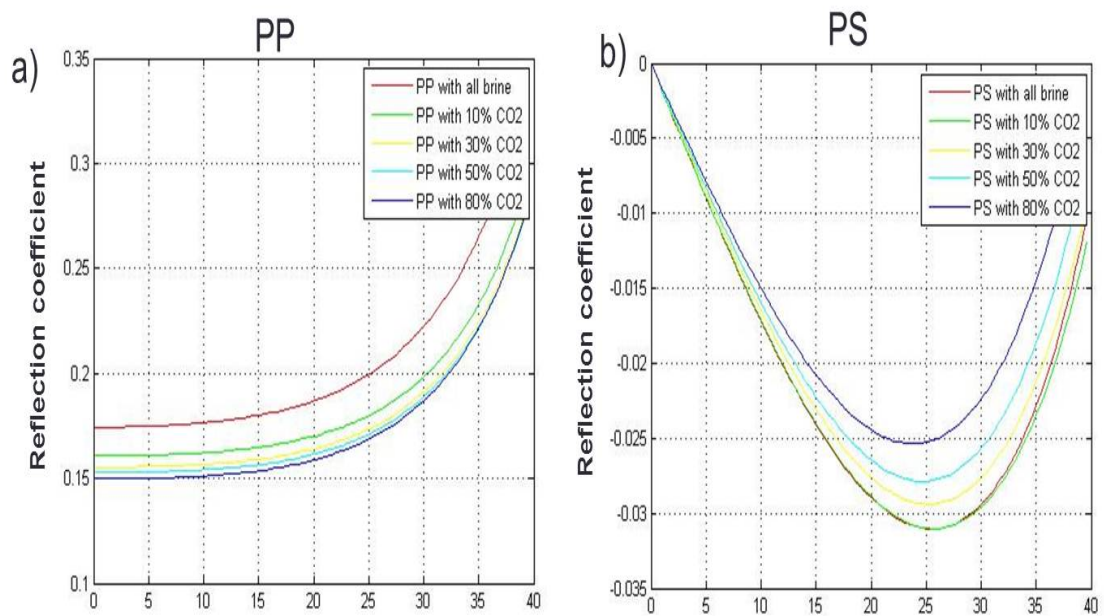


Figure 6.4. Details of PP and PS reflectivity for incident angles from 0-40 degree with brine and 10%-80% CO_2 .

Table 6.2. PP reflectivity

CO_2 saturation	PP reflectivity vs. PP without CO_2 injection (%)
0.1	-7.79 to -14.2
0.3	-10.89 to -17.4
0.5	-12.39 to -17.9
0.8	-14.15 to -17.49

Table 6.3. PS reflectivity

CO_2 saturation	PS reflectivity vs. PS without CO_2 injection (%)
0.1	-0.48 to 17.42
0.3	-8.05 to -3.95
0.5	-40.03 to -6.84
0.8	-50.07 to -12.06

It is evident that at the zero offset (incident angle is equal to 0), there is no reflectivity of PS. Here only incident angles less than critical angle (around 40 degree) are considered (Figure 6.4). With more CO_2 injection, changes on PP reflection coefficients are considerably larger than that of PS; and PP reflectivity increases with more CO_2 injected while PS reflectivity decreases first then increases. The P wave velocity decreases most when CO_2 started to be injected into carbonate reservoir, and with more CO_2 injection, the changes on P wave velocity have a slight increase. S wave does not change much as compared with P wave, because the shear modulus is not affected by the fluid substitution, and density changes are comparably very small. By choosing the incident angle less than 40 degree, a quantitative comparison of PP and PS reflectivity for different CO_2 saturation are listed in Table 6.3 and Table 6.4. Overall, PP reflectivity with more CO_2 saturation decreases, but increases with incident angle. PS reflectivity decreases first and then increases with incident angle. Change of PS reflectivity with induced CO_2 is larger than that of PP, which shows the added value for multicomponent study in CCS.

6.2 Forward modeling results

The Dickman CMG flow simulation output is a set of reservoir property grids that have missing sections interpolated to make a regular 3D volume with dimension of $(n_x, n_y, n_z) = (33, 31, 32)$. The simulation grid upper surface is at around +45m subsea depth (seismic datum is at 792m). The grid cells have uniform lateral dimension $(dx, dy) = (152m, 152m)$ and have an origin at the southwest corner at absolute coordinates (47 617, 21 032) meter coincident with the Dickman field 3D seismic data origin. The simulation grid depth increment (dz) is variable to represent the thickness of geological layering and loss of section due to an unconformity at about -605m subsea. As discussed in the previous sections, the cell size is coarse and needs to be interpolated. For **1D** convolutional forward modeling, to match the existing seismic survey, the flow grid is interpolated into the seismic bin size of 25m by 25m in both x and y directions by using the cubic spline routine in Matlab. The simulated seismic dataset consists of 194 (inline) x 182 (crossline) traces with 1s time window ($dt = 2ms$). In our simulations, monitoring starts with CO_2 injection lasting 50 years, then CO_2 injection stops and flow modeling continues for another 200 years. Seismic volumes have been calculated for simulation years 0 and 250. The flow simulation model has a measured depth ranging from 838m to 1510m. A leakage scenario flow model is shown in Figure 6.5. The leak is set at the seal layers in the flow simulation model by assigning a fault along the northeast direction. It is not a real geological fault, and it is realized by assigning high permeability to the cells at the seal layers as high conductive conduit. The purpose is to test how CO_2 leaks from the storage site if there is fault cutting through the seal. The CO_2 plume in the flow simulation model shown in Figure 6.5(b) has vertical expansion to the top of the seal and expands in the horizontal direction. To validate whether geological structure is accurately represented in the velocity model, one 2D line is plotted in Figure 6.6. This

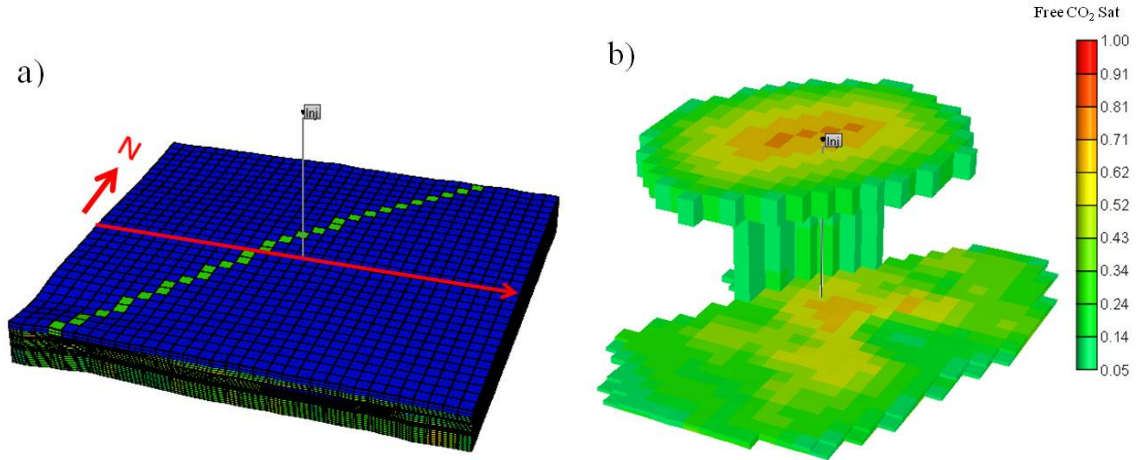


Figure 6.5. (a) Flow simulation grid showing fault (green) and location of seismic inline 100 (red). (b) Accumulation of CO_2 at the Fort Scott level after 50 years of injection and 200 years continued simulation (Liner *et al.*, 2011).

2D line is close to the injection well location and thus has the highest CO_2 saturation. The details of the structure in the red box show the truncation and pinch-out where CO_2 pools at the porous carbonate Mississippian-Pennsylvanian unconformity.

6.3 Reservoir properties

The reservoir properties for inline 100 are shown below. These properties have been regridded with $dz=2m$ and $(dx,dy)=(25m,25m)$. Notice that the depth structure has been top filled and the variation can be detected from this 2D plot; porosity distribution is interpolated and calibrated from digital well logs and core analysis. They may be fuzzy in some areas due to insufficient porosity log information (Figure 6.7). Below is the comparison of a set of reservoir properties at year 0 and year 250.

1. **Saturation:** saturation is changed with CO_2 injected and CO_2 plume is clearly identified in Figure 6.8(b) at the year 250.

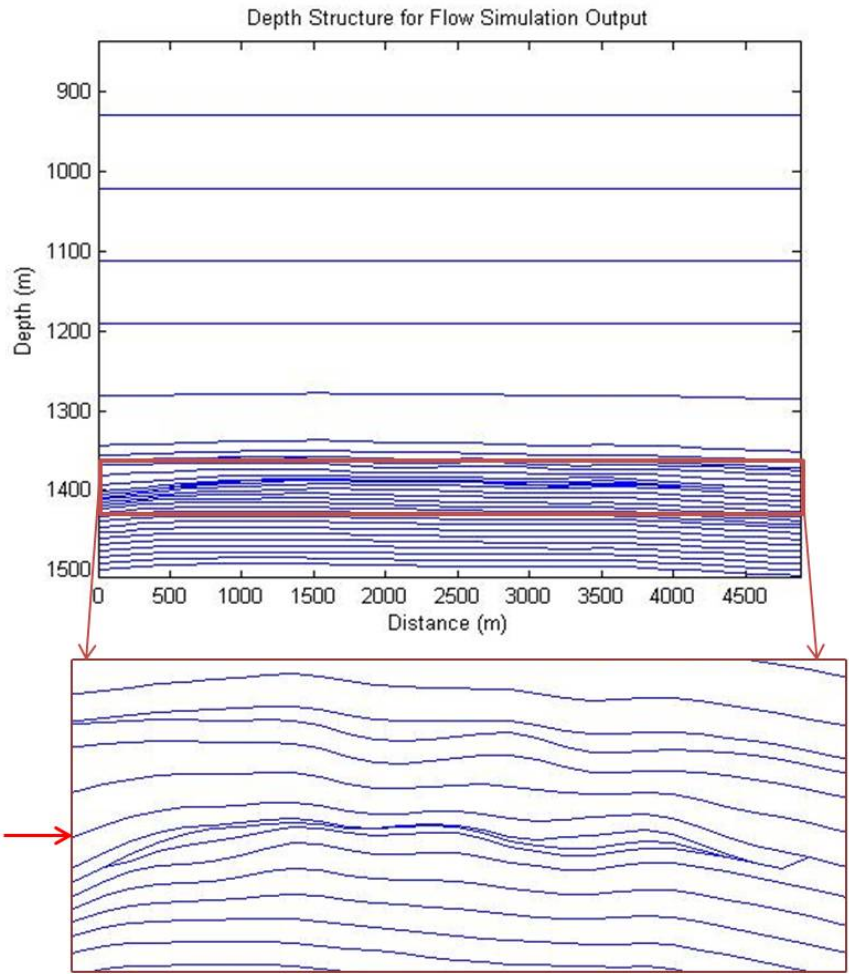


Figure 6.6. Structure of simulation layers along inline 100 in the cross section view. The layers are plotted using the depth points directly from the flow simulator which shows a complex and realistic geological structure. Mississippian unconformity and porous carbonate are identified by red arrow.

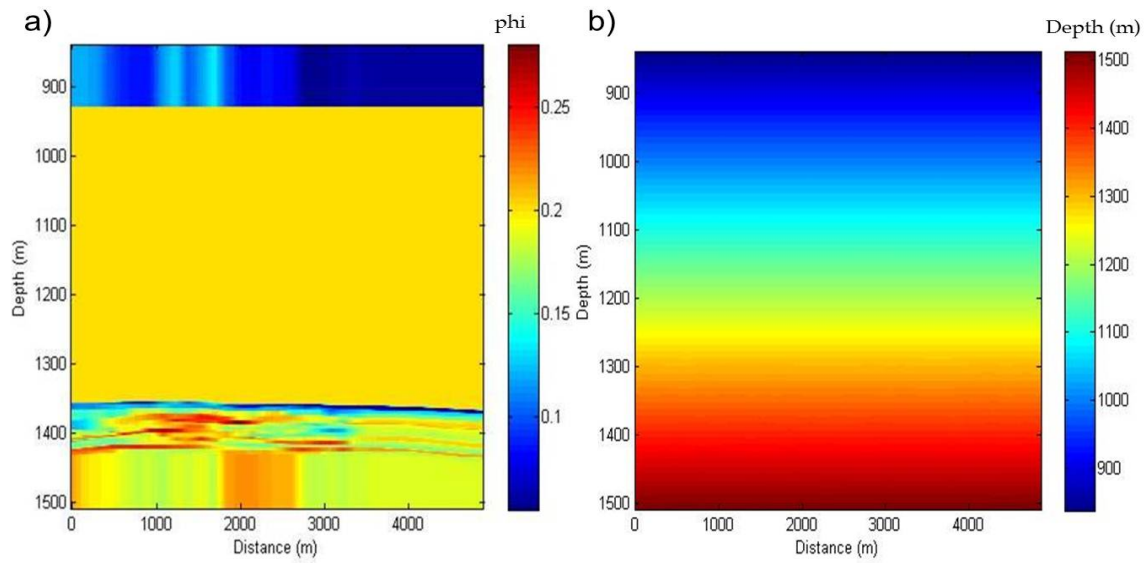


Figure 6.7. (a) Porosity distribution for Inline 100. It's assumed that porosity doesn't change during this injection process. (b) Depth profile for Inline 100. The injection depth is around 1450m.

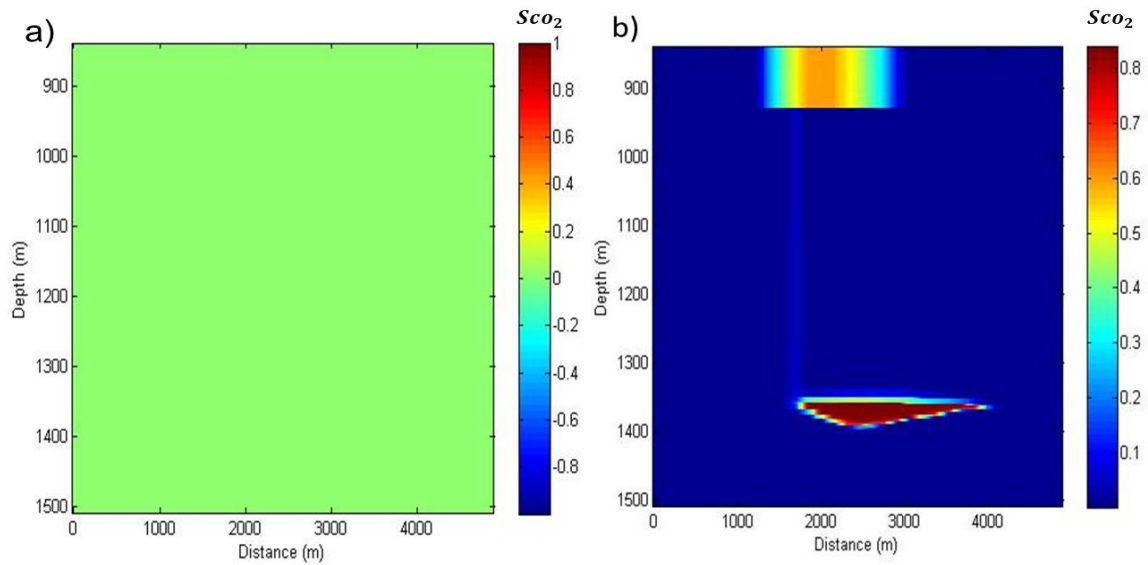


Figure 6.8. Saturation for (a) year 0 and (b) year 250. The CO_2 leakage path can be detected from the top of seal and contained at the surface level.

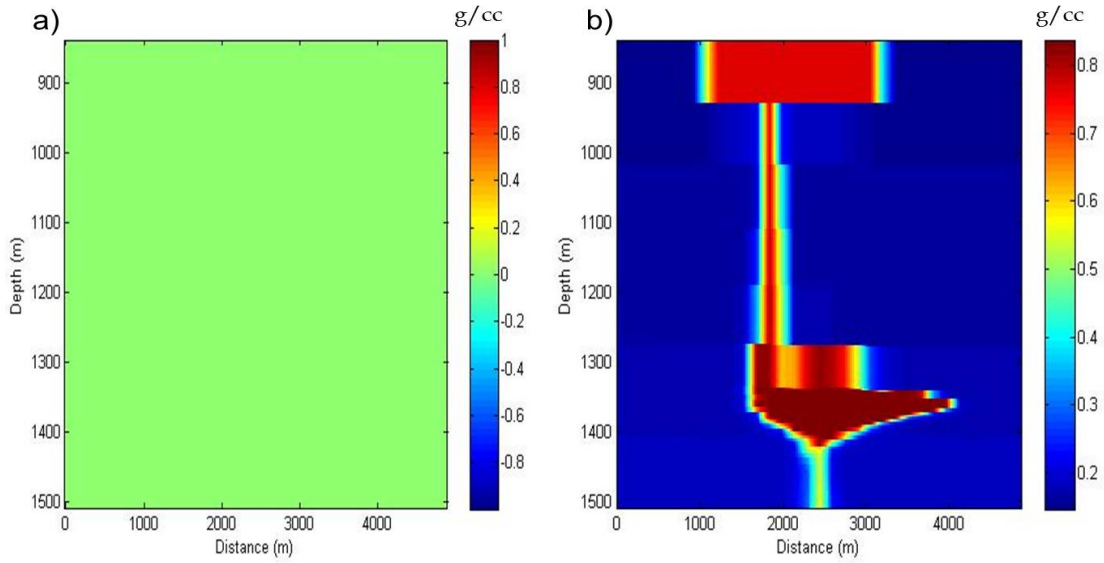


Figure 6.9. CO_2 density for (a) year 0; and (b) year 250. CO_2 density is also changed due to this effect and it increased considerably at the locations where CO_2 accumulates.

2. **Density:** according to CO_2 saturation change, density is also affected due to CO_2 concentration at the high saturation zone (Figure 6.9).
3. **Pressure:** pressure has been also increased due to injection. By comparing the values of pressure changes, it has been almost doubled after 250 years injection (Figure 6.10).

The averaged mineral density and bulk modulus are from dolomite and calcite. For the seal layers, the mineral content is composed of hard limestone and clay (Figure 6.11).

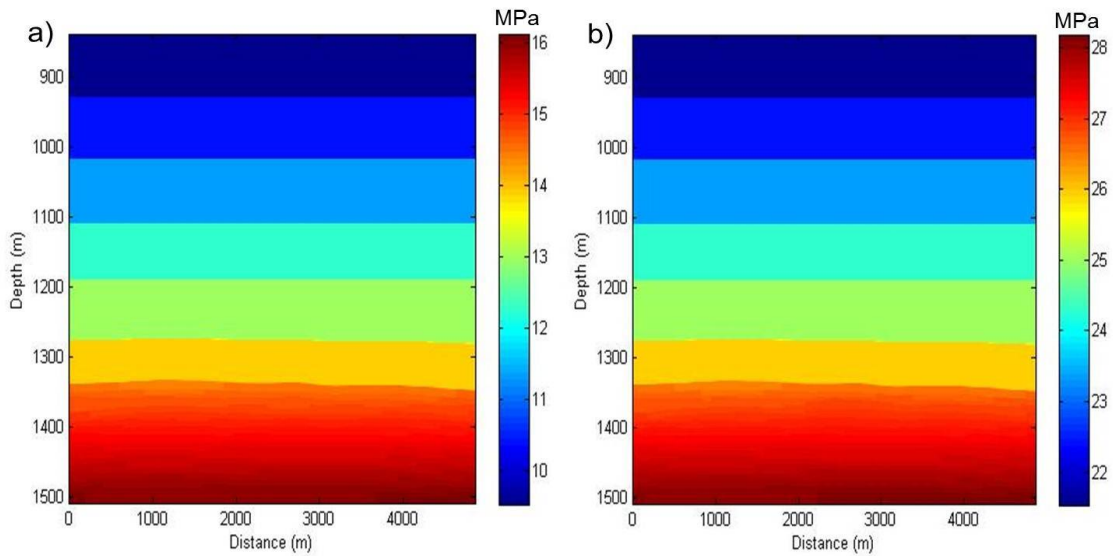


Figure 6.10. Pressure for (a) year 0; and (b) year 250. Pressure has approximately doubled throughout the model due to CO_2 injection at depth around 1450m and is proportional to depth.

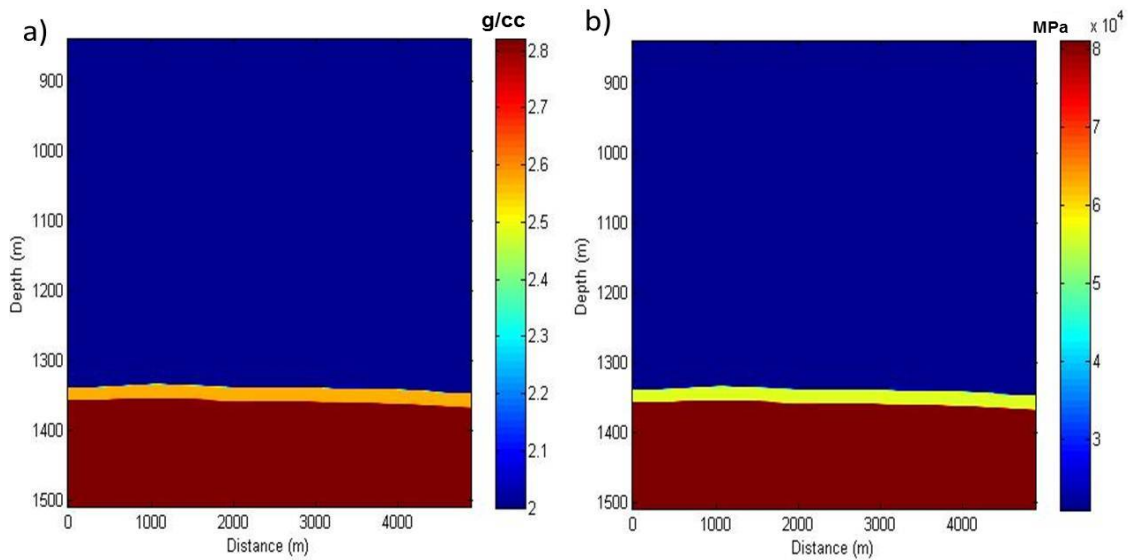


Figure 6.11. (a) Averaged rock density; (b) Mineral bulk modulus

6.4 Example 1: One dimensional convolutional forward modeling results

The initial velocity estimates used the well log Humphery 4-18. Since there is no shear log in the Dickman field, a constant V_p/V_s value of 1.62 is applied. This result is obtained from different localized geological V_p/V_s ratio from statistical core analysis by Schlumberger and Core Lab. Our study shows that the crossplot of V_p and V_s has come up with the closest ratio 1.62 (Wu and Liner, 2011). Although this well is located inside the seismic survey outline, it is not deep enough to accommodate changes in the deeper section of flow simulation model. The well Side Bottom 6 was brought in to compensate the deeper variations, but it is located outside of the seismic survey and may not provide accurate geological information to represent its surrounding deposition. This single well velocities were populated to three dimensions. For seismic simulation using 1D convolutional forward modeling, this velocity can be adequate.

As mentioned earlier, the velocity model has (n_x, n_z) of (194,336) data points. The vertical grid spacing dz is set as 2m and both dx and dy are set as 25m. The 1D convolutional forward modeling requires a vertical cell size small enough to represent realistic vertical impedance variations in the earth. The native vertical spacing from the flow simulation model varies from 0.2m to 90m which is regridded to a constant dz of 2m. The one dimensional forward modeling focuses on the vertical change, 25m spacing for (x,y) is adequate. The velocity models are calculated for flow simulation years 0 and 250 (Figure 6.12). The velocity structure for year 250 clearly shows reduced velocity features related to the CO_2 saturation change shown in Figure 6.12(c).

A Ricker wavelet with dominant frequency 35Hz is used, based on seismic data spectrum analysis of the Dickman 3D survey (Figure 6.13)(Liner, 2012). Changes in shallow CO_2 saturation cause velocity difference cause time shifts in seismic modeling results. Therefore,

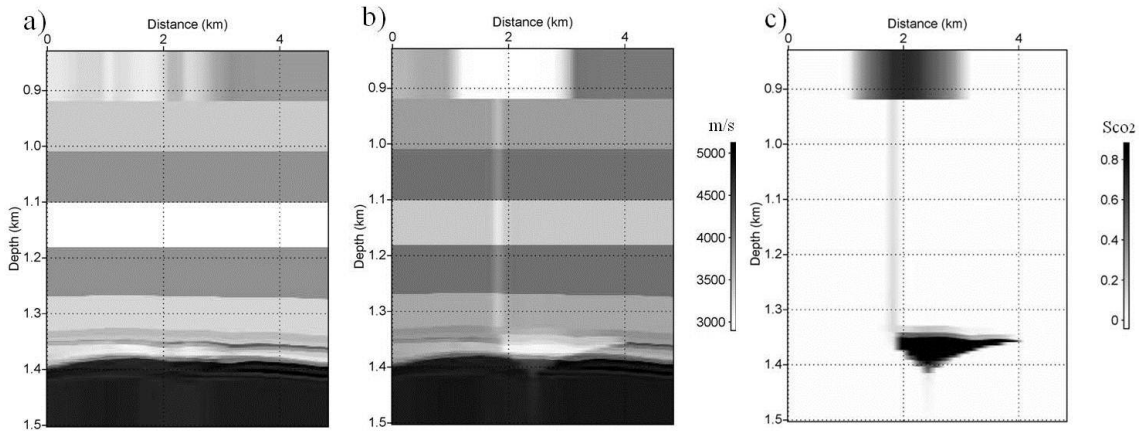


Figure 6.12. (a) P-wave velocity field in simulation year 0. (b) P-wave velocity field in simulation year 250, after 50 years of CO_2 injection and 200 years of continued flow simulation. Note vertical faults acts as CO_2 conduit. (c) Saturation levels of CO_2 in year 250.

the seismic images shown here are all depth converted (Figure 6.14) using their exact corresponding velocity models. Figure 6.15 shows a detailed depth interval at around 1350m to 1500m at the sequestration site. It is evident that seismic results with 35Hz dominant frequency at an average velocity of 5000m/s can not resolve the subtle feature within the 2m depth interval. But for acoustic or elastic forward modeling methods, the 2m interval may be necessary to help detect the detailed reservoir property changes. Figure 6.16 gives the comparison of depth converted seismic images from the velocity models shown in Figure 6.12. Notice that changes on seismic are closely related to the change of CO_2 saturation. Difference on seismic images caused by CO_2 saturation is validated in Figure 6.16. Figure 6.17 gives the map view of the property changes (porosity and CO_2 saturation and velocity changes at the depth of Mississippian unconformity shown in as the red arrow in Figure 6.14. Figure 6.18 shows the CO_2 density at the year 250 due to the saturation change. The velocity without CO_2 injection is highly correlated to porosity distribution shown as in Figure 6.17(a). But with more CO_2 injection into the sequestration cite, velocity is more

affected by CO_2 saturation. Figure 6.19 shows the seismic changes for these two years and the difference is mostly affected by the combination of porosity and saturation, and amplitude has decreased about 50% after CO_2 injection.

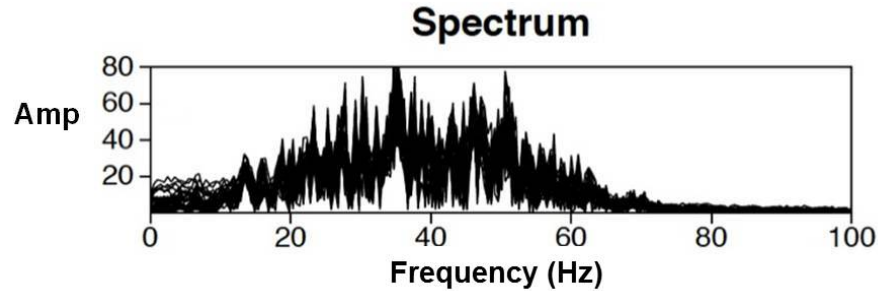


Figure 6.13. Frequency spectrum for the Dickman field (Liner, 2012). The dominant frequency is around 35Hz.

This study only showed the results of the first and the last year of CO_2 injection. The leakage test of 250 years CO_2 monitoring is able to reveal CO_2 flow paths from the saturation change obtained from the flow simulation output at each time step. Figures 6.20-6.23 show the map view of CO_2 saturation for four different years (2,20,30,32). Layers 1 to 8 are the additional layers added on top of the flow model for CO_2 containment as mentioned earlier. The CO_2 saturation at each layer at these four different years illustrate how CO_2 migrates from the sequestration cite. Figure 6.20 (year 2) shows that at the initial stage of injection, a small amount of CO_2 started to migrate into layer 8; Figure 6.21 (year 20) shows that CO_2 has migrated into layer 3 and started to accumulates at the layer 8. Figure 6.22 (year 30) shows that CO_2 has reached layer 2 and Figure 6.23 (year 32) shows that CO_2 has leaked to the surface. The whole process takes 32 years.

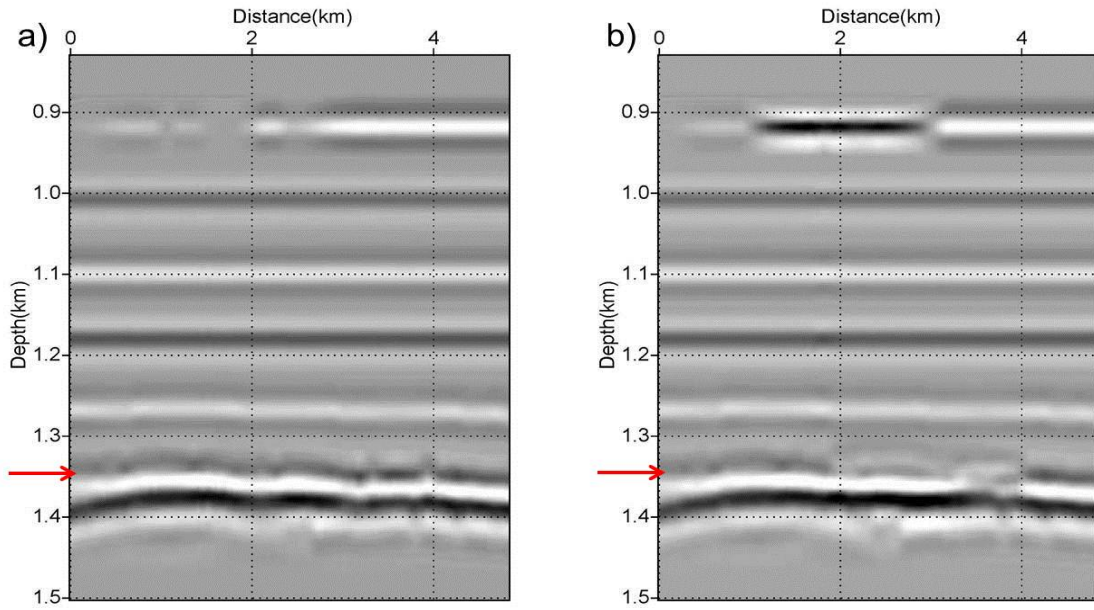


Figure 6.14. One-dimensional seismic convolutional forward modeling results for inline 100: (a) first year of injection ; (b) last year of monitoring (250) (red arrow shows top of sequestration cite at around 1348m measured depth).

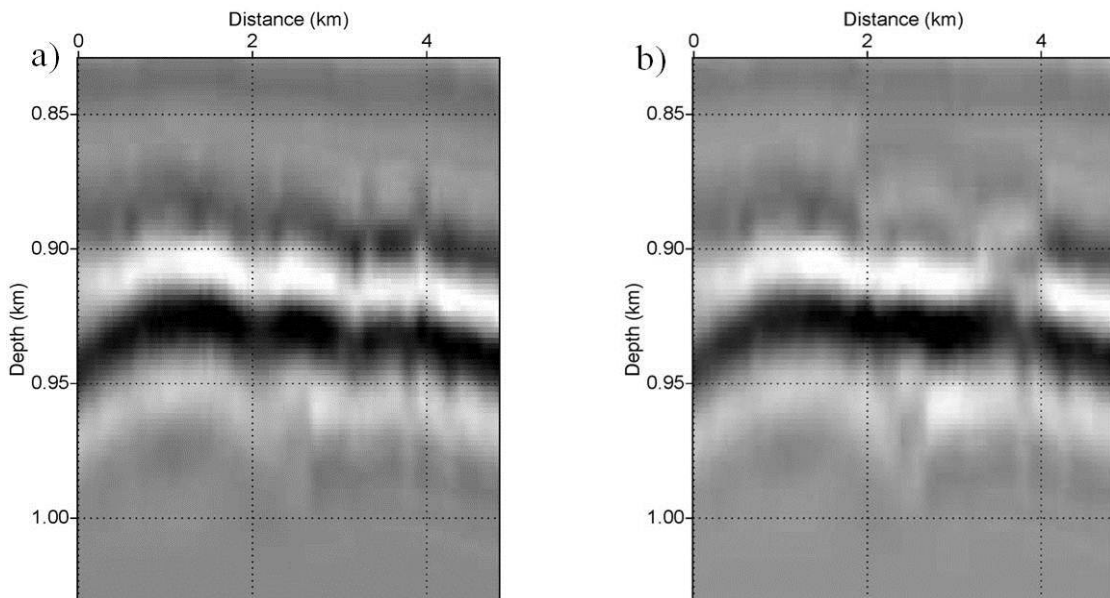


Figure 6.15. Details of seismic simulation in Figure 6.14: (a) year 0, (b) year 250.

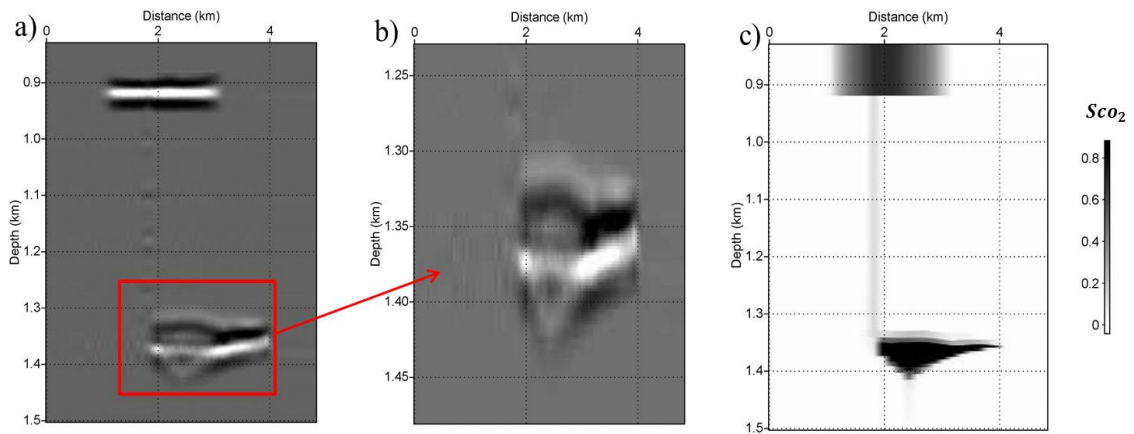


Figure 6.16. (a) Difference on seismic sections between year 0 and 250 due to CO_2 injection. (b) Detailed 1D convolutional seismic simulation result at the sequestration level. (c) CO_2 saturation at the last year of monitoring (year 250).

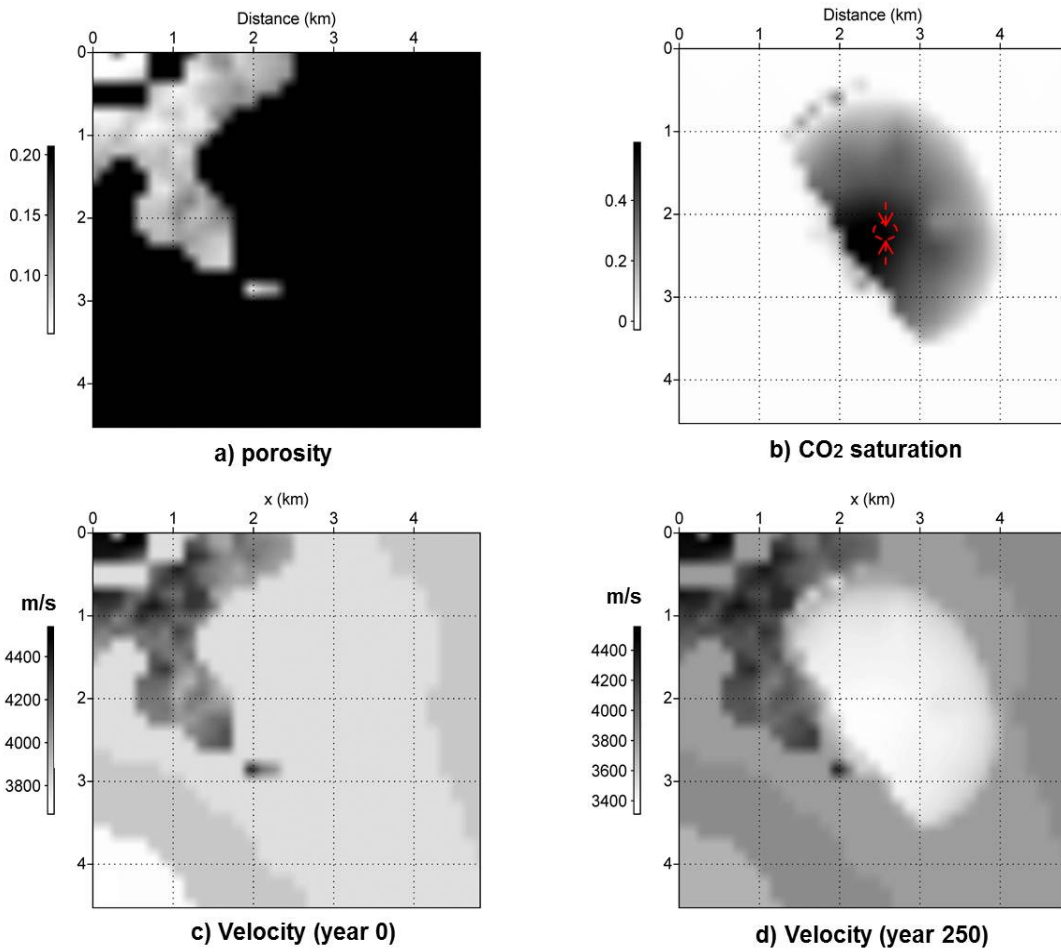


Figure 6.17. Map view of CO_2 properties and velocity models at the sequestration site (top of Mississippian: depth 1348m) for year 0 and year 250. (a) porosity, (b) CO_2 saturation, (c) velocity in year 0, (d) velocity in year 250. Injection well is marked with red color.

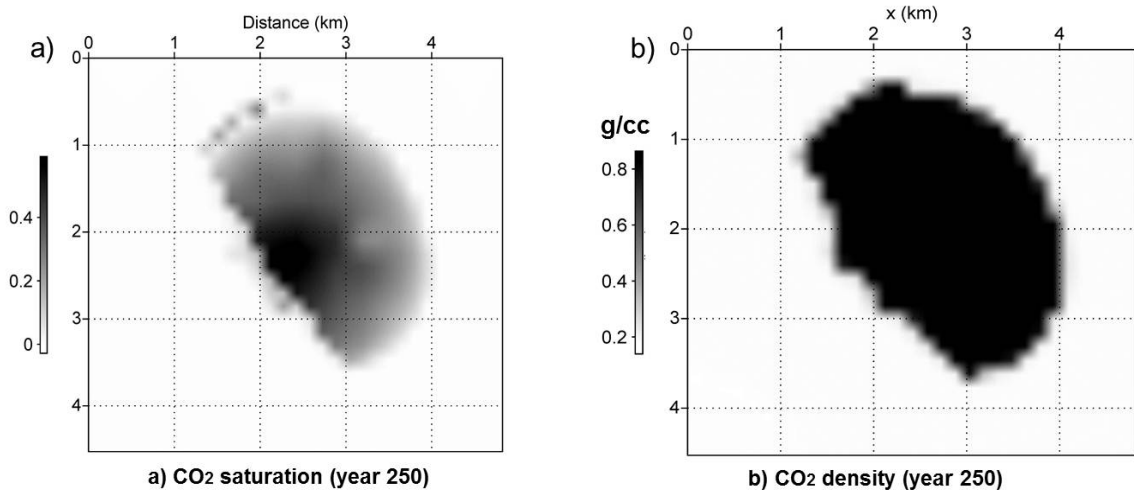


Figure 6.18. Map view of CO_2 density at the sequestration site at year 250.

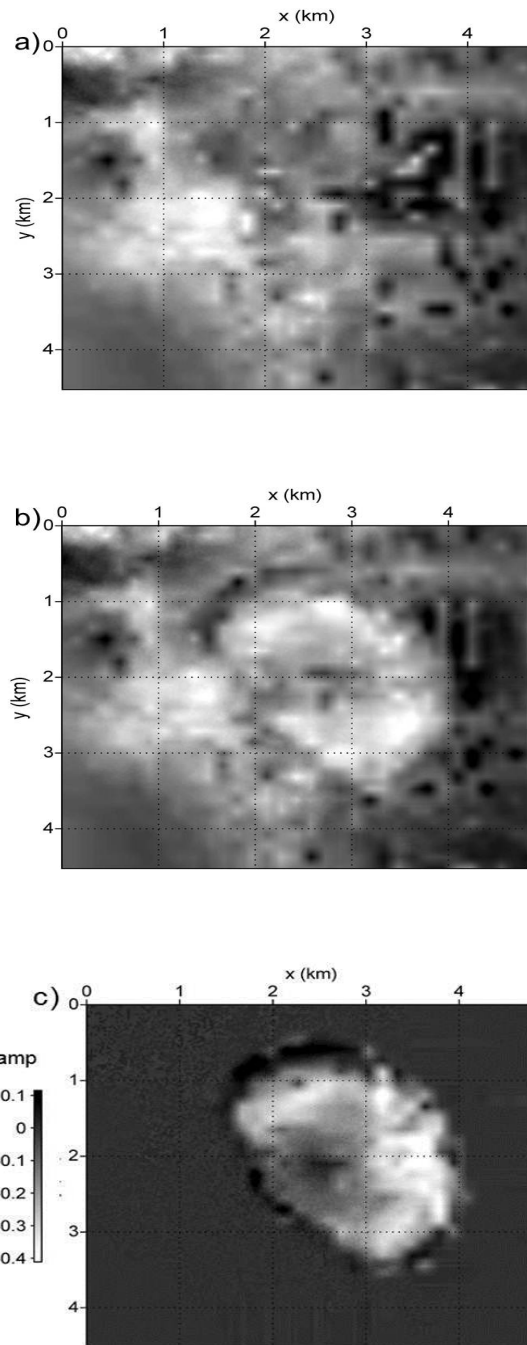


Figure 6.19. Depth slice (1348m) of 1D convolutional forward modeling results (a) Year 0. (b) Year 250. (c) Difference.

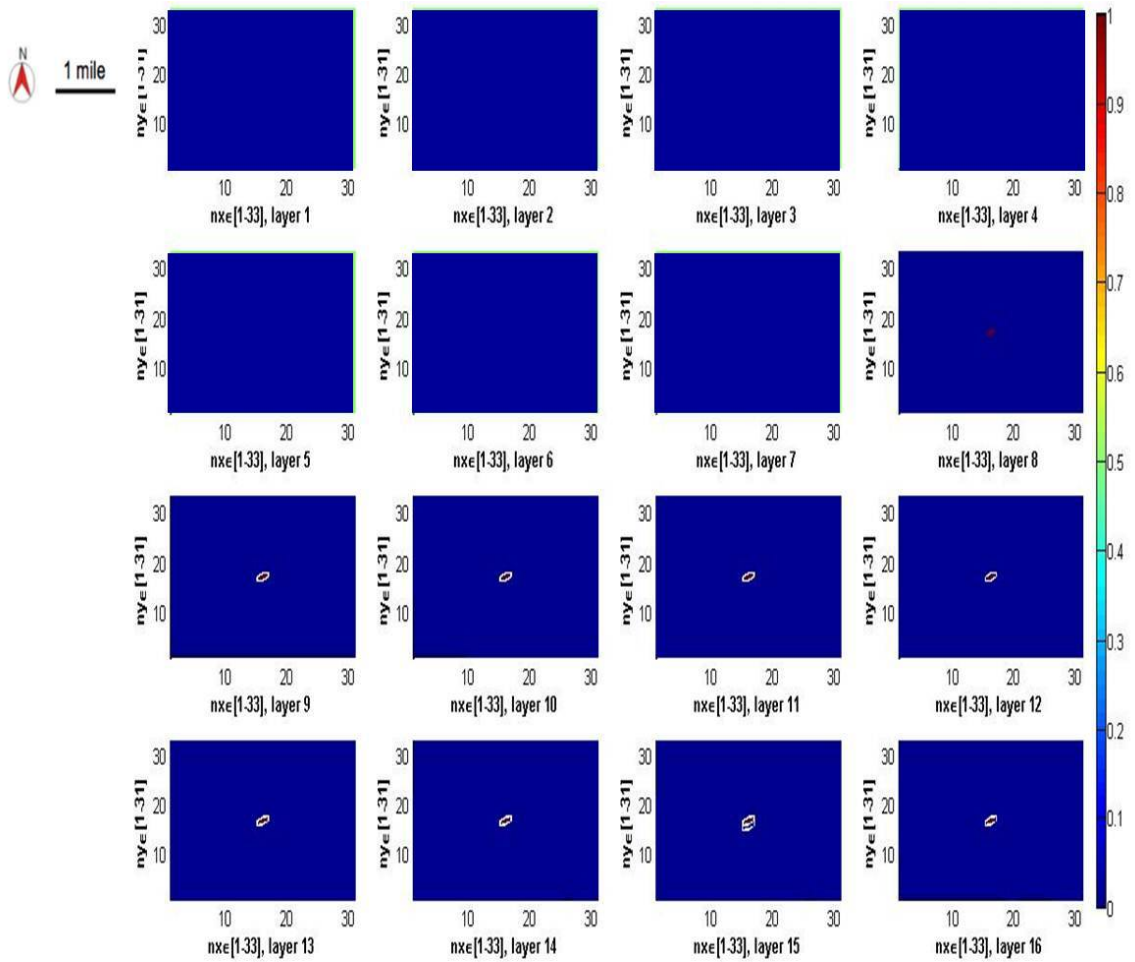


Figure 6.20. Map view of CO_2 saturation for simulation layers from 1 to 16 at year 2. CO_2 started to migrate into layer 8, which is one of the layers added on top of storage site for containment.

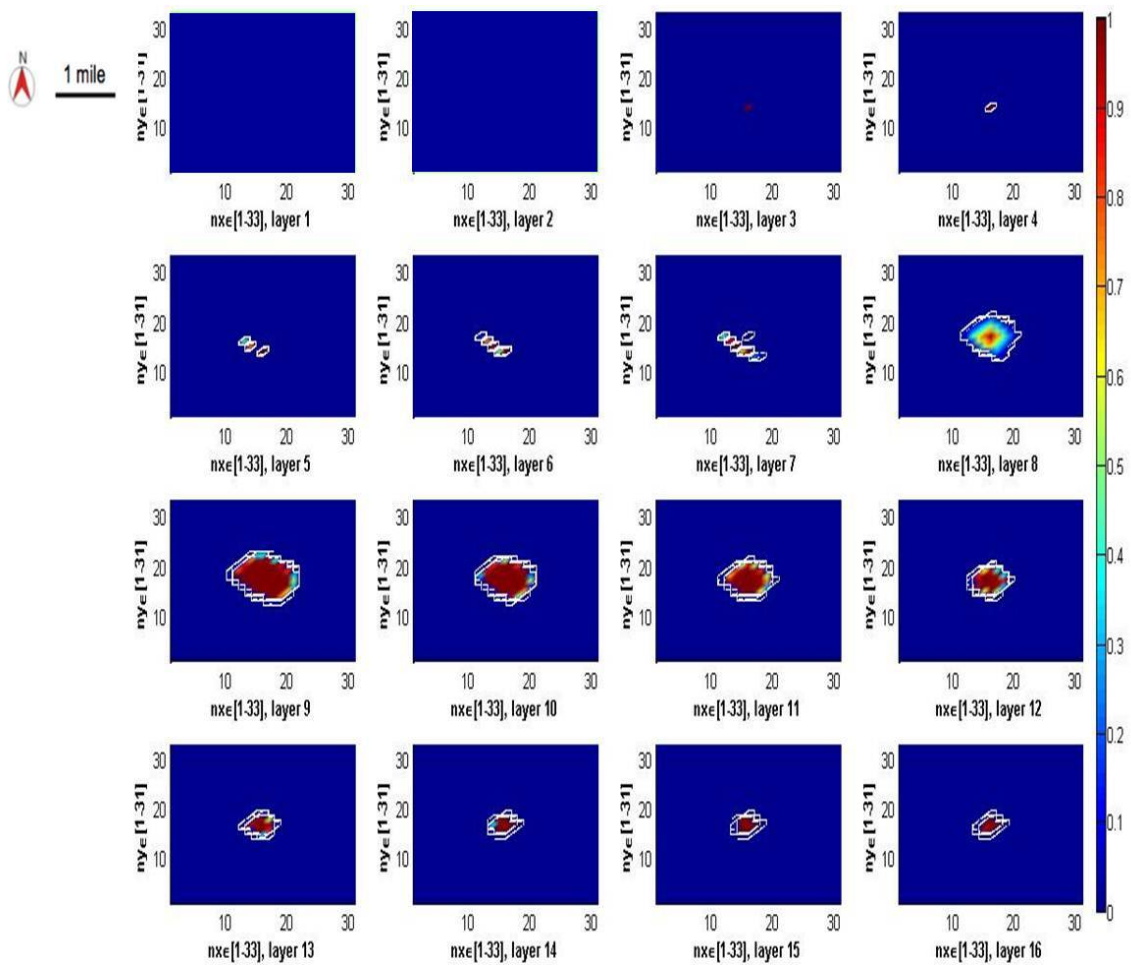


Figure 6.21. Map view of CO_2 saturation for simulation layers from 1 to 16 at year 20. CO_2 migrated into simulation layer 3 and 4.

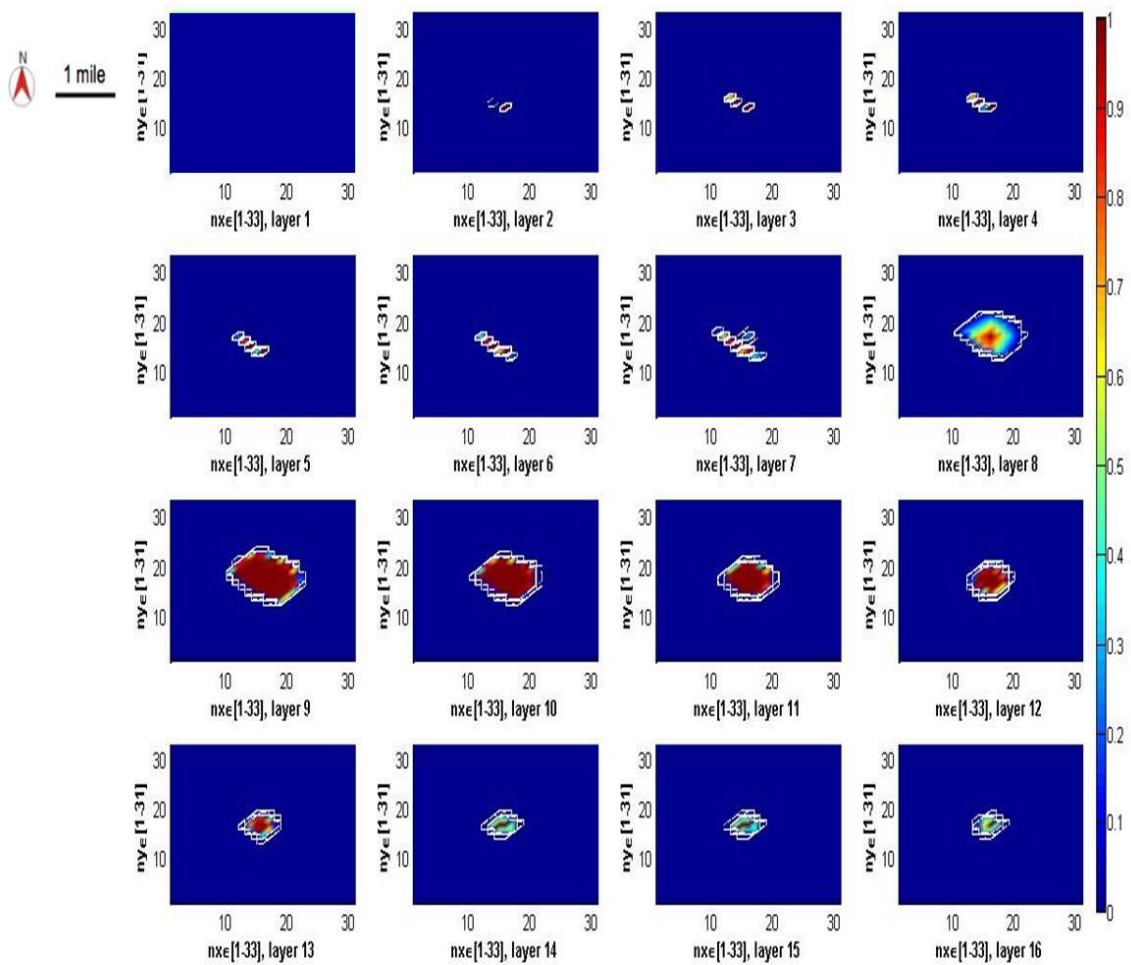


Figure 6.22. Map view of CO_2 saturation for simulation layers from 1 to 16 at year 30. CO_2 migrated into layer 2, and started to accumulate from the sequestration site.

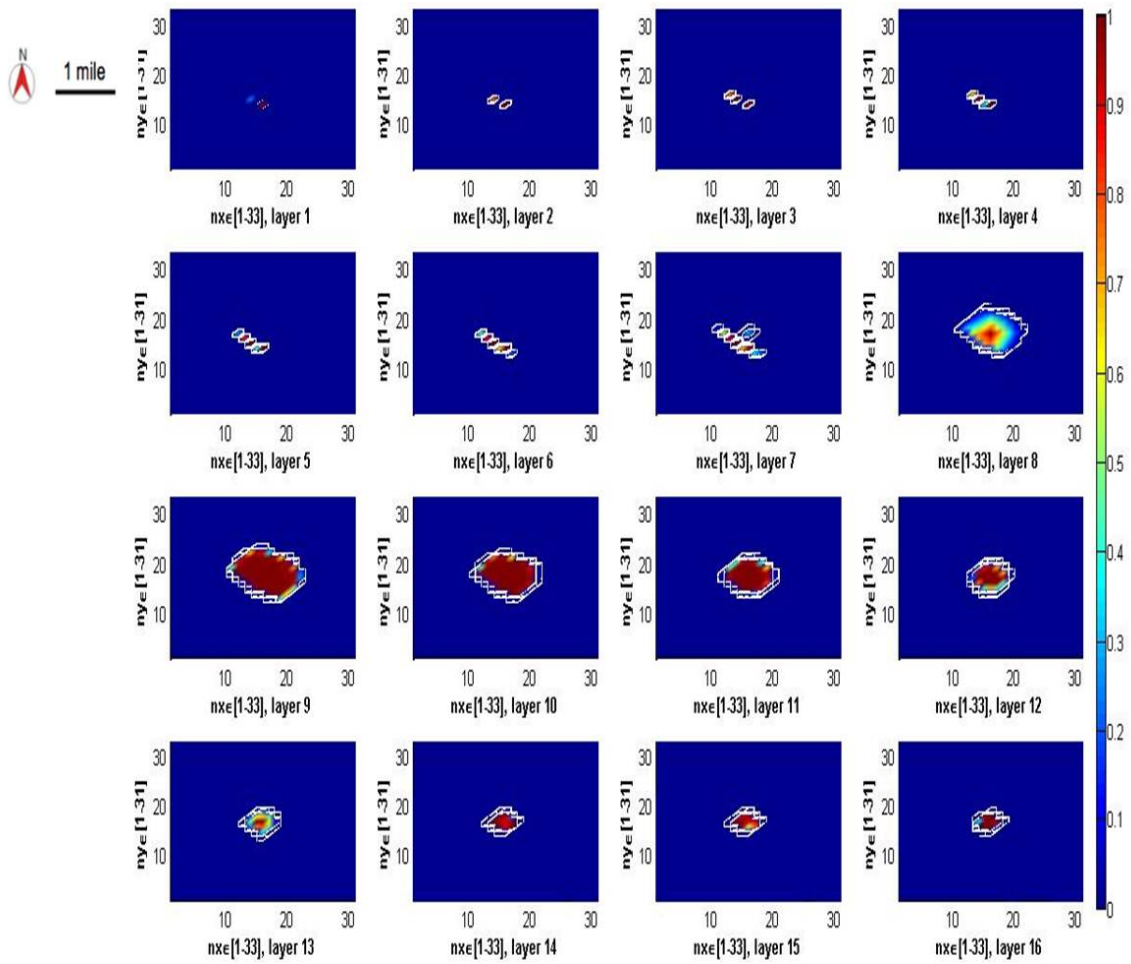


Figure 6.23. Map view of CO_2 saturation for simulation layers from 1 to 16 at year 32. CO_2 started to leak at the surface.

6.4.1 Validation of gridding technique

As previously discussed, when doing the regridding from flow simulation to seismic, the variation of cell size in z direction is quite large from less than 0.5m to 150m. A reasonable dz of 2m is used to maintain the calculation efficiency and also reduce the numerical dispersion in the forward modeling methods. In order to evaluate the accuracy for this process, the CO_2 saturated rock velocity model (year 0) is converted from depth to time using the SU command **Suztot** to see if the Mississippian Pennsylvanian unconformity still lies in the accurate traveltimes. A time slice ($t=848ms$) at this unconformity is plotted in Figure 6.24 which shows the channel feature. In the cross section view, this unconformity is detected at around 848ms corresponding to the original seismic data. This has proved that the gridding process maintains the accurate traveltimes and is valid and reliable.

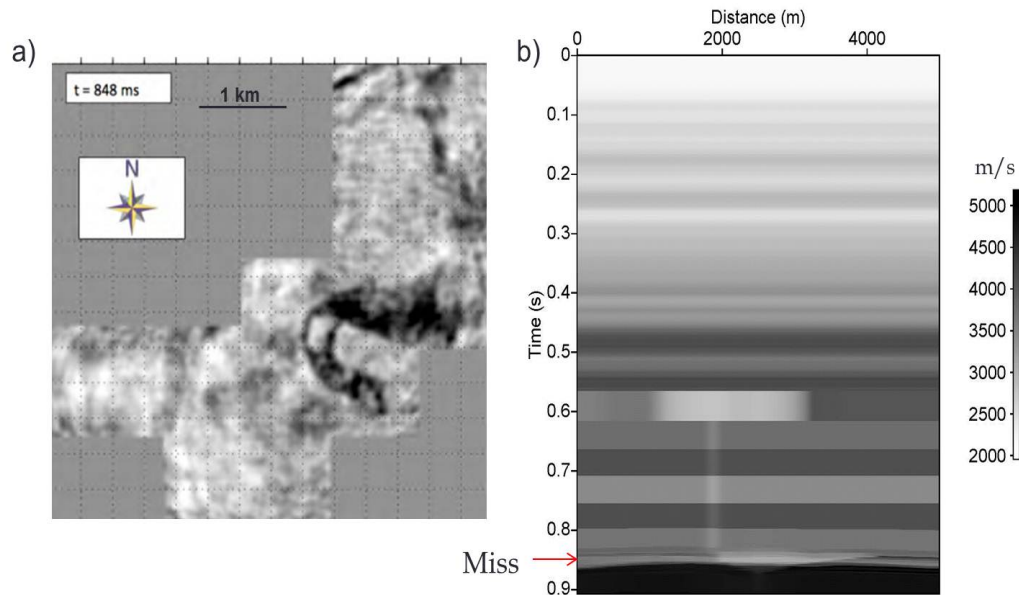


Figure 6.24. Validation of the gridding technique using 2m cell size in (x,y) and z. (a) Time slice at the Mississippian - Pennsylvanian unconformity at the time (848ms) (Liner, 2012) and (b) depth to time converted velocity model (year 0), the red arrow shows the Mississippian - Pennsylvanian unconformity

6.5 Example 2: Two dimensional acoustic and elastic forward modeling results

The velocity model for this simulation method is composed of two parts: the deeper includes rock velocity and density using Gassmann fluid substitution from the top of flow model to the base of deep saline aquifer (830m to around 1520m). The shallower part consists of additional layers added to surface added in order to obtain a realistic earth model instead of simply using the flow model with a nonzero starting depth. Parameters for these top layers are obtained using sonic and neutron density curves from the Humphery 4-18 well. Where log data is missing in the near surface, properties are extrapolated from the adjacent layers with good values to the surface ($z=0$). The S wave velocities are obtained from constant V_p/V_s value of 1.62. Due to rapid large variations at logs scale, these parameters are first averaged from half foot to 2m spacing and smoothed within a 10m depth window. The smoothed shallow model is combined with the deeper V_p , V_s and density model as input for the seismic simulation. In this section, the Seismic Unix command **Sufctanismod**, a flux-corrected transport correction applied to the 2D elastic wave equation for finite difference modeling in anisotropic media has been used. In order to model the acoustic waves, it was realized with V_s set to 0.

Nevertheless, when performing forward modeling methods, the grid size in (x,y) plane needs to be regridded. In order to obtain accurate and reliable forward modeling results, the (x,y) plane grid size is regridded with the same size as dz (2m), and thus this 2D forward modeling is realized on evenly spacing 2D grid with $(dx,dz)=(2m,2m)$. The shot is located at the center of the receiver line. Depth of the receiver line is set at one vertical sample down (2m) below the surface. The offset ranges from -2400m to 2400m which makes the total number of traces 2400. The record length is 2s with time sample rate of 2ms. For elastic forward

modeling, the source direction is vertical and a 35Hz Ricker wavelet is used. The shot gathers parameters for 2D acoustic and elastic forward modeling are shown in Figure 6.25. The shot for VSP geometry is slightly off the center of model around 50m. The receivers

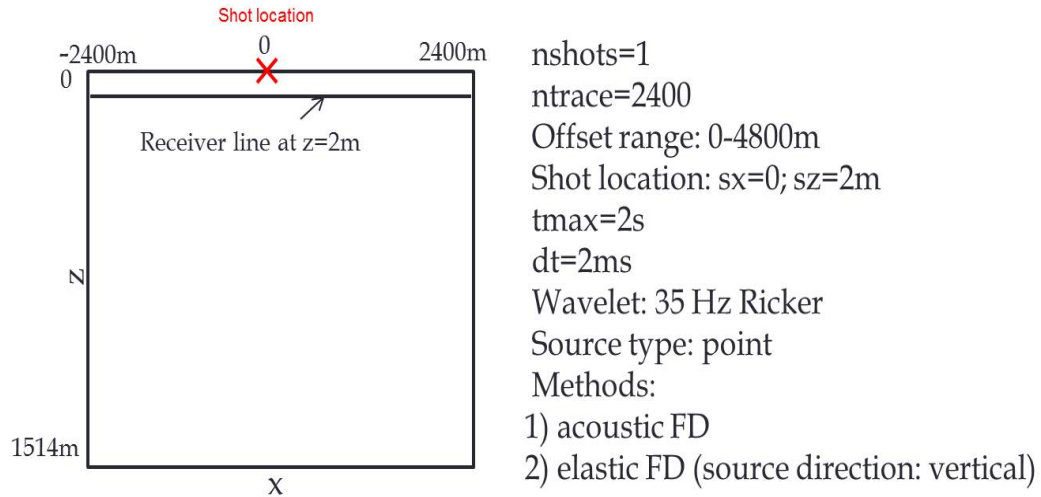


Figure 6.25. Shot gather parameters for 2D acoustic and elastic finite difference modeling.

are lined up at the center of the model with spacing of 2m (Figure 6.26).

6.5.1 Acoustic forward modeling results

The input model for elastic forward modeling includes both P and S wave velocities, as well as density (Figure 6.27 and Figure 6.28). It is assumed that shear velocity is unaltered during Gassmann fluid substitution. The elastic forward modeling results include both horizontal and vertical data components.

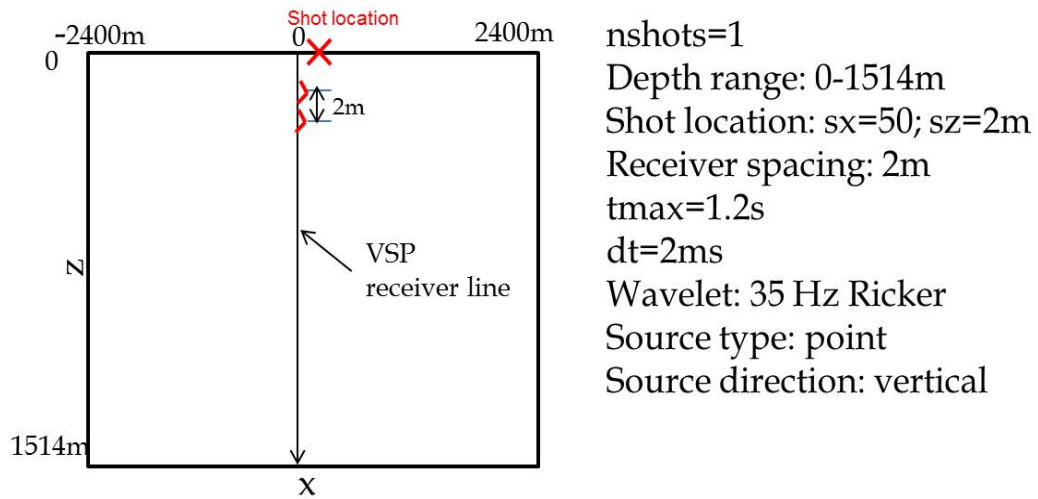


Figure 6.26. VSP geometry affiliated with the results from finite difference modeling code.

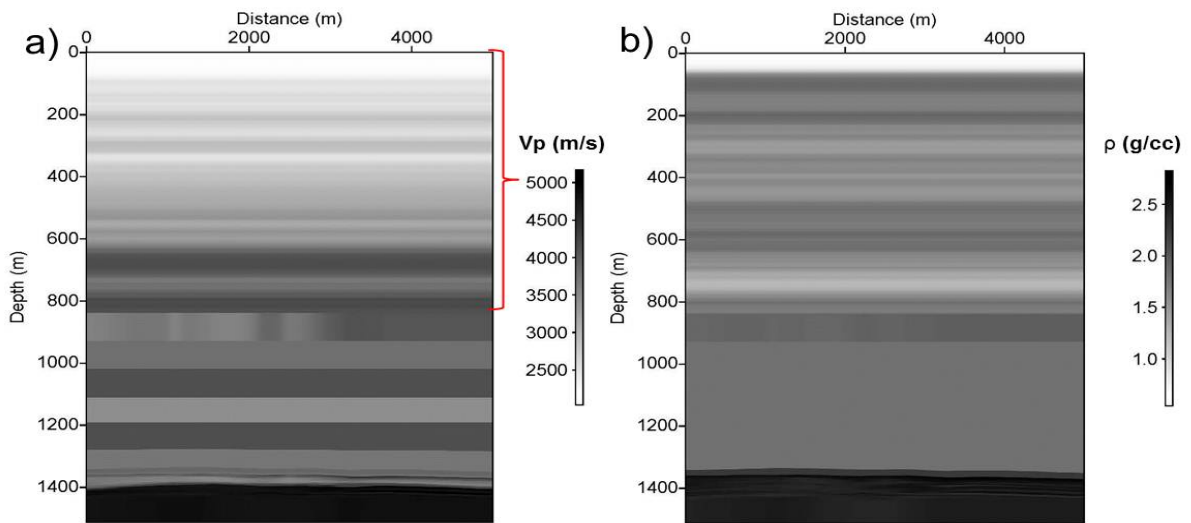


Figure 6.27. Input models for acoustic forward modeling at year 0: (a) V_p . (b) Fluid-saturated density. Red bracket shows the additional layers added on top of flow model from the well Humphrey 4-18, same for V_s and density models.

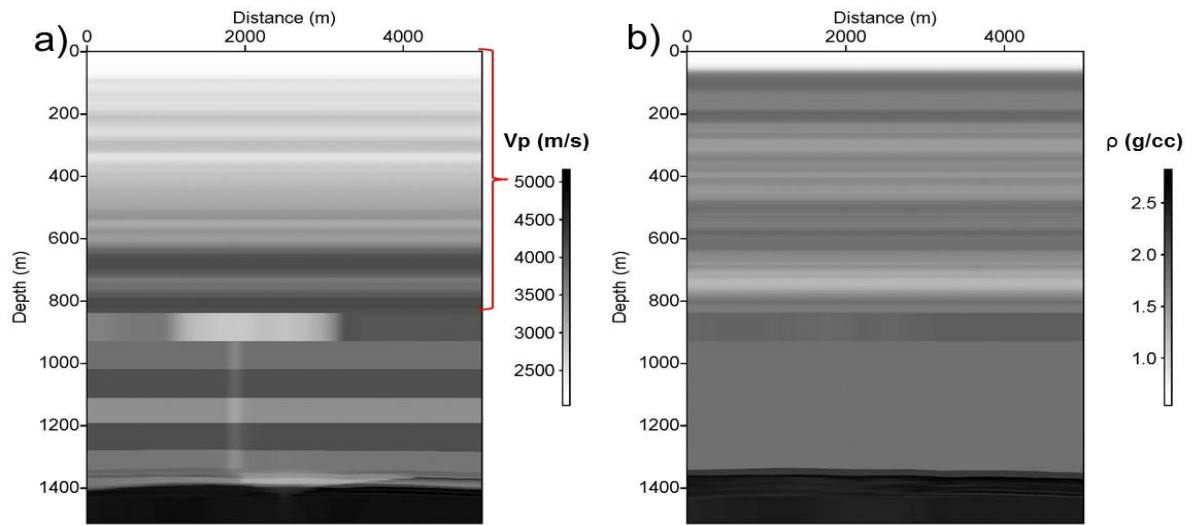


Figure 6.28. Input models for acoustic forward modeling at year 250: (a) V_p . (b) Fluid-saturated density.

The shot gathers from acoustic forward modeling method have low frequency artifacts at near offsets (shown as vertical lines on shot gather), which is likely due to Gaussian source pulse that has finite energy at zero frequency. To remove these stubborn artifacts, the processing steps are as follows:

1. cut the time window down to 1.25s and apply low cut band pass filter to the data
2. pull out the traces with offsets less than 20m and zero them, and give blank traces with correct headers
3. split traces with negative offsets less than -20m
4. split traces with positive offsets greater than 20m
5. reform shot record with blank near offset traces

The shell script is as follows:

```
segyread tape=./shotz250p0.segy \  
| segyclean \  
| suwind tmax=1.25 \  
| sufiler f=5,10,100,110 \  
| suresamp dt=.002 nt=600 \  
| suwind j=5 s=1 \  
> shot.su  
# pull out offsets leq 20 m and zero them  
# giving blank traces with correct headers  
suwind < shot.su key=offset abs=1 max=18 \  
|suzero itmax=600 \  

```

```
> nears.su
# split negative offsets and keep leq -20 m
suwind < shot.su key=offset max=-20 > left.su
# split positive offsets and keep geq 20 m
suwind < shot.su key=offset min=20 > right.su
# reform shot record with blank near offset traces
cat left.su nears.su right.su > shot1.su
rm left.su nears.su right.su shot.su header binary
mv shot1.su shot.su
surange < shot.su
suximage < shot.su perc=99 &
suxwigb < shot.su key=offset perc=99 &
exit 0
```

The shot records before and after processing is shown in Figure 6.29.

All the shot records shown below have been applied this processing procedure. The shot gather using acoustic forward modeling method for year 0 is plotted in Figure 6.30(a). In order to identify the geological layers, vertical seismic profile (VSP) results for the shot gathers are plotted (Figure 6.30(b)). According to the first break for this wave propagation along the borehole, top of flow model (838m), the Mississippian and Pennsylvanian unconformity (around 1350m) and top of deep saline aquifer (1400m) can be identified with the same two-way travel time on the surface seismic modeling results. For year 0, traveltimes for the top of flow model is around 600ms; and Miss-Penn unconformity lies at around 848ms, which is valid based on our previous discussion, and deep saline aquifer corresponds to 900ms. These time values are quite reasonable. For year 250, the results and corresponding

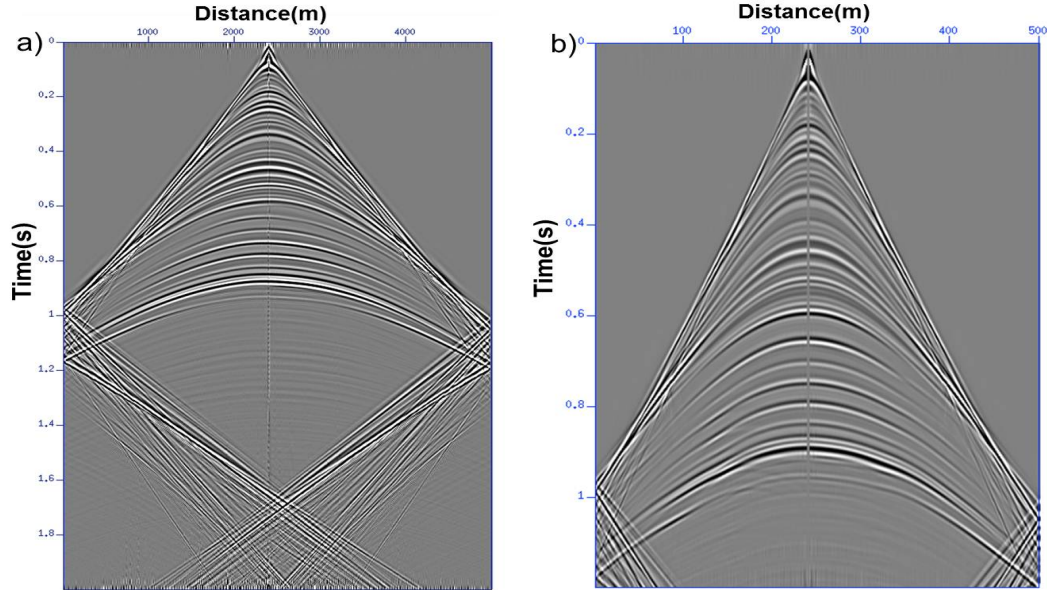


Figure 6.29. Acoustic forward modeling results: (a) Before processing. (b) After processing.

geological layers are identified in a similar fashion (Figure 6.31). For year 250, due to high CO_2 saturation that would decrease the velocity values, traveltimes from the top of model will be larger than year 0 and time shift is detected by comparison for these two years.

A comparison of this shot gather from acoustic forward modeling at different times are plotted in Figure 6.32. Notice that the traveltimes are kept constant from the surface to the top of flow model for year 0 and year 250, but 2 time samples shift (downward) exist from the top of flow model due to CO_2 saturation change with decreased velocity in year 250. The time shift is small, because velocity at the carbonate reservoir is pretty high as around 4500m/s.

In order to compare the seismic response for these two years, subtraction is performed. The result (Figure 6.33) shows that CO_2 leakage has resulted in a velocity change to the top of the flow model, and thus cause the reflections misfit due to different traveltimes. The same feature can be seen from the elastic forward modeling results.

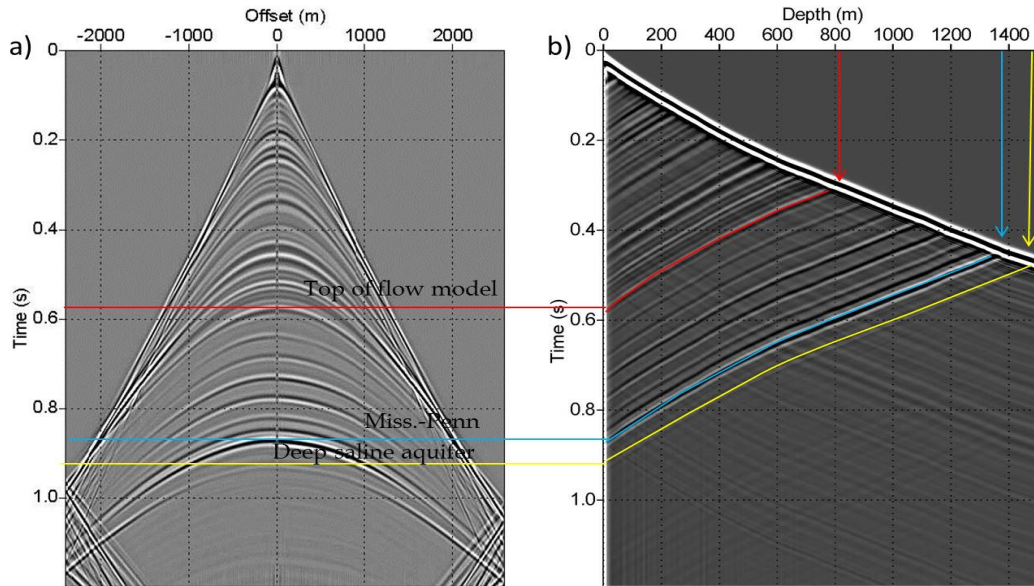


Figure 6.30. Acoustic forward modeling result for Year 0: (a) Shot gather (sx=2400), (b) VSP

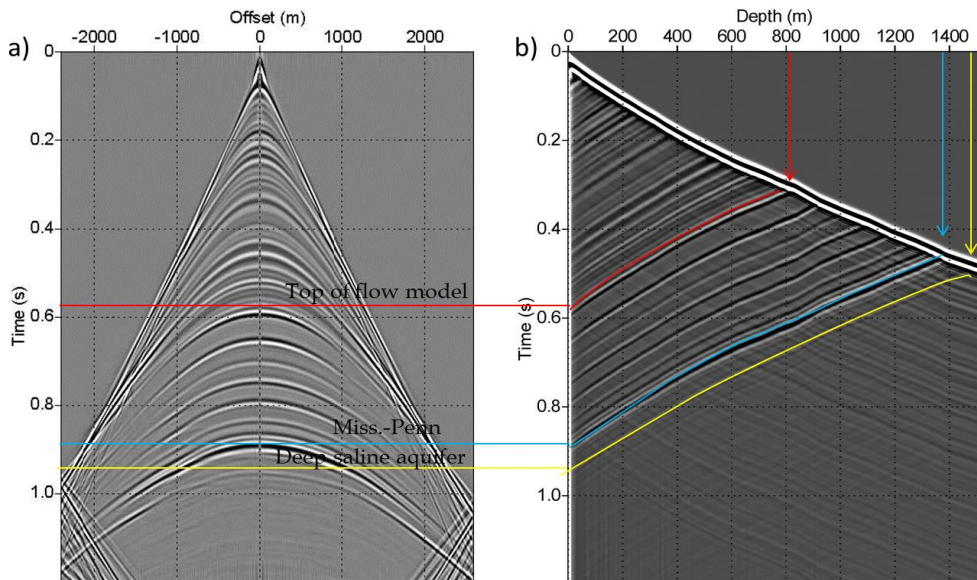


Figure 6.31. Acoustic forward modeling result for Year 250: (a) Shot gather (sx=2400), (b) VSP

6.5.2 Elastic forward modeling results

The input model for elastic forward modeling include both P and S wave velocities, as well as density shown in Figure 6.34 (year 0) and Figure 6.35 (year 250). It is assumed

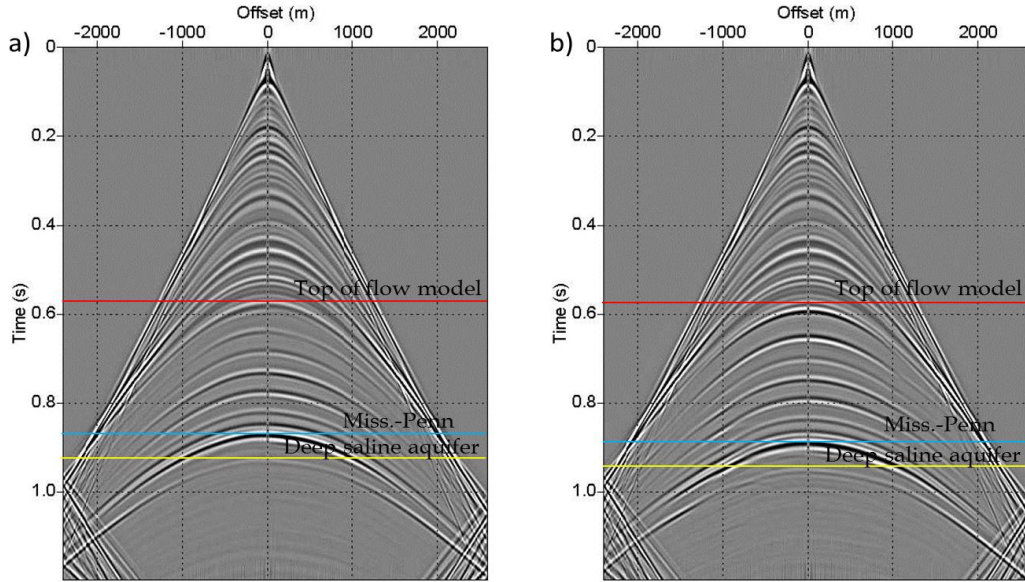


Figure 6.32. Shot gather ($sx=2400m$) from acoustic forward modeling results for (a) Year 0, (b) Year 250

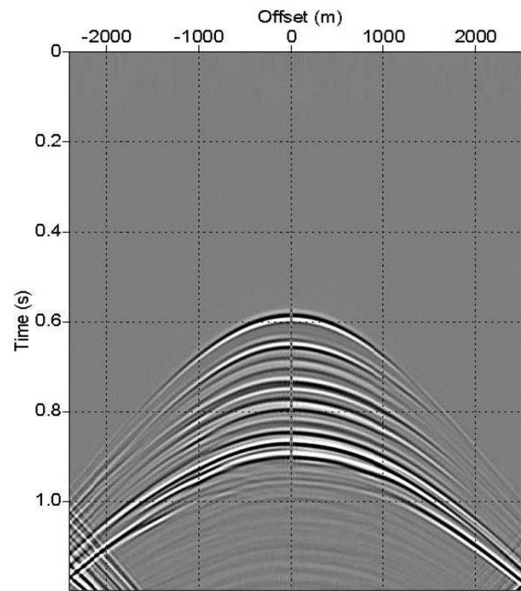


Figure 6.33. Difference from shot gathers ($sx=2400m$) year 0 and year 250 using acoustic forward modeling method.

that shear velocity is unaltered during Gassmann fluid substitution. The elastic forward modeling results include both horizontal and vertical components.

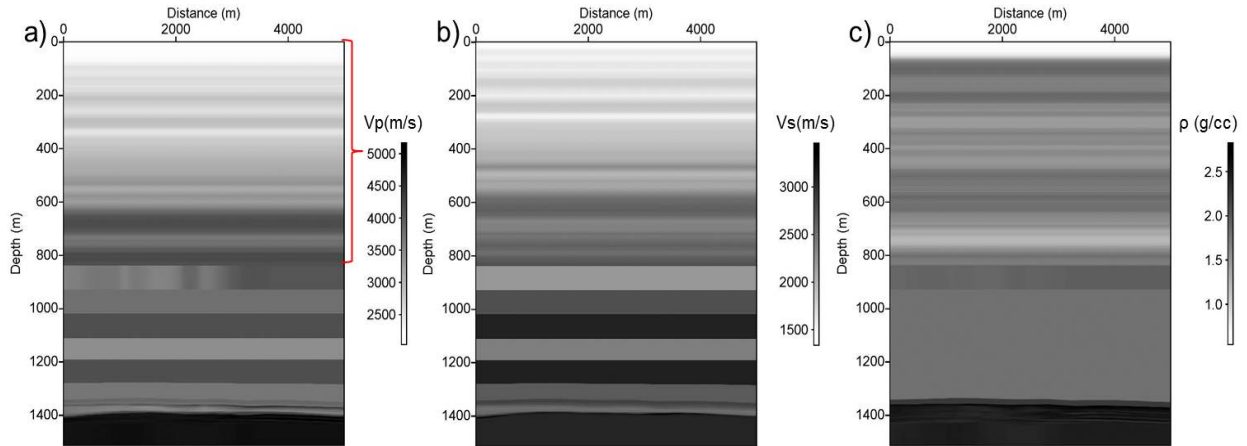


Figure 6.34. Input models for year 0: (a) V_p , (b) V_s , (c) Fluid saturated density. Red brackets are the part of the velocities added from the well Humphrey 4-18.

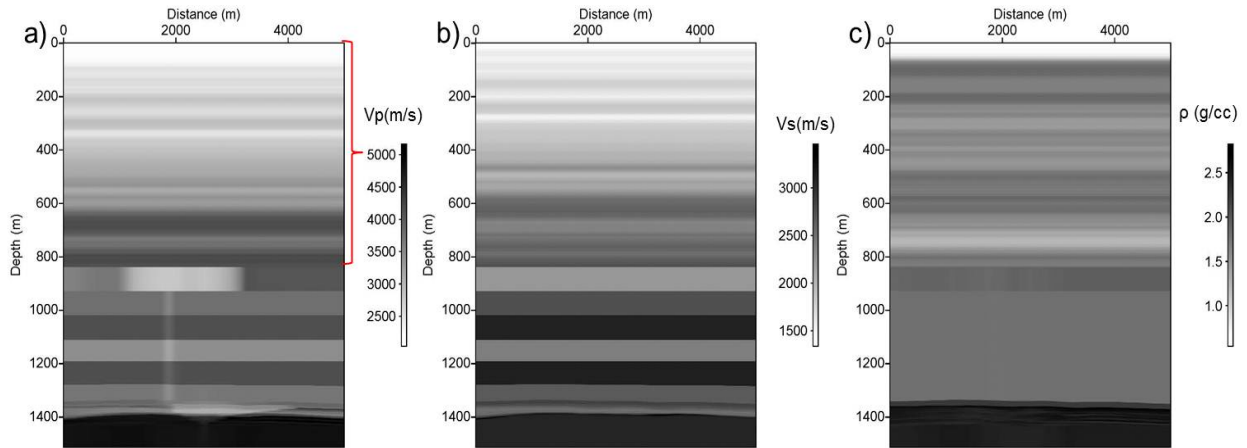


Figure 6.35. Input models for year 250: (a) V_p , (b) V_s , (c) Fluid saturated density

Figure 6.36 and Figure 6.37 show the elastic vertical component results for year 0 and year 250. VSP vertical component is again used to identify geological layers and a 5-10ms time shift is observed in Figure 6.38. Figure 6.39 shows the subtraction of results for these two

years.

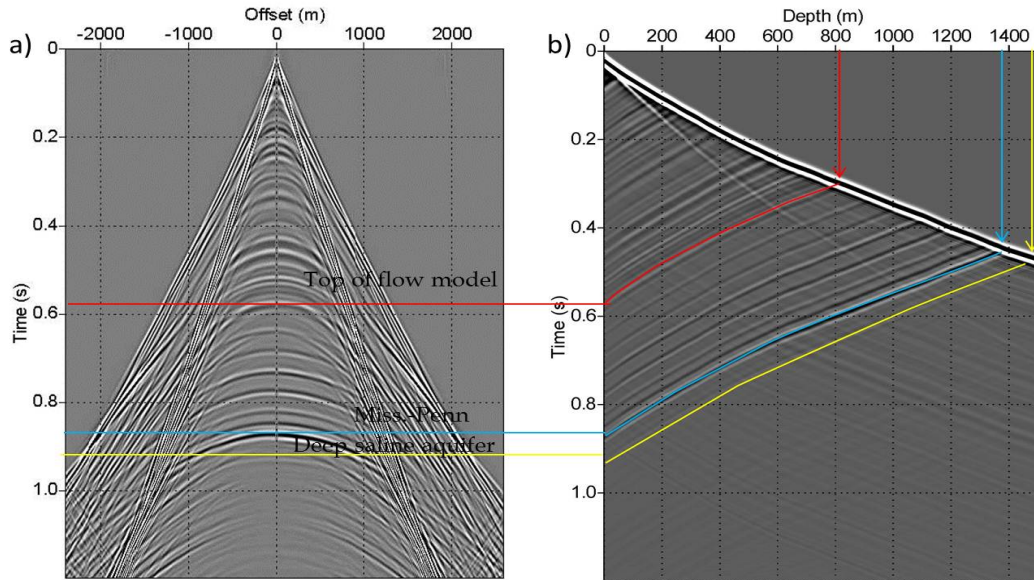


Figure 6.36. Elastic forward modeling results for Year 0: (a) Vertical component for shot gather (sx=2400), (b) Vertical component from VSP.

It is evident that elastic forward modeling shows more dispersion on the large offsets than the acoustic results. Generally, the vertical component for elastic forward modeling results should be same as the acoustic forward modeling results. By comparing the results for these two years (Figure 6.40 and Figure 6.41), the hyperbola curvatures for small offsets are quite identical, which validate this forward modeling algorithm. Again, time shift exists on the comparison of these two years, which shows similar features as on acoustic forward modeling results.

The seismic difference plot for year 0 and year 250 due to CO_2 injection for these two methods shown in Figure 6.42. For the same event, PP and PS reflections can be identified by different traveltimes and PS has larger traveltimes than PP. For the near offsets, the differences are identical; this PS converted wave starts to appear on larger offsets.

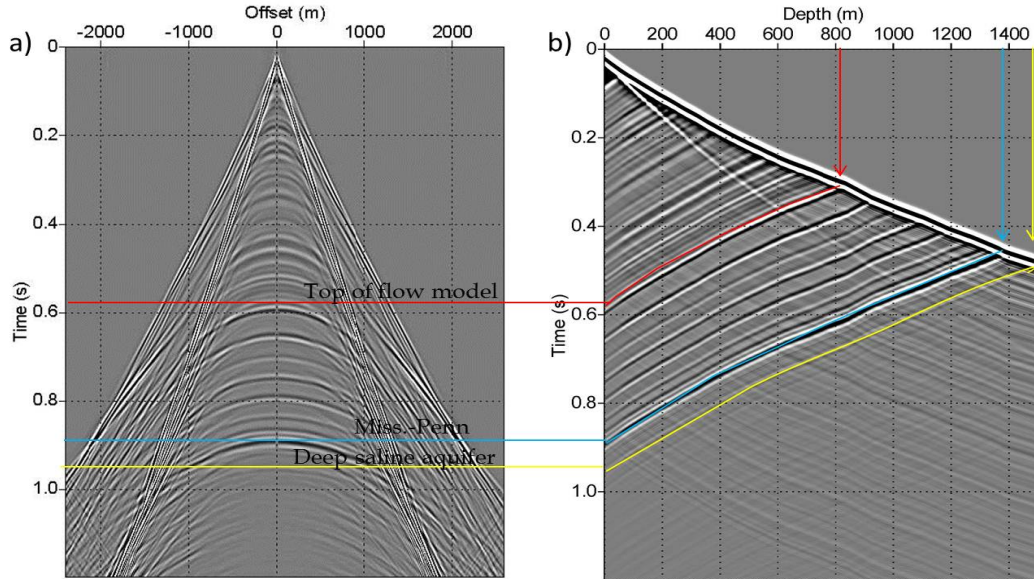


Figure 6.37. Elastic forward modeling results for Year 250: (a) Vertical component for shot gather (sx=2400), (b) Vertical component from VSP.

By simply comparing the wave types that are shown in acoustic and elastic forward modeling methods (Figure 6.43), PP and PS, surface waves are shown on the elastic forward modeling results that could be included in the results.

The elastic forward modeling results can provide horizontal components for both shot gather and VSP. This would help to identify PP and PS reflections that can be studied to characterize reservoir features. Notice that the polarity change starts at the shot location which is a general attribute for S wave, and no amplitude can be detected at the zero offset since the VSP geophones are located almost straight below the shot. P and S reflections are both identified from different traveltimes from the VSP. Note that the time shift is detected due to the decreased velocity where CO_2 was injected. By correlating surface seismic data and VSP results, the PP and PS reflections can be identified (Figure 6.44). This would help us to study different reservoir properties shown from PP and PS reflections.

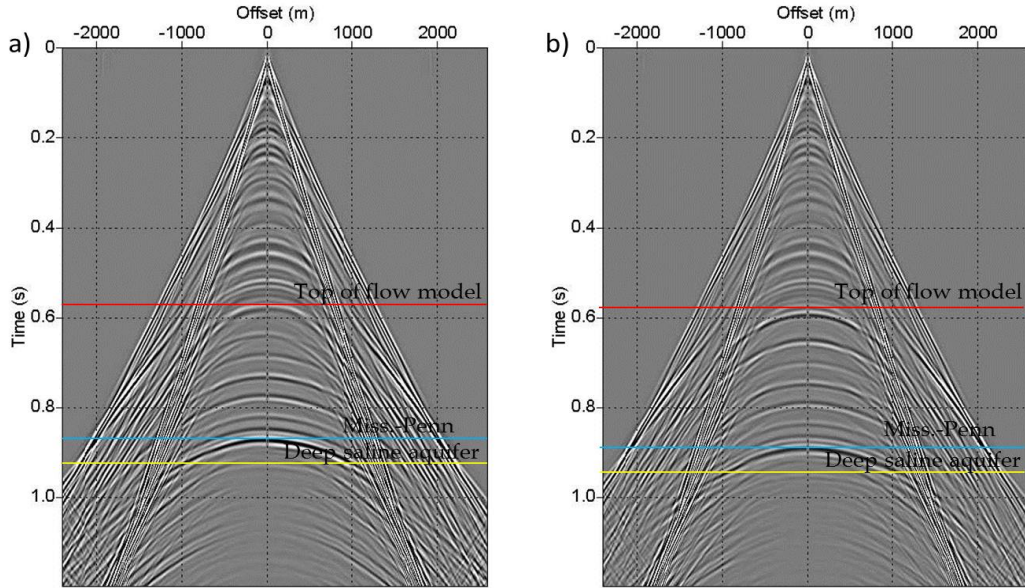


Figure 6.38. Elastic forward modeling results for (a) Year 0, (b) Year 250 (sx=2400).

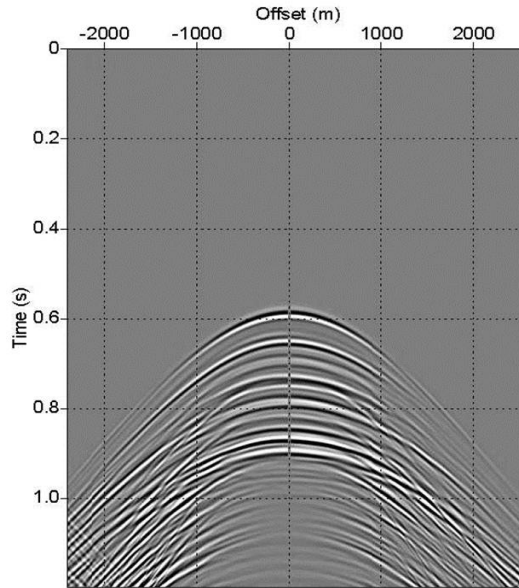


Figure 6.39. Difference from these two years via elastic forward modeling method (sx=2400)

To compare the horizontal component with the major events (top of flow model and deep saline aquifer) on the vertical component, the PP reflections from horizontal component

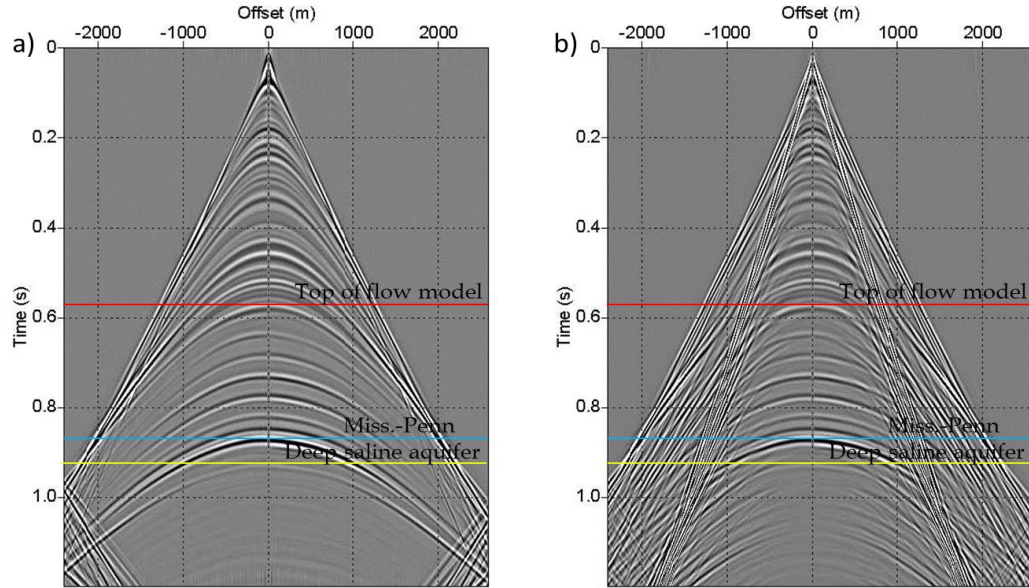


Figure 6.40. Comparison for the difference for year 0 by: (a) acoustic forward modeling method, (b) elastic forward modeling method.

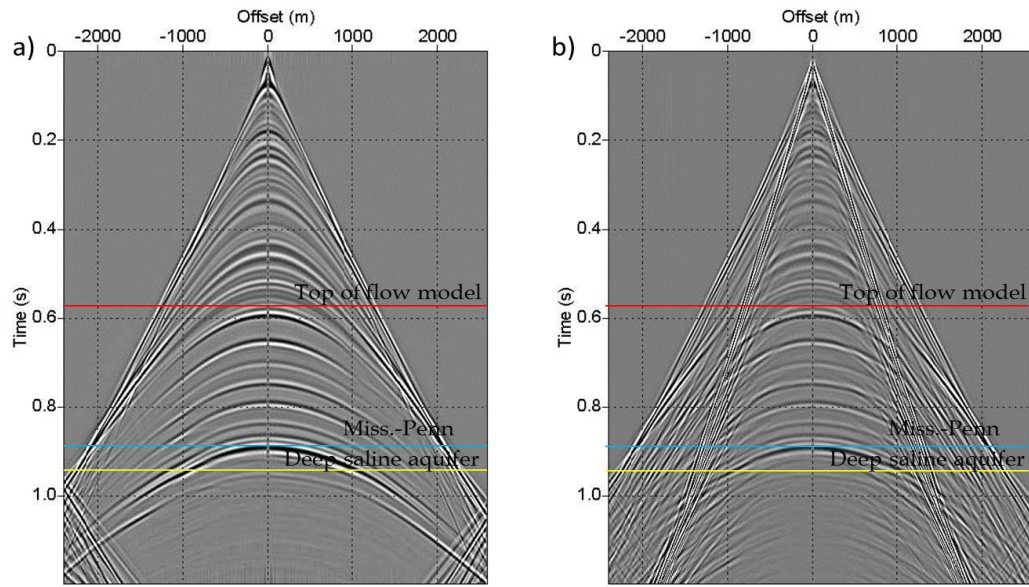


Figure 6.41. Comparison for the difference for year 250 by: (a) acoustic forward modeling method, (b) elastic forward modeling method.

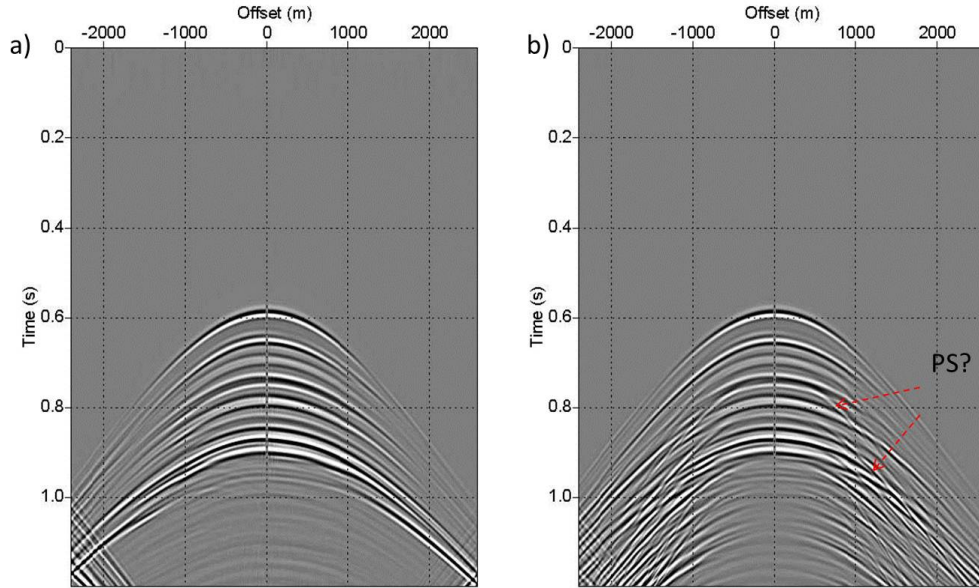


Figure 6.42. Seismic difference due to CO_2 injection for year 0 and year 250 from: (a) acoustic forward modeling method, (b) elastic forward modeling method.

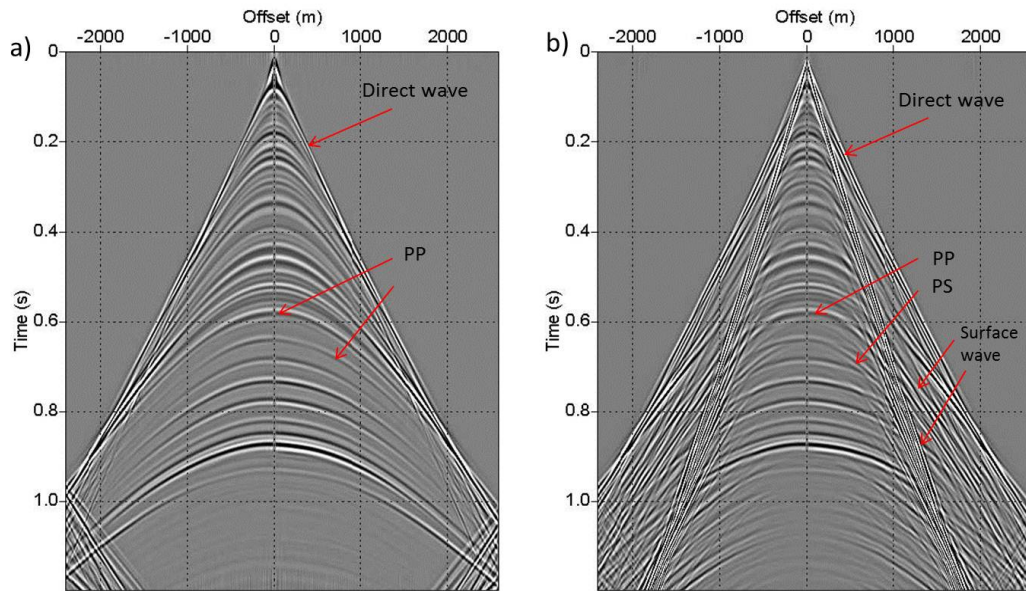


Figure 6.43. Wave types interpreted on the shot gather at year 0. (a) Acoustic forward modeling method. (b) Elastic forward modeling method.

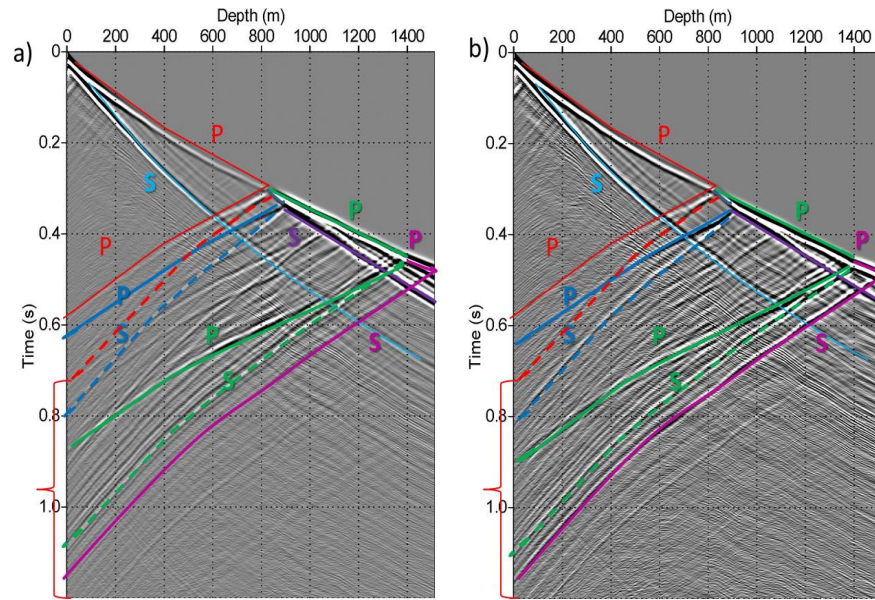


Figure 6.44. VSP horizontal component for: (a) year 0, and (b) year 250. P and S reflections are both identified. CO_2 saturation causes evident around 2ms time shift in the red bracket.

and vertical component match pretty well (Figure 6.46).

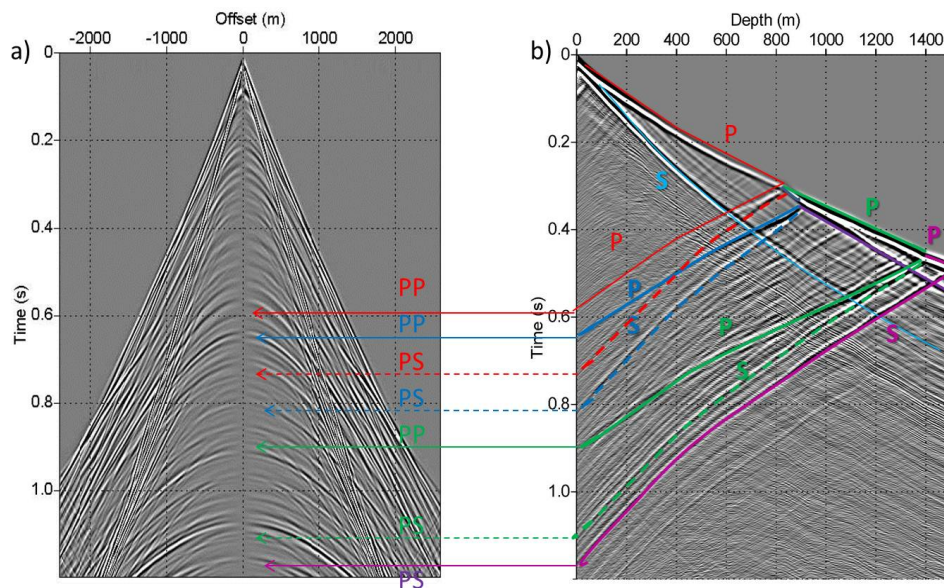


Figure 6.45. Year 250. (a) Horizontal component of shot gather, and (b) horizontal component of VSP.

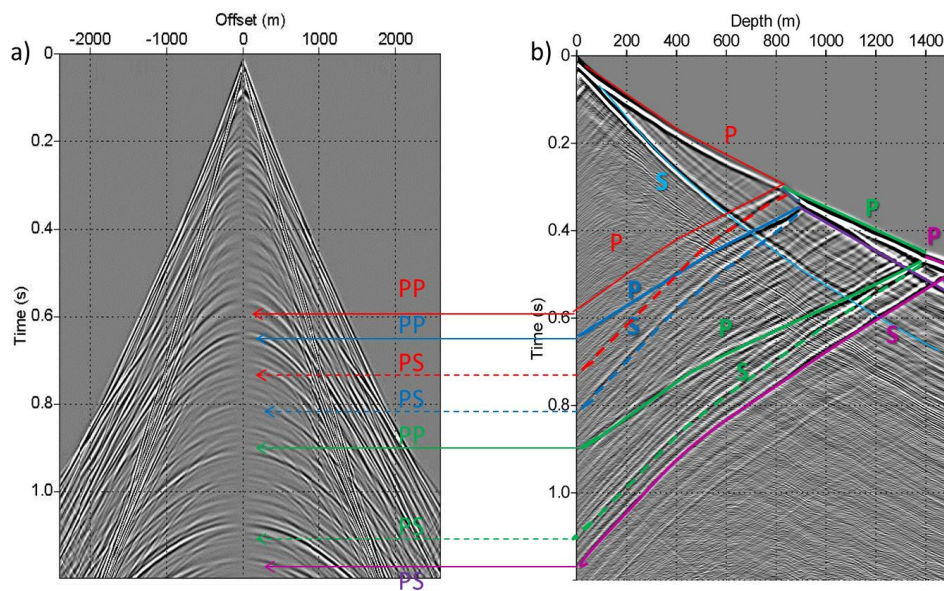


Figure 6.46. Year 250. (a) Horizontal component of shot gather, and (b) horizontal component of VSP.

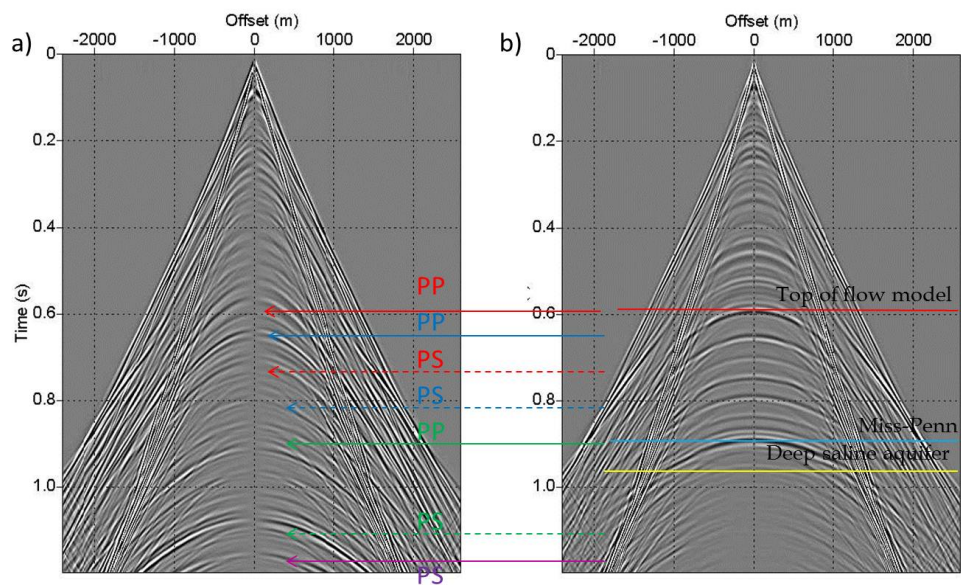


Figure 6.47. Shot gather for year 250. (a) Horizontal component, and (b) vertical component. PP reflections on both components match pretty well.

In addition, the VSP results can help identify the detailed geological layers for the Dickman Field. Table 6.4 shows the well tops for the well Humphrey 4-18.

Table 6.4. Well Tops for Humphrey 4-18

	A	B	C	D	E	F	G	H	I	J	K
1	Surface	TVDss	MD	TWT picked	TWT auto	Interpreter	SurfaceVELOCITY	DPOR	DT	GR-Original	RHOB
2	FortScott	-1843.00	4280.00	818.00	818.00	STEVE_S		9.79	78.56	116.74	2.542
3	CHEROKEE_GROUP	-1869.74	4306.74		825.89	WellPix	3882.70	21.57	79.45	237.56	2.341
4	BASE_PENN_LIME	-1910.00	4347.00		830.97	WellPix	5998.17	5.12	51.35	69.21	2.622
5	CHEROKEE_SAND	-1915.00	4352.00		831.60	STEVE_S	3248.26	19.95	94.82	140.92	2.369
6	LOWER_CHEROKEE_SS	-1949.00	4386.00		835.90	STEVE_S	4811.45	13.34	64.01	50.11	2.482
7	MISSISSIPPIAN	-1950.00	4387.00	836.02	836.02	STEVE_S	5025.37	10.09	61.29	44.39	2.538
8	MISS_PORO	-1962.28	4399.28		838.17	WellPix	4985.07		61.79	35.25	2.518
9	OSAGE	-2033.00	4470.00	848.00	848.00	STEVE_S	4656.86	12.56	66.14	38.08	2.495
10	GILMORE_CITY	-2105.00	4542.00	854.00	854.00	STEVE_S	4656.30	16.48	66.15	38.26	2.428
11	ViolaMidOr	-2163.00	4600.00		855.32						
12	MISS_OWC	-1981.00	4418.00		841.44	WellPix					
13	UOM1	-2076.00	4513.00		853.34		4709.41		65.40		2.433
14	KB	2437.00	0.00								

Figure 6.46 shows the type log of the Dickman field (depth in ft) and VSP result (depth in m). By reading the depth for the well tops from Table 3. Since some of the geological layers are adjacent which is beyond seismic resolution, only the geological layers that can be identified are assigned with the corresponding colors (Figure 6.48). The target area starts from the top of Fortscott to the base of Viola with a depth range of 1300m to 1535m. The two-way travelttime is mostly in the range of 0.85-0.95s. The shell script to perform this forward modeling is attached in **Appendix-C**.

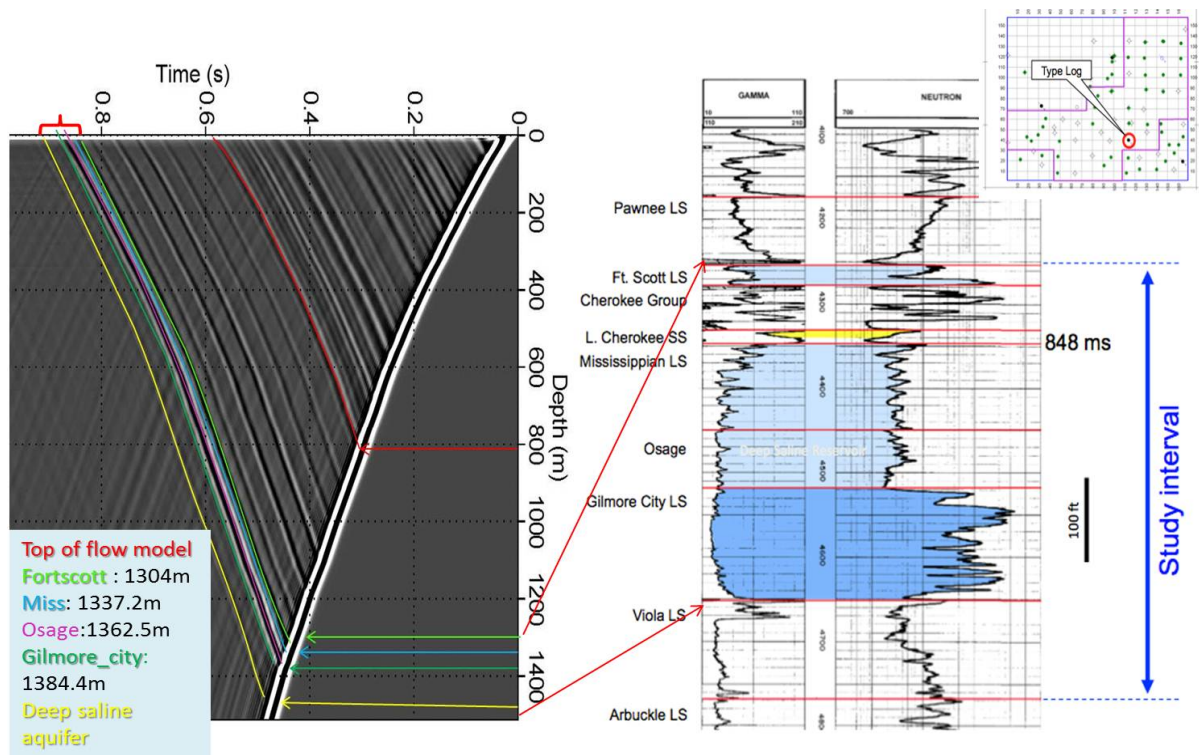


Figure 6.48. Well tops identified from the VSP results for the well Humphery 4-18 based on Table 6.4.

6.6 Discussion

Some comparisons for different simulation methods are discussed in this section, as well as the other models that have been investigated to be applied in this work. Design of different flow simulation scenarios may be applied for future research.

6.6.1 Comparison of 1D convolutional and 2D acoustic forward modeling

The 2D acoustic and elastic forward modeling results have been compared to show the difference by these two methods. One-dimensional convolutional forward modeling results have primaries only, and do not include any other wave types, however, they can still be compared with 2D forward modeling results. One-dimensional convolutional results are depth converted while the 2D acoustic forward modeling results are in time. The former represents the zero offset results while the latter is a shot gather with different offsets. In order to make a reasonable comparison, the zero offset trace from the acoustic modeling result has been taken out. For this zero offset trace, the V_p and density values can also be obtained from the previous input models. To this end, the reflectivity can be calculated from the V_p and density values for each depth interval, and a depth to time conversion is also performed to convert the reflectivity in time and then convolve with a Ricker wavelet with a dominant frequency of 35Hz. As mentioned earlier, in this flux correction transport equation for the elastic forward modeling, simply by setting V_s equal to zero may not purely represent acoustic forward modeling, so the SU command **Sufdmod2** which only deals with the acoustic forward modeling method is used for the comparison. It is assumed that these two methods should have similar seismic response because they both used P wave. The whole procedure is as follows:

- take out the velocity and density at the zero offset

-
- calculate the impedance and reflection coefficients
 - convert this reflectivity series from depth to time, and re-sampled to $dt=2\text{ms}$
 - convolve with the Ricker wavelet to obtain a seismic trace for comparison

The comparison results for year 0 are shown in Figure 6.47 (year 0). One-dimensional convolutional result is superimposed on the zero offset of 2D result. The major events are matched well, and shows that convolutional model can be used as an accurate alternative to finite difference forward modeling method only if zero offset data is needed.

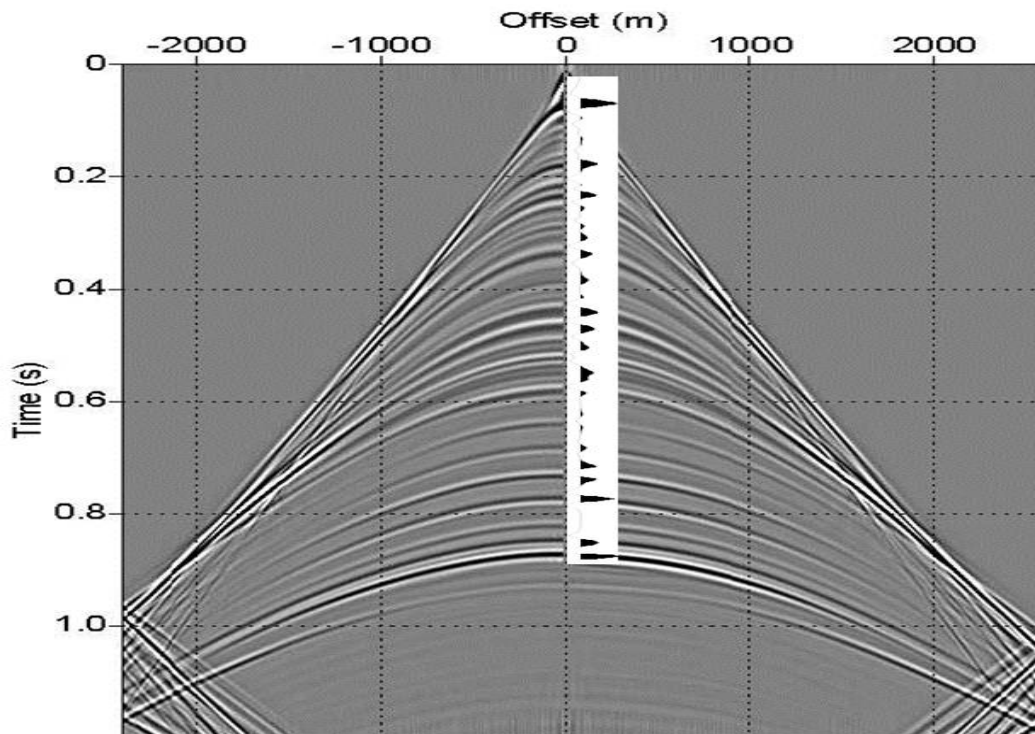


Figure 6.49. Comparison of 1D convolutional forward modeling and acoustic forward modeling results for year 0. 1D convolutional result is superimposed on the zero offset trace of 2D seismic data.

6.6.2 *Signal-to-noise ratio study*

In this study, we would like to find out how much signal-to-noise ratio is needed to image the CO_2 plume from the seismic simulation results. A signal-to-noise ratio (S/N) can be performed by adding some noise to the existing simulated response. This can help to identify the S/N ranges for detecting CO_2 flow paths from different seismic data quality. This can be realized by SU command **Suaddnoise** and a reasonable comparison asks for the normalization of seismic amplitude prior to any noise added. The steps are as follows:

1. find maximum amplitude for year 0 (m_0) and year 250 (m_{250})
2. calculate the ratio of m_0 and m_{250} (R)
3. choose a S/N value, and add noise to year 0, but noise of R times to year 250
4. subtract the images with noise added for both years, then the residual random noise in the difference image along with the signal difference can both be detected

A trial of different S/N ratios practices are shown below. Figure 6.49 shows the seismic data for year 0 and 250 with normalized amplitude shown on colorbar. S/N ratio starts from 1(Figure 6.50), 2 (Figure 6.51) and 10 (Figure 6.52), and have demonstrated seismic images with better quality. The results showed that in order to see the CO_2 plume, S/N ratio has to be at least 10.

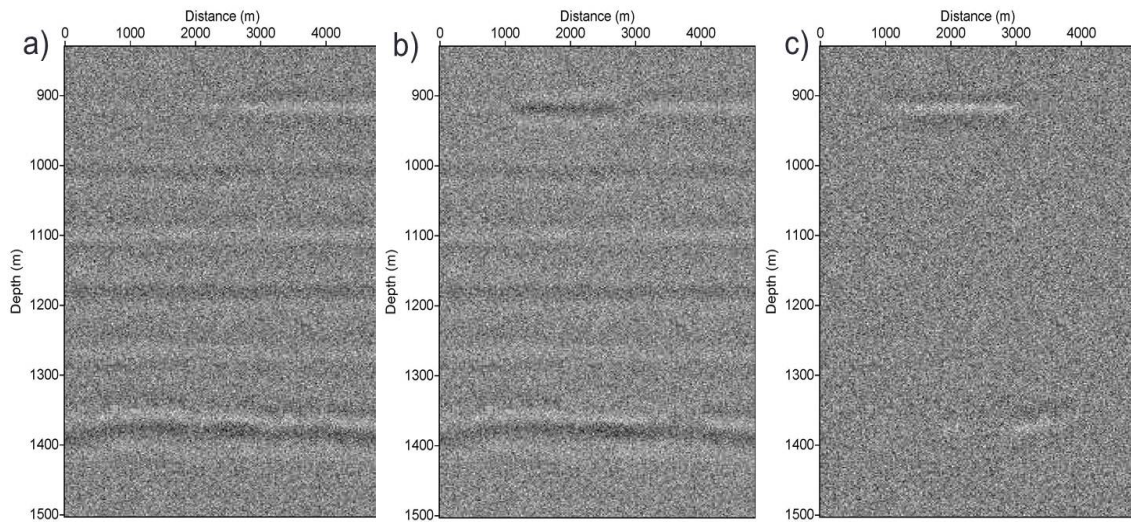


Figure 6.50. S/N is equal to 1. (a) year 0; (b) year 250; and (c) difference.

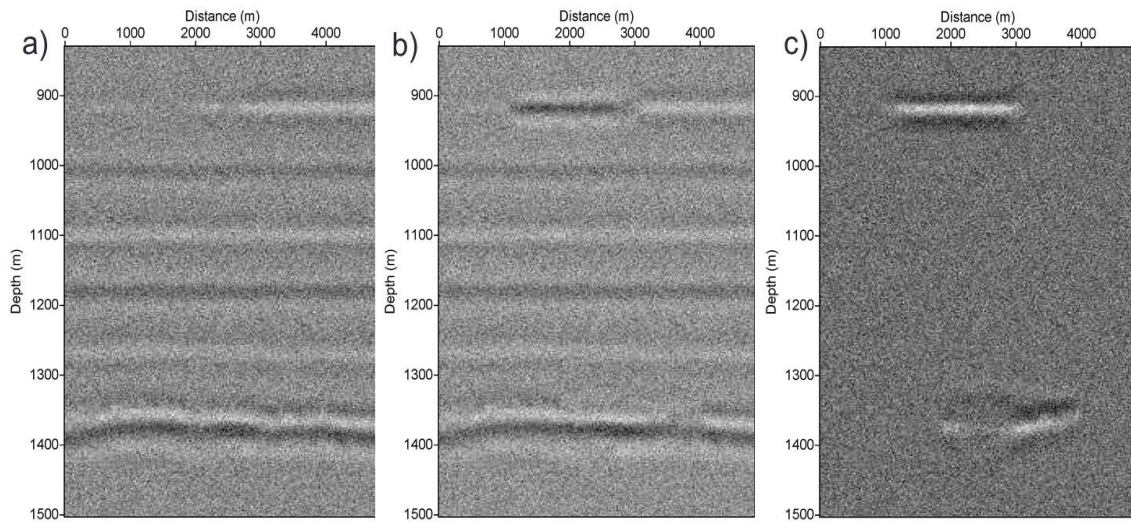


Figure 6.51. S/N is equal to 2. (a) year 0; (b) year 250; and (c) difference.

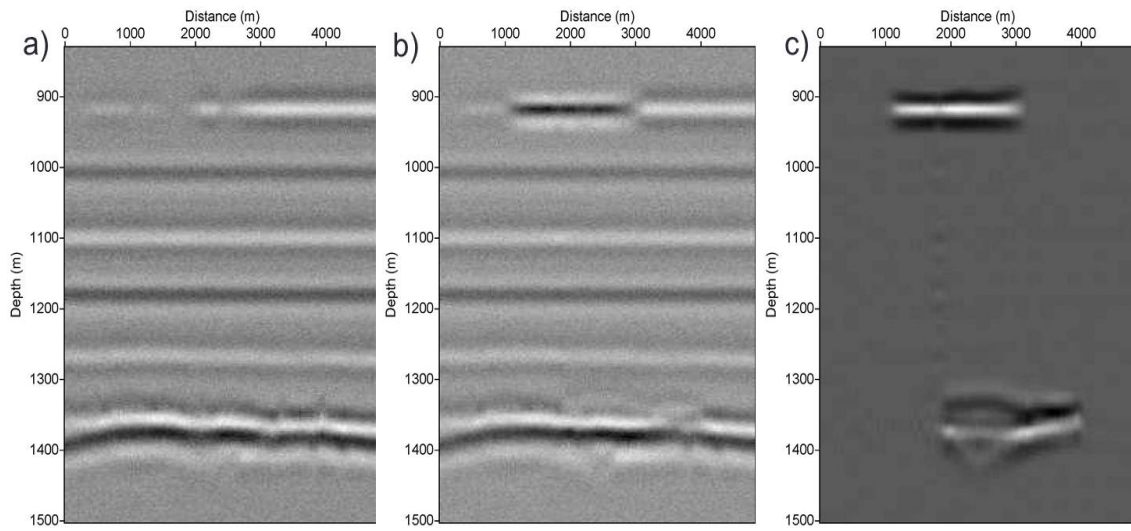


Figure 6.52. S/N is equal to 10. (a) year 0; (b) year 250; and (c) difference.

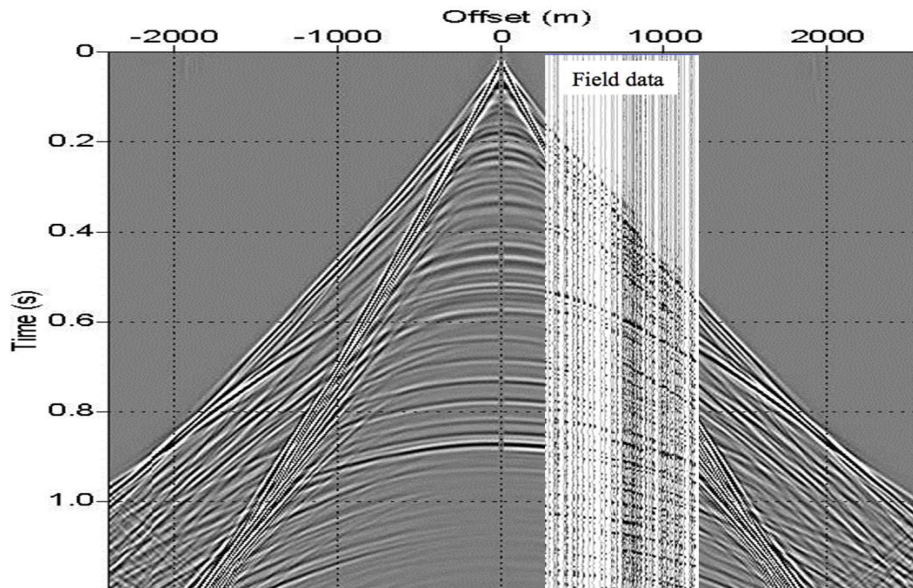


Figure 6.53. Field seismic data superimposed on the acoustic synthetic data (year 250). Red arrow shows the difference where there is CO_2 injection.

6.6.3 Comparison with the real seismic data

There is limited prestack seismic data for the Dickman field. A good comparison of our synthetic shot record with field data can help validate our work. The shot record for year 250 as the last year monitoring of CO_2 flow path is plotted. This shot record is obtained from acoustic forward modeling result which contains regular offsets. Our prestack field record does not have regular offsets, and has been sorted with the key header word (key=offset) to be comparable with the synthetic data. The images have been squeezed to make the best fit as the synthetics. Figure 6.53 showed the comparison of elastic synthetic (year 0) and prestack gather. The major PP events are matched considerably well, as well as the PS events showing slower events at the larger offsets. The comparison of acoustic synthetic for year 250 and prestack gather show a very good matching on the major events except difference on seismic images below the top of flow model due to CO_2 injection (Figure 6.54).

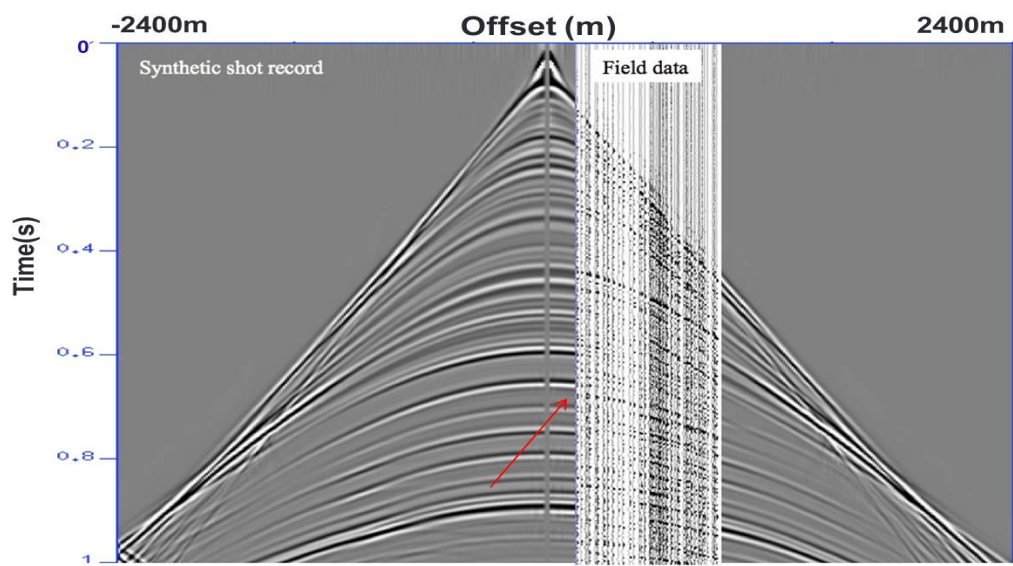


Figure 6.54. Field seismic data superimposed on the elastic synthetic data (year 0).

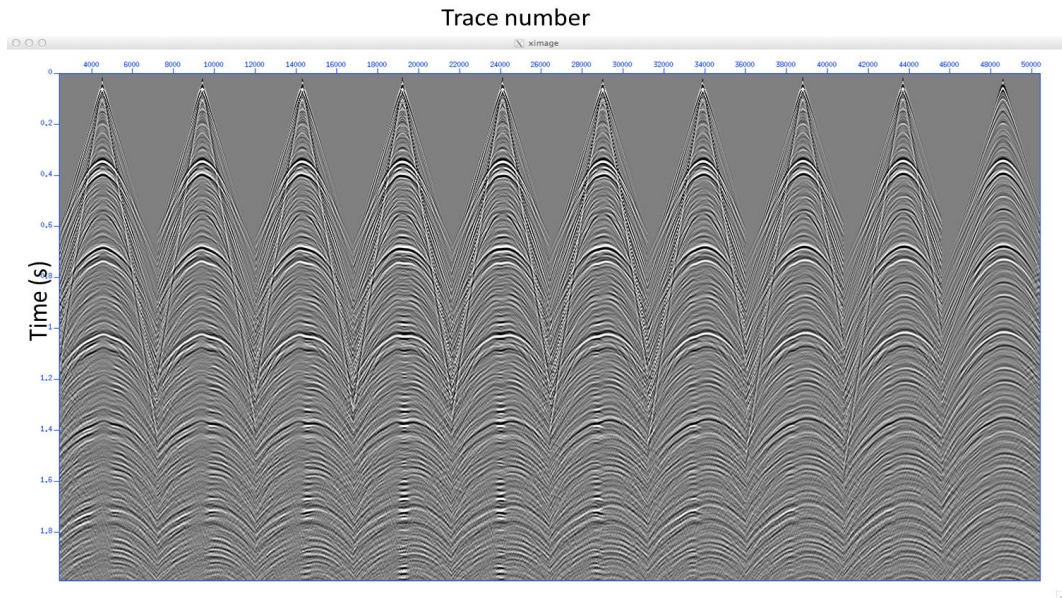


Figure 6.55. Shot gathers using acoustic forward modeling results for sx ranging from 2100-3000m in year 0.

6.6.4 Multiple shot gathers

In addition, shot gathers have been generated for both 2D acoustic and elastic forward modeling methods and for both velocity models (Figure 6.55). The shot gathers have shown the locations where have been affected by CO_2 leakage (Figure 6.56). These prestack shot gathers can be processed and stacked, which should be no much difference as compared with the plane wave results. However, they can still be further investigated if migration is applied and seismic images can be compared.

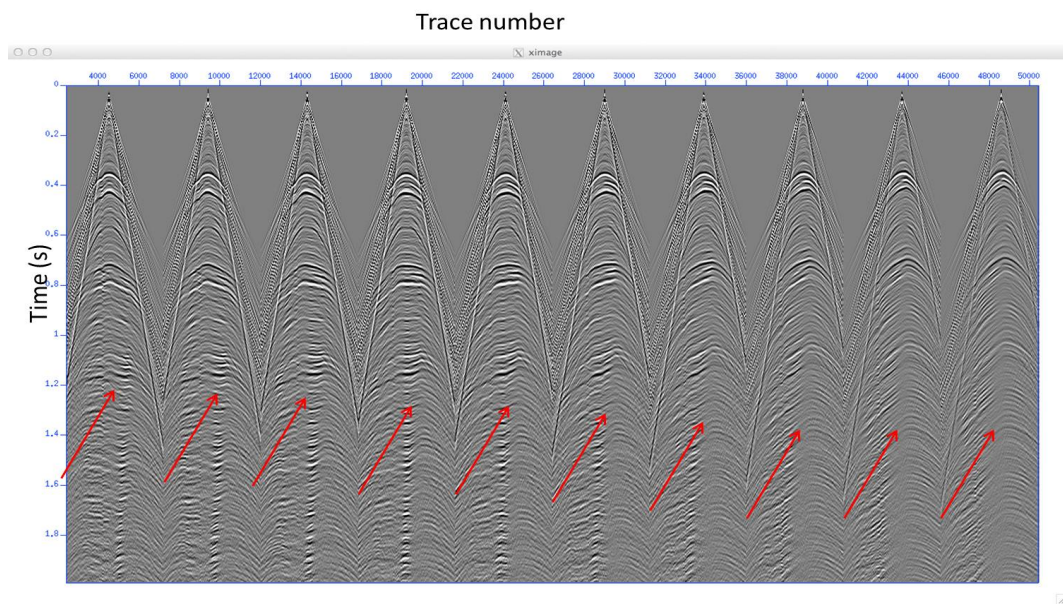


Figure 6.56. Shot gathers using acoustic forward modeling results for sx ranging from 2100-3000m in year 250. Note that the reflections affected by CO_2 injection.

6.6.5 Horizontal injection design

On the flow simulation side, only one vertical well injection was studied in this work. However, there are additional simulation sceneries have been tested in the flow simulation model. It has been proved that for horizontal well injection, the trapping efficiency can be increased from 8-10% with CO_2 only, and 56% to 94% for CO_2 injection with water. These would be interesting tests from the seismic simulation results in the future study. For the leakage test a fault is added on the cap rock, and CO_2 leakage scenario is built which has been seldom studied by other researchers. With insufficient theory based on Gassmann fluid substitution, this leakage scenario can still be tested in seismic simulation and has given reasonable results.

In summary, we have shown a CO_2 plume in WIP aquifer sites that can be detected from seismic changes before and after CO_2 injection, and the seismic changes are highly correlated to the CO_2 saturation change. 3D seismic data may also provide a volumetric quantity by looking at different seismic lines or depth slices. The average velocity change before and after injection is 500-600m/s, leading to a seismic amplitude of 10 percent. Changes on the same seismic line at various time intervals can help to monitor CO_2 flow paths and to determine distribution. However, some uncertainty arises due to simplified (convolutional) modeling when using Gassmann fluid substitution for calculating carbonate rock properties or shale. Moreover, the better estimation for carbonate bulk modulus or fracture reservoirs can be used from previous studies (Hudson, 1981; Adam *et al.*, 2006; Vega *et al.*, 2010;). The velocity models for V_p and V_s were obtained from a single well (Humphery 4-18), but this limited data may bring full waveform inversion results which recently is made available for the Dickman field (Phan and Sen, 2010).

With daily injection 368 tons of CO_2 for continuous 250 years, CO_2 plume can be identified

from simulated seismic response. With 1D convolutional forward modeling, this simulated 3D seismic cube can clearly track the CO_2 flow paths in both cross-section view and map view. The amount of CO_2 may be estimated in the zonal and areal distribution, and this result can be compared with that from flow simulation to be validated. In the flow simulator, it is always unrealistic to regrid the data to match the finer details of fluid properties in the cell due to expensive computational cost, and this can be realized in seismic simulation in this study. By using different seismic simulation methods, this regridded cell size can be efficiently small and computational cost is reasonable, and for the most time is low (for 2D case).

Overall, for the mid-continent, hard rock and complex geology structure (unconformity, truncations and pinch outs), CO_2 flow path can be mapped from 4D seismic. Elastic forward modeling results can provide more realistic results than acoustic forward modeling.

6.7 *Other attempts: Prestack inversion result from UT*

This dissertation has gone through several trial velocity estimations to accurately obtain a good starting velocity model for Gassmann fluid substitution. However, due to the limited data for the seismic survey (only one well has healthy sonic curve that has the deepest penetration to the saline aquifer), this estimation has been adjusted and tested a few times. One big effort was paid to inversion results that were provided from previous studies (Phan and Sen, 2010). Their volume is calculated from the same seismic data, so it mimics the same seismic survey outline. However, due to the noisy content of the models (also in time domain instead of in depth) and insufficient information for depths, it may not be a good candidate for providing a reliable initial velocity estimate. Below is the whole process that has been done to ultimately utilize this input velocity model and it also explained why it is

not used in this study.

They employed pre-stack seismic inversion to successfully estimate some reservoir parameters (V_p , V_s and density). First of all, well logs with post-stack seismic data using synthetic seismograms are tied at the well locations. Then pre-stack gathers are converted into angle gathers, and the angle that ranges between 5 and 30 degrees with a 6-degree increment are chosen. The next step is starting models of impedance for P and S waves and density is created by well log interpolation and extrapolation, which is guided by interpolated horizons to invert pre-stack angle gather using a linearized version of Zoeppritz equation to obtain the updated impedance volumes and density. These are used as attributes to estimate porosity using a multi-attribute linear regression approach (Hampson et al., 2001).

These volumes have a time window from 750ms to 910ms, covering the geologic section of Mississippian and Pennsylvanian unconformity (the storage cite). Since there is no information in the data above 750ms, the time depth pairs are obtained from the well Elmore3. The depth range for the flow simulation model is known from 838m to 1493.5m. From the time depth function, they corresponding to the time at 570ms. So a constant V_p velocity using these two points at 570ms (838m) and 750ms (1191.8m) is used to cover the data above 750ms. The V_p/V_s ratio is also unknown, a constant $V_p/V_s=2$ is used to estimate the V_s velocity. After the data has been filled up in the shallow section, a time to depth conversion is performed. The depth window is constrained to that of flow simulation model (838m to 1493.5m).The original seismic survey and prestack inversion results both have 158 inlines and 122 cross-lines with a seismic bin size of 25m x 33.5m. The prestack inversion results that include V_p and V_s velocities are used to be compared with the V_p and V_s obtained from one well (Humphery 4-18) estimation. The survey outlines of the prestack inversion results and the flow simulation results have different coordinate origins, but have some overlap in the data area. The outline has to be modified to switch to (4 761 700,

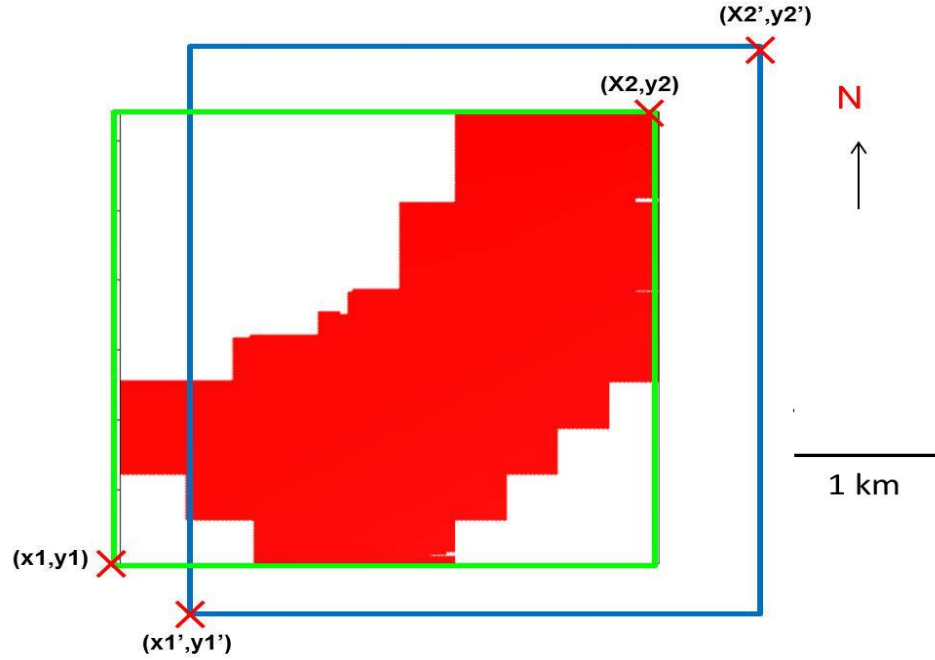


Figure 6.57. Resize the outline of prestack inversion results (UT) (green) to that of reservoir simulation model (blue).

210 320) and (479 560,214 220) and expand the data to the corner at (481 050,214 890) as shown in Figure 6.57. Note that the prestack inversion results outline has an irregular shape and SEG Y data are composed of live traces which have different source and receiver locations due to this irregularity. In order to bring these live traces and reshape their outline, zero traces in the empty section need to be added to reconstruct a regular survey outline. First, the SEG Y data was sorted into the header word **sy** (source y coordinates) to obtain the number of traces for each y coordinate, and then manually count for number of traces and the results are stored in the excel sheet (Figure 6.58). This data sheet gives the information for each y coordinate, the first and the last traces x coordinates and number of traces for this **sy** information. This is used to load the data from SU to Matlab with correct indices and placed onto a regular 3D grid. The input file is composed of 10559 traces, and is mapped to a regular grid with 194 inlines by 122 cross lines. The original output for the live

traces information from SEG Y data is shown in Figure 6.58. So for each inline or crossline, seismic data from the irregular survey outline will be repositioned with the correct index in 3D seismic cube which has 158 inlines and 127 cross-lines. After this step, the empty section where there was no seismic data lined up will be filled with the very first or last column of the seismic data for each inline. Figure 6.59 shows copying the data for one side, and Figure 6.60 shows the completed one on both sides.

For the vertical direction, the data has 81 time steps with $dt=2ms$. These volumes are in time domain which covers a 160ms time window (750ms 910ms), representing from Fort Scott to Mississippian and Pennsylvanian unconformity (the storage site). According to the only time-depth table available from the well Elmore-3, this time window represents the depth from around 1191m. The depth range for the flow simulation model is known from 2750ft (838m) to 4950ft (1510m), so the missing velocity information from 838m to 1191m has to be filled. This process includes extrapolating the data upward from 750ms to 570ms (around 838m), and converting it to depth to exactly match the flow simulation model.

The procedure of time to depth conversion is a little tricky. Due to insufficient information of existing data, the depth range for the V_p and V_s model is unknown, except the time window from 750ms to 910ms. Based on the only well (Elmore-3) with time-depth tables, the two points are known at the 838m (0.57s) and at the 1509m (0.75s). This section is not our storage target, so an averaged velocity model may be adequate. So instead of doing a linear velocity model that may bring unnecessary information, a constant V_p velocity is assigned to the section between the two points at 570ms (838m) and 750ms (1191m) to represent geological model. Once this velocity is fixed for the shallow depth section, the time to depth conversion is performed with the time accumulation calculated from velocity variations at the user-defined depth grid cell. After this step is complete, the vertical depth range has been constrained to that of flow simulation model. The seismic bin size is 110ft(33.5m) by

gx	sx (first)	sx(last)	number of traces
690025	1563013	1568073	47
690107	1563013	1567413	41
690190	1563013	1567853	45
690272	1563013	1568073	47
690355	1563013	1568073	47
690437	1563013	1568073	47
690520	1563013	1568073	47
690602	1563013	1568073	47
690685	1563013	1568073	47
690767	1563013	1568073	47
690850	1563013	1568073	47
690932	1563013	1568073	47
691015	1563013	1568073	47
691097	1563013	1568073	47
691180	1562243	1569393	66
691262	1562243	1569393	66
691345	1562243	1569393	66
691427	1562243	1569393	66
691510	1562243	1569393	66
691592	1562243	1569393	66
691675	1562243	1569393	66
691757	1562243	1569393	66
691840	1562243	1569393	66
691922	1562243	1569393	66
692004	1562243	1569393	66
692087	1562243	1569393	66
692170	1562243	1569393	66
692252	1562243	1569393	66
692335	1562243	1569393	66
692417	1562243	1569393	66
692500	1562243	1570713	78
692582	1562243	1570713	78
692665	1562243	1570713	78
692747	1562243	1570713	78
692830	1562243	1570713	78
692912	1562243	1570713	78
692995	1562243	1570713	78
693077	1562243	1570713	78
693160	1562243	1570713	78
693242	1562243	1570713	78
693325	1562243	1570713	78
693407	1562243	1570713	78
693490	1562243	1570713	78
693572	1562243	1570713	78
693655	1562243	1570713	78
693737	1562243	1570713	78

Figure 6.58. The prestack inversion results live traces information to be imported into Matlab and were filled with empty traces.

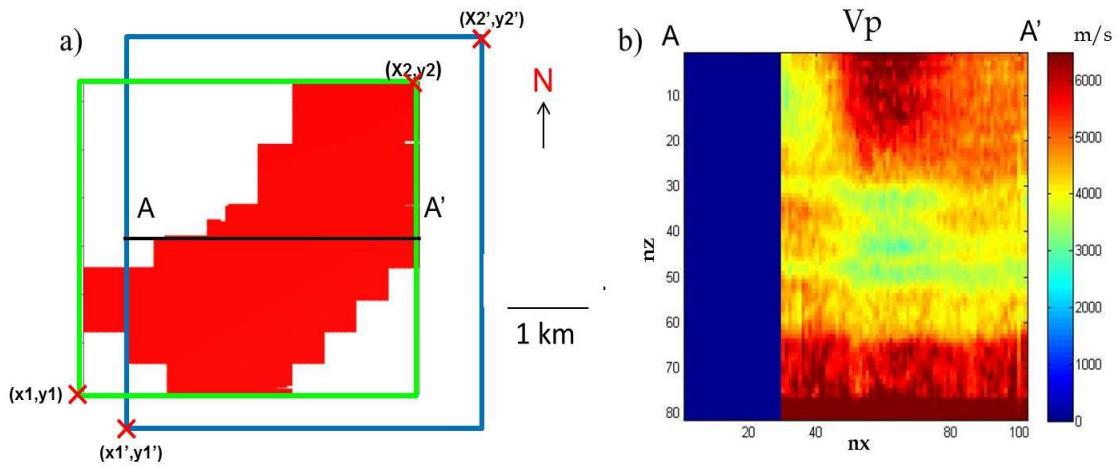


Figure 6.59. The resized data has empty traces on one side.

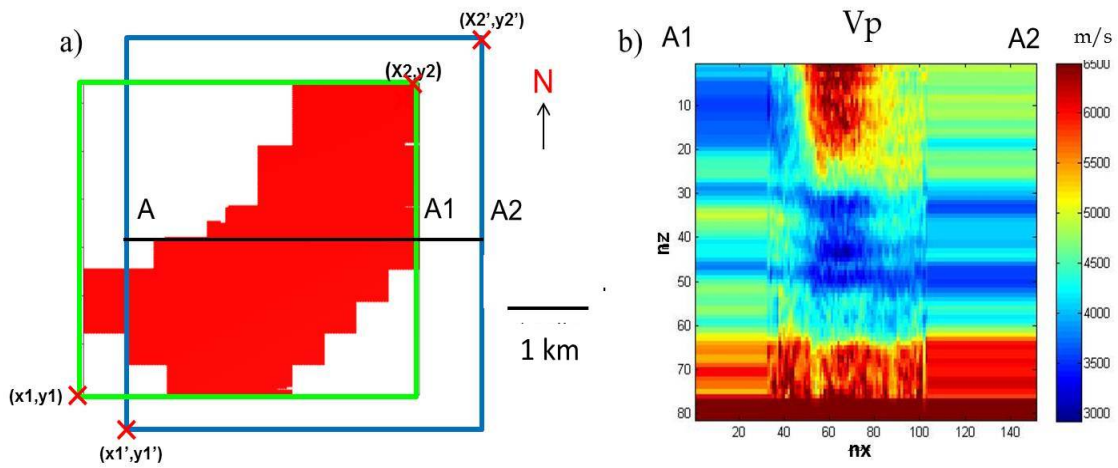


Figure 6.60. Extrapolate the data on both sides by copying the first and last row for this seismic line.

82.5ft (25m), and will be interpolated into 82.5ft (25m) by 82.5ft (25m). Now the modified V_p and V_s velocity models have the same depth range and (x,y) increment as the flow simulation model, so the Gassmann fluid substitution can be applied directly. However, this model is not used because of noisy content and insufficient data coverage, even though after these processing steps have been applied, the interpolation results still have many artifacts that would greatly hamper the forward modeling results.

7. SUMMARY

This research presents a CO_2 sequestration work flow that links flow simulation output with seismic simulation for a complex carbonate reservoir in the Dickman oil field. Previous investigations rarely involve a complex flow simulation model that has variable thickness for a grid layer while assume uniform thickness for the geological model. Hence, uncertainties may arise when defining spacing of the property grid and seismic grid. Generally speaking, flow simulation models and seismic surveys have different spatial scales. In a Cartesian coordinates, the flow grid could be regular in x and y axis and irregular in the z axis. on the contrary, a desired seismic grid is regular in all the x, y and z direction. In addition, the flow grid size (dx,dy) is generally much larger than the seismic grid size(dx,dy), which requires downscaling from the flow grid to the seismic grid. It becomes more complicated in the vertical (z) direction things. The irregular flow grid size (dz) may range from zero (unconformity) to the order of 30m, while the seismic grid size (dz) is on the order from 1 to 3m. Depending on the thickness of each individual block, either upscaling or downscaling may be required for the regridding. The missing section must be addressed carefully since every point in an earth model for seismic simulation must contain parameter values.

Gassmann fluid substitution is used to obtain rock properties at different time in the flow simulation. 1D convolutional forward modeling is used as the seismic simulation. The variations of seismic response characteristics due to CO_2 injection can be detected and correlated to CO_2 saturation. Future work includes seismic simulation using finite difference 3D acoustic and elastic forward modeling, which is expected to characterize more details of reservoir changes on seismic response due to CO_2 plumes at the Dickman site.

The contribution of this research is that the detailed working flow for different regridding processes represents a unique approach to link the complex flow simulation model to help

monitoring CO_2 capture and storage. This work shows the procedures for dealing with the majority of flow simulation scenarios, and it can be used as a reference for resolving the difficulty in re-scaling issues that may be encountered in many cases.

Open issues for future research include: (1) modified Gassmann fluid substitution theory to more accurately calculate the bulk modulus for carbonate and shale; (2) apply Hudson's crack model to study CO_2 leakage from the seal layers of normally shale. The changes reflected on seismic may be trivial; (3) 3D acoustic and elastic forward modeling methods to simulate 3D CO_2 plumes can better help identify the quantity and location of CO_2 fluid flow paths.

REFERENCES

- ADAM, L., MICHAEL, B., AND IVAR, B. 2006. Gassmann's fluid substitution and shear modulus variability in carbonates at laboratory seismic and ultrasonic frequencies. *Geophysics* 71, 173–183.
- AL-NAJJAR, N. F., BREVIK, I., PSAILA, D. E., AND DOYEN, P. M. 1999. 4d seismic modelling of the Statfjord Field: Initial results. *SPE Annual Technical Conference and Exhibition, 56730-MS, October 1999, Houston, Texas.*
- AVANSI, G. D., DE SOUZA, R. M., AND SCHIOZER, D. 2010. Scaling issues through quantitative analysis between reservoir simulation. *Society of Petroleum Engineers, 131632, June 2010, Barcelona, Spain.*
- BACHU, S. 2003. Screening and ranking of sedimentary basins for sequestration of CO_2 in geological media in response to climate change. *Environmental Geology* 44, 277–289.
- BAES, C.F., B. S. AND LEE, D. W. 1980. *The collection, disposal and storage of carbon dioxide. in: Interactions of Energy and Climate (eds Bach, Prankrath and Williams).* The Netherlands: D. Reidel Publishing Co.
- BATZEL, M. AND WANG, Z. 1992. Seismic properties of pore fluids. *Geophysics* 57, 1396–1408.
- BENTHAM, M. AND KRIBY, G. 2005. CO_2 storage in saline aquifers. *Oil and Gas Science and Technology* 60, 559–567.
- BOOK, D. L., B. J. P. AND HAIN, K. 1975. Flux-corrected transport ii: generalization of the method. *J. Comput. Phys.*, 18, 248–283.

- BORIS, J. P. AND BOOK, D. L. 1973. Flux-corrected transport. i. shasta, a fluid transport algorithm that works. *J. Comput. Phys.* 11, 38–69.
- BRINKS, J. AND FANCHI, J. 2001. Geologic sequestration: Modeling and monitoring injected CO_2 . *SPE Annual Technical Conference and Exhibition, 66749-MS, February 2001, San Antonio, Texas.*
- CARR, T., MERRIAM, D., AND BARTLEY, J. 2010. Use of relational databases to evaluate regional petroleum accumulation, groundwater flow, and CO_2 sequestration in Kansas. *AAPG Bulletin* 89, 1607–1627.
- CASTRO, S. A. AND CAERS, J. 2005. Flow-based downscaling of coarse grid saturations for modeling 4d seismic response. *SEG Expanded Abstracts* 24, 2504–2507.
- CHADWICK, A., WILLIAMS, G., DELEPINE, N. AND CLOCHARD, V., AND LABAT, K. 2010. Quantitative analysis of time-lapse seismic monitoring data at the Sleipner CO_2 storage operation. *The Leading Edge* 29, 170–177.
- COHEN, J. K. AND STOCKWELL, J. J. W. Cwp/su: Seismic un*x release no.42: an open source software package for seismic research and processing, center for wave phenomena, Colorado School of Mines.
- DAVIES, D. AND MAVER, K. 2004. 4d time-lapse studies and reservoir simulation to seismic modeling. *Offshore Technology Conference, 16934-MS, May 2004, Houston, Texas.*
- DODDS, K. AND SHARMA, S. 2009. Developing a monitoring and verification plan with reference to the Australian Otway CO_2 pilot project. *The Leading Edge* 28, 812–819.

- DOYEN, P., PSAILA, D., ASTRATTI, D., KVAMME, L., AND AL-NAJJAR, N. 2000. Saturation mapping from 4-d seismic data in the Statfjord field. *Offshore Technology Conference, May 2000, Houston, TX.*
- EMERICK, A. A., DE MORAES, R. J., AND RODRIGUES, J. R. 2007. Calculating seismic attributes within a reservoir flow simulator. *SPE Annual Technical Conference and Exhibition, 107001-MS, April 2007, Buenos Aires, Argentina.*
- ENCHERY, G., LE RAVALEC-DUPIN, L., AND ROGGERO, F. 2007. An improved pressure and saturation downscaling process for a better integration of 4d seismic data together with production history. *EUROPEC/EAGE Conference and Exhibition, 107088-MS, June 2007, London, U.K..*
- ETGEN, J. T. AND O'BRIEN, M. 2007. Computational methods for large-scale 3D acoustic finite-difference modeling : A tutorial. *Geophysics 72*, SM223–230.
- FANCHI, J. R. 2001. Feasibility of monitoring CO_2 sequestration in a mature oil field using time-lapse seismic analysis. *Society of Petroleum Engineers Annual Technical Conference and Exhibition, February 2001, San Antonio, Texas.*
- FEI, T. AND LARNER, K. 1995. Elimination of numerical dispersion in finite-difference modeling and migration by flux-corrected transport. *Geophysics 60*, 6, 687–690.
- HAN, D., SUN, M., AND BATZEL, M. 2010. CO_2 velocity measurement and models for temperatures up to 200°C and pressure up to 100mpa. *Geophysics 75*, E123–E129.
- HOUSE, N. J., FAULDER, D., OLSON, G. L., AND FANCHI, J. 2003. Simulation study of CO_2 sequestration in a north sea formation. *Society of Petroleum Engineers Annual Technical Conference and Exhibition, 81202-MS, March 2003, San Antonio, Texas.*

- HUDSON, J. 1981. Wave speeds and attenuation of elastic waves in material containing cracks. *Geophys.J.R.astr.Soc* 64, 133–150.
- JIN, S. 1999. Characterizing reservoir by using jointly P- and S-wave AVO analysis. *69th Annual International Meeting, SEG, Expanded Abstracts*, 687-690.
- JOHNSON, D. H. 1997. A tutorial on time-lapse seismic reservoir monitoring. *Offshore Technology Conference*, 8289-MS, May 1997, Houston, TX.
- KALLA, S., WHITE, C., GUNNING, J., AND GLINSKY, M. 2009. Downscaling multiple seismic inversion constraints to fine-scale flow models. *SPE Journal* 14, 4, 746–758.
- KEY, S. C. AND SMITH, B. A. 1998. Seismic reservoir monitoring: Application of leading edge technologies in reservoir management. *Offshore Technology Conference*, 8648-MS, May 1998, Houston, TX.
- KUMAR, A., OZAH, R., NOH, M., POPE, G., BRYANT, SEPEHRNOORI, K., AND LAKE, L. 2005. Reservoir simulation of CO_2 storage in deep saline aquifers. *Society of Petroleum Engineers*, 89343, April 2004, Tulsa, Oklahoma.
- KUMAR, N. AND BRYANT, S. L. 2008. Optimizing injection intervals in vertical and horizontal wells for CO_2 sequestration. *Society of Petroleum Engineers* 116661.
- LAW, D. H., VAN DER MEER, L. B., AND GUNTER, W. B. 2003. Comparison of numerical simulators for greenhouse gas sequestration in coalbeds, part iii: more complex problems. *Second Annual Conference on Carbon Sequestration: Developing and Validating the Technology Base to Reduce Carbon Intensity*, 1–13.

- LINER, C. 2012. *Elements of Seismic Dispersion: A somewhat practical guide to frequency-dependent phenomena*. Society of Exploration Geophysicists, Distinguished Instructor Short Course, 2012.
- LINER, C., GENG, P., ZENG, J., AND KING, H. 2009. Toward flow simulation for CO_2 sequestration at the Dickman Oilfield, Ness Co., Kansas. *SEG Expanded Abstracts 28*, 3359–3363.
- LINER, C., GENG, P., ZENG, J., KING, H., AND LI, J. 2011. A CO_2 sequestration simulation case study at the Dickman Field, Ness Co., Kansas. *SPE Annual Technical Conference and Exhibition, 145791, 2011, Denver, Colorado*.
- MA, J. AND MOROZOV, I. 2010. AVO modeling of pressure-saturation effects in weyburn CO_2 sequestration. *The Leading Edge 29*, 178–183.
- MATHIESON, A., J., M., DODDS, K., WRIGHT, I., RINGROSE, P., AND SAOUL, N. 2010. CO_2 sequestration monitoring and verification technologies applied at Krechba, Algeria. *The Leading Edge 29*, 216–222.
- MAVKO, G., MUKERJI, T., AND DVORKIN, J. 2009. *The Rock Physics Handbook: Tools for Seismic Analysis of Porous Media*. Cambridge University Press.
- MENEZES, C. AND GOSSELIN, O. 2006. From log scale to reservoir scale: upscaling of the petroelastic model. *SPE Annual Technical Conference and Exhibition, 100233-MS, June 2006, Vienna, Austria*.
- METZ, B., DAVIDSON, O., DE CONINCK, H., LOOS, M., AND MEYER, L. 2005. IPCC (Intergovernmental Panel on Climate Change) Special Report on Carbon Dioxide Capture and Storage.

References

- NGHIEM, L., SAMMON, P., AND J., G. 2004. Modeling CO_2 storage in aquifers with a fully-coupled geochemical EOS compositional simulator. *Society of Petroleum Engineers*, 89474, April 2004, Tulsa, Oklahoma.
- NOH, M., LAKE, L., BRYANT, S., AND ARAQUE-MARTINEZ, A. 2004. Implications of coupling fractional flow and geochemistry for CO_2 injection in aquifers. *Society of Petroleum Engineers*, 89474, April 2004, Tulsa, Oklahoma.
- PAGANO, T., FANCHI, J. R., AND DAVIS, T. 2000. Integrated flow modeling: The fusion of geophysics and reservoir engineering. *SPE Annual Technical Conference and Exhibition*, 63137-MS, October 2000, Dallas, Texas.
- PHAN, S. AND SEN, M. 2010. Porosity estimation from seismic data at the Dickman Field, Kansas for carbon sequestration. *SEG Expanded Abstracts 29*, 2299–2303.
- RAZA, Y. 2009. Uncertainty analysis of capacity estimates and leakage potential for geologic storage of carbon dioxide in saline aquifers. *Master of Science Thesis, Massachusetts Institute of Technology*.
- REIMER, P. 1994. The utilization of carbon dioxide from fossil fuel fired power stations. *International Energy Agency Greenhouse Gas Research and Development Program*.
- RIBEIRO, C., REISER, C., AND DOYEN, P. 2007. Time-lapse simulator-to-seismic study - forties field, north sea. *SEG Expanded Abstracts 26*, 2944–2948.
- SAMSON, P., CASAUX, J.-M., CAVAILLES, B., LARRIBAU, E., MORANDINI, F., BIONDI, P., CALASSOU, S., AND JANODET, D. 1998. 3D modeling from seismic to fluid flow simulation: A case study. *SPE Annual Technical Conference and Exhibition*, September 1998, New Orleans, Louisiana.

References

- SKORSTAD, A. AND KOLBJORNSEN, O. 2005. Information content in forward 4d-seismic modeling and elastic inversion. *International Petroleum Technology Conference, 10660-MS, November 2005, Doha, Qatar.*
- SMITH, T., SONDERGELD, C., AND RAI, C. 2003. Gassmann fluid substitutions: A tutorial. *Geophysics 68*, 430–440.
- STOFFA, P. L., SEN, M. K., SEIFOUALLAEV, R., KLIE, H., GAI, X., BANGERTH, W., RUNGAMORNROT, J., AND WHEELER, M. F. 2005. An analysis of flow-simulation scales and seismic response. *SEG Expanded Abstracts 24*, 1461–1464.
- VEGA, S., PRAJAPAT, J., AND AI MAZROOEI, A. 2010. Preliminary experiments to evaluate the Gassmann equation in carbonate rocks: calcite and dolomite. *The Leading Edge 29*, 906–911.
- VEIRE, H. AND LANDRO, M. 2011. Simultaneous inversion of PP and PS seismic data. *Geophysics, 71*, 1–10.
- WU, Q. AND LINER, C. 2011. Case study: Comparison on shear wave velocity estimation in the Dickman field, Ness county, Kansas. *SEG Expanded Abstracts 30*, 4066–4070.
- YAMAMOTO, H., FANCHI, J. R., AND DAVIS, T. 2004. Integration of time-lapse seismic data into a flow model study of CO_2 injection into the weyburn field. *SPE Annual Technical Conference and Exhibition, 90532-MS, September 2004, Houston, Texas.*
- YUH, S., YOON, S., GIBSON JR., R., AND DATTA-GUPTA, A. 2000. 4D seismic feasibility study based on an integrated reservoir model. *Offshore Technology Conference, 12135-MS, May 2000, Houston, TX.*

References

ZELLER, D. E. 1968. The Stratigraphic Succession in Kansas. *Kansas Geological Survey Bulletin, University of Kansas Publications.*

APPENDICES

A. DETAILED GASSMANN FLUID SUBSTITUTION WORK FLOW FOR THE DICKMAN FIELD

This appendix provides a conventional work flow for calculating \mathbf{K}_{sat} with other reservoir properties.

1 *Kmin and density*

The Mississippian is composed predominately of dolomite and calcite. So the frame mineral bulk modulus can be estimated by Voigt-Reuss-Hill (VRH) averaging of constitutes:

$$K_{min} = \frac{1}{2}([V_{dolo}K_{dolo} + V_{cal}K_{cal}] + [\frac{V_{dolo}}{K_{dolo}} + \frac{V_{cal}}{K_{cal}}]^{-1}) \quad (\text{A.1})$$

The volume fraction of dolomite ($V_{dolo}=0.7$) and calcite ($V_{cal}=0.3$) in the frame were determined by geological analysis. The frame density is given by:

$$\rho_{min} = \rho_{dolo} \times V_{dolo} + \rho_{cal} \times V_{cal} \quad (\text{A.2})$$

For the other seal layers above this Mississippian-Pennsylvania unconformity in the flow simulation model, the seal layers are shale, and some layers are combination of limestone and shale. The mineral bulk modulus is also calculated as above. All mineral properties needed are given by the Rock Physics Handbook (Mavko *et al.*, 2009).

2 K_{fluid}

The fluid mixture is brine and CO_2 . Batzel and Wang (1992) provide formulae for calculation of brine bulk modulus as a function of temperature and pressure. The CO_2 bulk modulus uses the velocity formulas from (Han *et al.*, 2010), and the CMG output gives densities of the CO_2 in gas phase and liquid phase.

3 K_{dry}

The dry rock bulk modulus (K_{dry}) is calculated from the initial estimate of K_{sat} . The initial saturated rock bulk modulus can be estimated by the P and S wave sonic and density logs:

$$K_{sat} = \rho(Vp^2 - \frac{4}{3}Vs^2). \quad (A.3)$$

Since no shear sonic log is available, a Vp - Vs relationship is built from lithology derived from the well logs and core information at different depth intervals (Wu and Liner, 2011). The Humphery 4-18 sonic log is used to estimate the shear sonic log values, and combined with the density log to obtain K_{sat} . The dry frame bulk modulus can then be obtained using (Gassmann, 1951):

$$K_{dry} = \frac{K_{sat}(\frac{\phi K_{min}}{K_{fluid}} + 1 - \phi) - K_{min}}{\frac{\phi K_{min}}{K_{fluid}} + \frac{K_{sat}}{K_{min}} - 1 - \phi} \quad (A.4)$$

Once K_{dry} is calculated, it is fixed and assumed to represent the layered lithology throughout the field. We found an estimate of K_{dry} ranges from 15 GPa to 58.4 GPa for the Dickman site.

4 K_{sat}

With K_{min} , K_{dry} , and K_{fluid} known, we can write

$$K_{sat} = K_{dry} + \frac{(1 - \frac{K_{dry}}{K_{min}})^2}{\frac{\phi}{K_{fluid}} + \frac{1-\phi}{K_{min}} - \frac{K_{dry}}{K_{min}^2}} \quad (\text{A.5})$$

In the Gassmann theory it is assumed that fluid changes have no effect on shear modulus

$$\mu_{sat} = \mu_{dry} \quad (\text{A.6})$$

Then P wave velocity for the saturated rock can be estimated from the following:

$$V_{sat} = \sqrt{\frac{K_{sat} + \frac{4}{3}\mu_{sat}}{\rho_{sat}}} \quad (\text{A.7})$$

B. PREPROCESS THE FLOW SIMULATION OUTPUT

1 *Skipping headers*

The headers in the *.txt* files need to be eliminated. Here is the C program to skip the headers and store the data into a new file.

```
#include<stdio.h>
main(){
FILE *fp1,*fp2,*fp3,*fp
int c;
int i=0,j=0,number;
float x[32039];
float y[32039],value[32039];
float z[32039]; /*to store the z index*/
int dx=500;
int dz=150;
int dy=500;
int ix,iy,iz=1;
char str[100];
fp1=fopen("out1","wb+");
/*load several input data first, including porosity,depth*/
fp2=fopen("gassat22500101.txt","rt");
/*fp2=fopen("porosity.txt","rt");*/
fp3=fopen("depth.txt","rt");
fp4=fopen("gassat22500101","wb+");
```

```
if (fp2==NULL){
printf("wrong\n");
}
else{
while((fgets(str,100,fp2))!=NULL){
if(str[0]!='*&& str[0]!='<&& str[0]!='\n'){
sscanf(str,"%f %f %f\n",&x[i],&y[i],&value[i]);
i++;
}
}
}
printf("i=%d\n",i);
number=i;
i=0;
if (fp3==NULL){
printf("wrong\n");
}
else{
while((fgets(str,100,fp3))!=NULL){
if(str[0]!='*&& str[0]!='<&& str[0]!='\n'){
sscanf(str,"%f %f %f\n",&x[i],&y[i],&z[i]);
i++;}
}
}
printf("here\n");
```

```
for (j=0;j<number;j++){
ix=(x[j]-x[0])/dx+1;
iy=(y[0]-y[j])/dy+1;
fprintf(fp1,"%d %d %6.2f %15.8f\n",ix,iy,z[j],value[j]);
fprintf(fp4,"%9.2f %8.2f %6.2f %15.8f\n",x[j],y[j],z[j],value[j]);}
printf("data is=%d\n",number);
fclose(fp1);
fclose(fp2);
fclose(fp3);
fclose(fp4);
```

2 *Adding missing points*

This short script is used to adding the missing points detected from the inconsistent x and y index from the flow simulation output, and finding the correct location of this indices and adding the corresponding missing points back.

```
iz=1;
nx=33;
ny=31;
nz=32;
%datavol=zeros(nx,ny,nz);
count=zeros(32,1);
counttime=1;

for i=1:length
```

```

if a(i,1)==33 && a(i,2)==31
    if counttime==1
        count(counttime)=i;
        z(1:i)=iz; %read the first time, then assign iz=1 to the z index
    else
        count(counttime)=i-sum(count(1:counttime-1) );
        %record length of each slice
        z(count(counttime-1):count(counttime))=iz;
        %assign all the z index same for that slice
    end
    iz=iz+1;
    counttime=counttime+1;
end
end
%datavol(x(i),y(i),z(i))=value(i);

z(1:count(1))=1;
iz=2;
z(count(1)+1:sum(count(1:1+1)))=2;
% z(sum(count(1:2))+1:sum(count(1:2+1)))=3;
% z(count(3)+1:sum(count(1:3+1)))=4;

for i=2:31
    z(sum(count(1:i))+1:sum(count(1:i+1)))=i+1;
end

```

C. FLUX CORRECTION TO THE TRANSPORT EQUATION FOR ELASTIC FORWARD MODELING FINITE DIFFERENCE METHOD

1 *Implementation of elastic finite difference forward modeling*

Here is the script for performing the **Sufctanismod** which includes several parameters for the input.

```
# SIMULATION TIME
nt=10000
dt=0.0002
time=2
indexdt=0
## THE MODEL:
nx=2400
nz=757
dx=2.0
dz=2.0
## THE SOURCE: depth in gridpoints iz,  $z=(iz-1)*dz$ 
sx=2400
sz=1
## THE RECEIVERS: depth in gridpoints iz,  $z=(iz-1)*dz$ 
receiverdepth=2
# source=1 means that it is a point source
```

```
source=1
# Source information (index=direction of source)
indexux=0
indexuy=0
indexuz=1
# source wavelet
wavelet=2
fpeak=45
# impulse is 1 is a single source
impulse=1
## OUTPUT (using suheaders on seismograms):
suhead=1
reflxfile=shotx.su
reflzfile=shotz.su
afile=
cfile=
ffile=
lfile=
nfile=
vspxfile=vspx.su
vspzfile=vspz.su
## THE NUMERICAL METHOD:
# Order of numerical method
order=4
eta=0.015
```

```
eta0=0.012
# Coordinates to start/stop using FCT (in gridpoints)
fctxbeg=0
fctxend=100
fctzbegin=0
fctzend=100
# isurf=1 means that we have an absorbing boundary at the top as well
isurf=1
# using FCT
dofct=1
# Using moving boundaries
movebc=1
mbx1=10
mbx2=900
mbz1=10
mbz2=90
# The files are:
# cfile - c33
# lfile - c44
# afile - c11
# nfile - c66
# ffile - c13
fd:
    sufctanismod \
        nt=$(nt) \
```

```
receiverdepth=$(receiverdepth) \  
indexdt=$(indexdt) \  
time=$(time) \  
dt=$(dt) \  
movebc=$(movebc) \  
fpeak=$(fpeak) \  
nx=$(nx) \  
nz=$(nz) \  
dx=$(dx) \  
dz=$(dz) \  
suhead=$(suhead) \  
mbx1=$(mbx1) \  
mbx2=$(mbx2) \  
mbz1=$(mbz1) \  
mbz2=$(mbz2) \  
sx=$(sx) \  
sz=$(sz) \  
indexv=$(indexv) \  
source=$(source) \  
fctxbeg=$(fctxbeg) \  
fctxend=$(fctxend) \  
fctzbeg=$(fctzbeg) \  
fctzend=$(fctzend) \  
dfile=rho.dir \  
cfile=c33.dir \  

```

```
    afile=c11.dir \  
    ffile=c13.dir \  
    lfile=c44.dir \  
    nfile=dummy_zero.dir \  
    indexux=$(indexux) \  
    indexuy=$(indexuy) \  
    indexuz=$(indexuz) \  
    wavelet=$(wavelet) \  
impulse=$(impulse) \  
    isurf=$(isurf) \  
    dofct=$(dofct) \  
    order=$(order) \  
    eta=$(eta) \  
    eta0=$(eta0) \  
    reflxfile=$(reflxfile) \  
    refllyfile=$(reflyfile) \  
    reflzfile=$(reflzfile) \  
> junk
```

2 *Implementation for generating the stiffness and shear model*

```
#!/bin/sh  
set -x  
ninf=1  
nx=200
```

```
nz=100
dx=5
dz=5
fx=0.0
fz=0.0
dvdv=0.0
npmax=100
dvdz=0.0,0.0
v00=1500.,2500.
unif2 < boundaries > vp.dir nx=$nx nz=$nz ninf=$ninf dx=$dx dz=$dz\
    dvdv=$dvdv v00=$v00 dvdz=$dvdz npmax=$npmax
v00=800.,1600.

unif2 < boundaries > vs.dir nx=$nx nz=$nz ninf=$ninf dx=$dx dz=$dz\
    dvdv=$dvdv v00=$v00 dvdz=$dvdz npmax=$npmax
v00=1000.,2100.

unif2 < boundaries > rho.dir nx=$nx nz=$nz ninf=$ninf dx=$dx dz=$dz\
    dvdv=$dvdv v00=$v00 dvdz=$dvdz npmax=$npmax
v00=0.,0.

unif2 < boundaries > delta.dir nx=$nx nz=$nz ninf=$ninf dx=$dx dz=$dz\
    dvdv=$dvdv v00=$v00 npmax=$npmax
v00=0.,0.

unif2 < boundaries > epsilon.dir nx=$nx nz=$nz ninf=$ninf dx=$dx dz=$dz\
    dvdv=$dvdv v00=$v00 npmax=$npmax
```

```
cp epsilon.dir dummy_zero.dir
```

```
# Transform into stiffness coefficients
```

```
vpfile=vp.dir
```

```
vsfile=vs.dir
```

```
rhofile=rho.dir
```

```
epsfile=epsilon.dir
```

```
deltafile=delta.dir
```

```
gammafile=gamma_lens
```

```
c11_file=c11.dir
```

```
c13_file=c13.dir
```

```
c33_file=c33.dir
```

```
c44_file=c44.dir
```

```
c66_file=c66.dir
```

```
vel2stiff vpfile=$vpfile vsfile=$vsfile rhofile=$rhofile epsfile=$epsfile \
```

```
deltafile=$deltafile nx=$nx nz=$nz \
```

```
c11_file=$c11_file c13_file=$c13_file c33_file=$c33_file \
```

```
c44_file=$c44_file c66_file=$c66_file
```

```
exit 0
```

